HYDRODYNAMIC AND THERMAL ANALYSES OF POOL BOILING DATA OBTAINED FROM EXPERIMENTS PERFORMED ON FLAT HORIZONTAL HEATERS WITH CONVENTIONAL AND NANO-STRUCTURED SURFACES

A Thesis

by

RONITA ROY

Submitted to the Office of Graduate and Professional Studies of
Texas A&M University
in partial fulfillment of the requirements for the degree of

MASTER OF SCIENCE

Chair of Committee,	Debjyoti Banerjee
Committee Members,	Jonathan Felts
	Karen Kirkland
Head of Department,	Andreas A. Polycarpou

December 2017

Major Subject: Mechanical Engineering

ABSTRACT

Pool boiling phenomena on different types of heater configurations have been explored in the heat transfer literature. Pool boiling experiments on heaters with nanostructured surfaces have gained popularity in contemporary literature for microchip cooling application. The thermal management challenges for cooling of electronic chips have become more acute with decrease in the size for these microchips with concomitant increase in device density and heat flux. Pool boiling is expected to provide appropriate technology solutions to meet these challenges for high heat flux cooling at low temperature differentials.

In this study, results obtained from pool boiling experiments were analyzed. The experiments were performed using heaters with plain surfaces (copper and silicon) and nanostructured surfaces (Anodic Aluminum Oxide/AAO). In these experiments, high speed digital image acquisition apparatus was used to record bubble dynamics (nucleation, growth and departure) for both nucleate and film boiling regimes. The videos were used to obtain the bubble diameter at departure, bubble growth rates (bubble height as a function of time) and bubble departure frequency. The objective of these experiments was to explore the change in bubble dynamics for different heater configurations in order to ascertain their role in the observed changes in the values of pool boiling heat flux as a function of wall superheat (i.e., from the boiling curves obtained in these experiments). These experiments were performed for saturated boiling conditions as well as for liquid subcooling of 5 °C and 10 °C. The test fluid was PF-5060 (Manufacturer: 3M Corp.). The

experimental apparatus utilized in this study consisted of a visualization chamber, cartridge heaters, power supply, high speed digital data acquisition system and chiller unit. Temperature nanosensors (Thin Film Thermocouples/ TFT) as well as wire bead thermocouples were used for measurement of wall superheat. Micro/ nano-fabrication techniques were utilized in this study for realizing the test surfaces integrated with temperature nanosensors.

The data gleaned from these experiments were compiled to obtain a correlation for the optimal heat transfer for different heater surface configurations. Literature review was also performed in this study to compare the experimental results with correlations for bubble dynamics available in the literature. The experimental results for bubble dynamics show that while silicon and copper surfaces have similar values for bubble departure diameter, the variability in the bubble departure frequency values for copper heater experiments were larger than that of silicon heaters. This trend is potentially due to large variation in surface roughness on copper heaters compared to that of silicon wafers (which are single crystal silicon substrates and therefore are atomically smooth at the commencement of the experiments). Heaters with nanostructured surfaces (e.g., for AAO heaters) were observed to yield smaller bubble departure diameters and higher bubble departure frequencies.

DEDICATION

This work is dedicated to my mother, father, sister and boyfriend, who guided me and gave me the strength needed to finish this program.

ACKNOWLEDGEMENTS

I would like to thank my committee chair, Dr. Debjyoti Banerjee, and my committee members, Dr. Karen Kirkland and Dr. Jonathan Felts, for their guidance and support throughout the course of this research.

Acknowledgements are also extended to Dr. Hongjoo Yang, Mr. Binjian Ma, and Mr. Yi Wang who helped perform the experiments and assemble the experimental apparatus as well the micro/nano-fabrication and materials characterization. I would also like to acknowledge Ms. Shambhobi Bhattacharya from IIT Kharagpur, Ms. Cynthia Gamboa from University of Texas in El Paso, and Mr. Alfonso Vallejo from University of Texas Brownsville for their contributions into the data collection and analysis. Mr. Navin Kumar also receives my thanks for providing some of the figures for this paper.

Thanks also go to my friends, colleagues in the research group of Dr. Banerjee, departmental faculty and staff for making my time at Texas A&M University a great experience. Finally, thanks to my mother, father, and sister for their encouragement and to my boyfriend for his patience and love.

NOMENCLATURE

AAO	Anodic Aluminum Oxide
A	surface area (m^2)
Bo	Bond number
c_p	specific heat (J/kg-K)
CF	calibration factor (pixels/mm)
C_g	geometric factor
CHF	Critical Heat Flux
d_D	departure diameter of bubble (mm)
D_c	critical cavity diameter (m)
D_{cl}	contact line length (m)
f	departure frequency of bubble (1/s)
F_b	buoyancy force (N)
F_s	surface tension force (N)
F_g	force of gravity (N)
g	gravitational acceleration (m/s^2)
h_{fg}	latent heat of vaporization (J/kg)
Ja	Jacob number
Ja*	modified Jacob number
k	thermal conductivity (W/m-K)
N	nucleation site density ($1/m^2$)

Pr	Prandtl number
q''	heat flux (W/cm^2)
r	radius of cavity (m)
t	elapsed video time (ms)
T_{sat}	saturation temperature (°C)
T_w	wall temperature (°C)
$\dot{V}$	volumetric flow rate of vapor (m^3/s)
y	y-coordinate measurement (pixels)

Greek symbols

α	thermal diffusivity (m^2/s)
θ	contact angle (degrees)
μ	dynamic viscosity (Pa-s)
ρ	density (kg/m^3)
σ	surface tension (N/m)
ω	uncertainty

Subscripts

l	liquid
v	vapor

CONTRIBUTIONS AND FUNDING SOURCES

Contributors

This work was supported by a thesis committee consisting of Dr. Debjyoti Banerjee (advisor) and Dr. Jonathan Felts of the Department of Mechanical Engineering and Dr. Karen Kirkland of the Department of Nuclear Engineering.

The author acknowledges the help of Dr. Hongjoo Yang, Mr. Binjian Ma, and Mr. Yi Wang for performing the pool boiling experiments and obtaining the raw data which were then analyzed and reported in this study. Ms. Shambhobi Bhattacharya, Ms. Cynthia Gamboa, and Mr. Alfonso Vallejo are acknowledged for data collection and processing. Mr. Navin Kumar is also acknowledged for assisting in technical laboratory procedures.

All other work conducted for the thesis was completed by the student independently.

Funding Sources

Graduate study was supported by a fellowship from Texas A&M University and a thesis research fellowship from the National Science Foundation.

TABLE OF CONTENTS

Page

LIST OF FIGURES

Page

LIST OF TABLES

Page

1 INTRODUCTION

1.1 Background

Improved methods are needed to prevent overheating of microchips in electronic devices. Non-uniform temperature distribution ("hot-spots") and overheating of microchips are serious issues as they cause severe decline in performance of these devices with increase in operating temperatures. As the size for these microchips decrease with concomitant increase in operating frequencies (as well as operating power ratings), the heat flux increases (and therefore, the cooling loads for the dissipated heat - by the thermal management platforms increases). Fin-fan cooling was the standard protocol for heat dissipation in early generation of microchips and packages. Traditionally, fin-fan cooling leveraged the use of fins in heat sinks and fans to improve the cooling efficacy of packages used for electronic components with the goal of preventing these systems from overheating. However at high heat fluxes, large form-factors for fans and heat sinks would be required, rendering this approach uneconomical and impractical for use. Hence, pool boiling is regarded as an alternative option for microchip cooling as it affords large heat flux values to be achieved for small enough temperature differences between a hot surface and working fluid.

One of the benefits accrued from employing boiling is the high heat flux values obtained at small temperature difference between a hot surface and the working fluid (this is typically the same range of temperatures used for single phase convection heat transfer in fin-fan cooling applications). A multitude of transport mechanisms are non-linearly coupled during pool boiling, such as: mass transfer, latent heat transfer (phase change),

forced or natural convection heat transfer, periodic transient conduction through solid-liquid contact effects, and microlayer effects (nano-scale transport phenomena at liquid-vapor and solid-liquid interfaces). The fluid movement at the heater surface is induced by the periodic inception, growth and departure of vapor bubbles (due to buoyancy forces) that in turn leads to a combination of forced and free convection of the liquid phase. Pool boiling can be classified into specific regimes: nucleate, transition and film boiling. Depending on the bulk temperature of the liquid phase - boiling can also be classified as subcooled and saturated. Subcooled boiling occurs when the bulk temperature of the liquid phase is below the saturation temperature (boiling point). In saturated boiling the bulk temperature of the liquid phase is at the saturation temperature (boiling point). The difference between the heater temperature (T_w) and the saturation temperature of the boiling liquid (T_{sat}) is called the "Excess Temperature" or "Wall Superheat" (ΔT_e). The plot of wall heat flux as a function of wall superheat is called the boiling curve. Nukiyama proposed the use of boiling curve to describe the various regimes in boiling [1]. Figure 1-1 shows a typical boiling curve on a "large" horizontal metallic heater surface with various regimes of saturated pool boiling for typical working fluids (e.g., water).

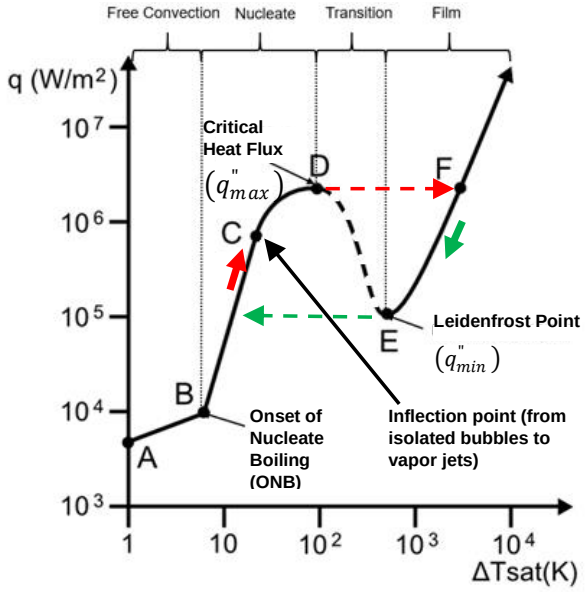

Figure 1-1 Typical pool boiling regimes for water at 1 atmosphere

1.2 Boiling Curve

When the heater surface is at the boiling point (ΔT_e = 0 °C) free convection governs the fluid motion in this region and the bubbles are not visible at this time. Onset of Nucleate Boiling (ONB) is typically observed at non-zero wall superheat (for water, typically, ΔT_e > 3~5 °C). ONB is characterized by the inception of isolated bubbles on the heater surface. Bubbles typically nucleate in surface imperfections on the heater – such as cavities, grooves and scratches that are typically several microns in size. At this condition a good proportion of the nucleated bubbles are in dynamic equilibrium resulting in very small growth rates and often the bubbles do not depart from the boiling surface. The total heat flux on the heater surface is equitably distributed between free convection heat transfer and phase change heat transfer.

As the wall superheat is increased beyond the ONB condition, the nucleation site density of the bubbles on the heater surface increases along with enhancement in the growth rates and departure frequency of bubbles from the heater surface. This induces additional convection in the bulk of the liquid phase away from the surface of the heater by the departing bubbles that have risen in the liquid pool due to buoyancy induced convection. This is termed as Partial Nucleate Boiling (PNB) where only a few of the larger-sized cavities on the heater surface have nucleating bubbles. Increasing the wall superheat results in further increase in nucleation site density since progressively smaller cavities on the heater surface nucleate. Fully Developed Nucleate Boiling (FDNB) regime is established when the wall superheat reaches a critical value resulting in all of the cavities available on the boiling surface to activate and start nucleating bubbles. Any further increase in wall superheat leads to vertical coalescence of the vapor bubbles – since the rate of vapor bubble production from the heater surface marginally exceeds the rate at which bubbles depart from the heater surface (bubble departure frequency) due to hydrodynamic forces (e.g., buoyancy and inertia forces). Coalescence of the vapor bubbles in the vertical direction leads to the formation of "vapor jets" and "mushroom shaped vapor columns".

As the number density of vapor jets (per unit area) on the heater surface increases with increase in wall superheat – it reaches the limit of vapor production from the heater surface – leading to an unstable regime, which is termed as the "Critical Heat Flux (CHF)" point. This is also called the "Maximum Heat Flux" condition - since this is typically the maximum possible heat flux that can be obtained from the heater surface under pool

boiling conditions. At CHF the heater surface is typically modeled to be covered with vapor jets that are spaced in an array with the pitch of the jets being proportional to the Taylor instability wavelengths. For typical fluids (e.g., water and refrigerants) CHF conditions is reached for wall superheat values less than 20 °C. In FDNB and CHF the free convection heat transfer is a minute fraction (less than 2 ~ 3%) of the total heat flux. Any further increase in wall superheat beyond CHF conditions causes a decrease in heat flux due to complex hydrodynamic interactions between the liquid and vapor phases, and this unstable pool boiling regime is called "Transition Boiling (TB)". The heat flux values obtained in TB are difficult to replicate since the fluctuations in the rate of change of heater surface temperature leads to different values of heat flux and steady state conditions are not easily achieved in this mode of boiling. In TB – the vapor removal process due to hydrodynamic/ buoyancy forces in the axial direction are inadequate to remove excess mass in the vapor jets causing a few of the vapor jets to merge laterally in the transverse direction. This lateral merger leads to the formation of vapor films that act as an insulating blanket on the heater surface. Hence the heat flux from a part of the heater is reduced leading to formation of local "hot spots" on the heater surface which leads to further growth of the film boiling region on the heater surface. Under these conditions – reducing the wall superheat leads to higher heat fluxes while increasing the wall superheat causes reduction in the total heat flux from the heater surface.

Eventually, at high wall superheat values (e.g., 100 ~ 200 °C for water at a system pressure of 1 atmosphere) the entire heater surface is covered with a uniform vapor film and this regime is termed as "Film Boiling (FB)". Vapor bubbles are formed periodically

due to fluid instability (e.g., Taylor instability). Bubbles that form from this vapor film grow and depart at much reduced frequency but have larger departure diameters with a lower number density on the heater surface. This occurrence results in substantially smaller heat flux values compared to CHF. Free convection heat transfer from the vapor film surface into the liquid pool is a significant fraction of the total heat transfer. In addition, radiation heat transfer at these high temperatures can significantly enhance the net heat flux values. Decrease in wall superheat in film boiling causes proportional decrease in heat flux values (in contrast, during transition boiling - decrease in wall superheat can lead to increase in wall heat flux). However, at a critical value of the wall superheat the stable vapor film collapses causing a part of the heater surface to operate in partial nucleate boiling regime while remaining part of the heater surface is covered with a blanket of vapor film. As a result, the systems reverts to Transition Boiling ("TB") regime once again. This critical value of wall superheat is known as the "Leidenfrost Point" ("LP") and the associated value of heat flux is called the "Minimum Heat Flux (MHF)" in pool boiling. Any further decrease in wall superheat causes progressive increase in proportion of the heater surface to be in the nucleate boiling regime until the entire heater surface operates in the nucleate boiling regime. The progression of the boiling curve from FDNB to CHF to TB to FB to LP and further to PNB is termed as the "boiling hysteresis" since different values of heat fluxes are reached when the wall superheat is increased beyond CHF or decreased below stable FB.

Often in engineering applications the high heater temperatures that result in transition boiling (or film boiling) when CHF condition is exceeded causes heaters to melt

leading to catastrophic failures (such as the accident and melt-down of the nuclear power plant in Chernobyl) and is therefore termed as “burnout”. Hence, CHF is an important parameter that determines the safe operating conditions for the heater material. The imposed values of heat flux or wall superheat beyond that of the CHF condition could run the risk of melting the heater surface. Hence, in design of thermal systems, CHF is an important parameter that needs to be determined and accounted for during operation (or monitored so that CHF conditions are not exceeded). Similarly, the study of film boiling is important for developing safety protocols in the design of thermal systems, such as for scenarios involving melt-down of nuclear reactors, i.e., Loss of Coolant Accident (LOCA). Hence, the determination of the Leidenfrost Point (LP) is important in this regard. Transition Boiling has not received much attention in the literature since this is an unstable regime and therefore has not been exploited in design of thermal systems or other engineering applications.

The boiling regimes are governed by different transport mechanisms (i.e., non-linear coupling of various modes of mass transfer and heat transfer). To model and predict the thermo-fluidic interactions in each boiling regime it is essential to have a coherent cognition of the various types of interactions between each of these different transport mechanisms. Insights about the coupled non-linear interactions between the hydrodynamic and thermal transport mechanisms can enable the identification of the dominant transport mechanisms as well as the most sensitive parameters that control wall heat flux in various modes of pool boiling. Considering that latent heat transfer is the more dominant mode or the primary contributor to the total heat flux (in comparison to free

convection heat transfer) for major part of the boiling curve, the volumetric flow rate was estimated by Jensen and Memmel [2] as:

$$q" = \frac{\rho_v \dot{V} h_{fg}}{A} \tag{1}$$

In this equation, h_{fg} is the latent heat of vaporization, A is the area of the heater surface, and ρ_v is the density of the vapor bubble and $\dot{V}$ is the net volumetric flow rate of vapor from the heater surface. The numerator equals the total heat transfer (q) accruing from phase change. The heat flux (q''), is evaluated by dividing the total value of heat transfer (q) by the total "projected" heater surface area (A).

Volumetric flow rate of vapor emanating from the heater surface needs to be analyzed in order to predict the value of wall heat flux. The volumetric flow rate of vapor ($\dot{V}$) can be estimated by assuming that each bubble has a perfect spherical shape, as stated by Kutateladze and Gogonin's research on growth rate and diameter of a bubble in free convection boiling [3]:

$$\dot{V} = \left(\frac{\pi}{6} d_D^3\right) f(AN) \tag{2}$$

where, N is defined as the active number of nucleation sites per unit area, d_D is the bubble departure diameter, and f is the bubble departure frequency. Hence the volumetric flow rate (as well as pool boiling heat flux) is most sensitive to the bubble departure diameter and moderately sensitive to the nucleation site density and the bubble departure frequency. It may be noted that bubble departure frequency depends on the bubble departure diameter. For example, larger bubbles typically require more time (during the inception-to-growth-

to-departure cycle) and therefore have smaller values of bubble departure frequency. This implies that there is an optimum value of nucleation cavity size on the heater surface for which the vapor volumetric flow rate is maximized by amplifying the net product of the bubble departure volume and the bubble departure frequency.

If convective heat transfer were to be the dominant factor instead, bubble departure diameter and bubble frequency would still be important parameters for quantifying the rate of fluid convection. Nucleation site density depends on the manufacturing process used for fabricating the heater and is beyond the scope of this study. Therefore, the scope of this study is focused on the measurement of bubble departure diameter and bubble departure frequency.

The significant factors that affect the bubble dynamics on the heater surface are expected to be: the surface properties (e.g., roughness and contact angle or surface energy), wall superheat, and the thermo-physical properties of the fluid (such as surface tension, density, thermal diffusivity, viscosity, specific heat capacity and thermal conductivity). For high temperatures (such as in film boiling) the radiative properties of the fluid and heater surfaces also play a significant role. Insight into the mechanisms affecting pool boiling phenomena requires the analyses of forces acting on an individual vapor bubble located on a heater surface. Comparing the magnitude of the different forces (e.g., surface forces and body forces) – the force due to surface tension (σ) and the buoyancy force - are the most significant forces that affect the growth and departure of a bubble. In contrast, the inertial forces (due to acceleration or deceleration) as well as drag forces are estimated to be much smaller in magnitude (approximately 10 ~ 100 times smaller in magnitude).

Hence, these latter forces are often neglected. Equating the surface tension and buoyancy forces on a departing bubble enables the estimation of the length-scale (l_o) in boiling and is expressed as [4]:

$$l_o = \sqrt{\frac{\sigma}{[(\rho_l - \rho_v)g]}} \tag{3}$$

where ρ_l is the liquid density, and g is the acceleration due to gravity in the direction of bubble departure. It can be expected that the bubble departure diameter (d_D) is a linear function of l_o and can be expressed as:

$$d_D = C \cdot l_o \tag{4}$$

where C is a constant that depends on the thermo-physical properties of the fluid and the experimental conditions (e.g., wall superheat, liquid sub-cooling, etc.). Similarly, the bubble departure frequency (f) can be estimated from linear stability analysis (e.g., using Taylor instability analysis), by defining an equivalent growth rate (ω). This can be expressed as [4]:

$$\omega = 2\pi f = \sqrt{\frac{(\rho_l - \rho_g)g}{(\rho_l + \rho_g)l_o}} = \frac{(\rho_l - \rho_g)^{\frac{1}{4}} g^{\frac{3}{4}}}{(\rho_l + \rho_g)^{\frac{1}{2}} \sigma^{\frac{1}{4}}} \tag{5}$$

These equations show that larger bubble departure diameters are expected in reduced gravity (such as in space based thermal systems) and therefore the bubble departure frequency will be lower in this scenario. Also, fluids with smaller density differences between liquid and vapor phases (such as for refrigerants) are expected to yield

proportionally larger bubble departure diameters but lower values of bubble departure frequency. Similarly as the surface tension decreases for the working fluids – the bubble departure diameter is expected to decrease with a concomitant increase in the bubble departure frequency. It is expected that inception of nano-bubbles on nanostructured heater surfaces are possible due to the lower values of surface tension that can occur under such special conditions [5]. Surface tension values can be reduced significantly when liquid-vapor interfaces are subjected to high electric field gradients or high concentration gradients (both of which are expected to occur during inception of nano-bubbles on heaters with nano-structured surfaces). Extreme values of concentration gradients can occur even for small fluctuations in ionic concentration (or even for small fluctuations in concentration of impurities dissolved in the liquid) that occur over very small distances on the liquid-vapor interface of the nano-bubble (which, during the inception process, is of the same order of magnitude as the inter-molecular spacing). Hence, simple model formulations, such as those mentioned above, can provide significant insights and enable the prediction of bubble departure phenomena.

Typically, bubble nucleation is favored in dents, cavities, pits and grooves (surface imperfections or surface roughness) on a heater. This is possibly due to the trapped gasses (or from the dissolved gasses that are ejected from the working fluid into these surface imperfections when heated). The dents, cavities, and grooves on a surface thus serve as nucleation sites. The bigger grooves provide the optimum nucleation sites for bubble formation when the fluid is heated initially. As a bubble starts growing, the adhesive forces caused by surface tension tends to keep it attached to the surface. Hence, the contact angle

significantly influences the growth of vapor bubbles. As the bubble continues to grow, buoyancy steadily pushes it upward against the surface tension force, while the bubble continues to form its dome-like shape. A bubble departure cycle is comprised of two parts: waiting time (t_w) and growth time (t_g). The waiting time is defined as the time required to form a thermal boundary layer of a required thickness to enable bubble inception from a surface cavity. The growth time is the time taken by the bubble after inception to grow and reach the bubble departure diameter. Bubble departure diameter can be correlated to its growth time if the growth rate history of the bubble can be estimated (e.g., from linear stability analysis and thermal-hydrodynamic analysis). Smaller cavities produce smaller bubbles, which in turn have smaller wait times and larger growth times (and vice-versa for larger cavities). Inception of smaller bubbles accrue from smaller nucleation cavities, hence, the wait times are smaller since the transient conduction process governing the formation of the thermal boundary layer of the same height (i.e., equal to the cavity diameter) requires less time. Hence smaller bubbles require more growth time in order for the smaller bubbles to reach the departure diameter. As mentioned before, this implies that there exists a range of cavity sizes for which the optimum condition is reached to maximize the bubble departure frequency (i.e., to minimize the sum of waiting time and growth time). This also enables the vapor volumetric flow rate on the heater surface to be maximized.

The analysis of bubble frequency and departure diameter helps in establishing the numerical structure of the correlations that are derived from boiling experiments. These numerical approaches also enable the comparisons for different experimental conditions

and can be used for evaluating the efficacy of the various transport mechanisms during boiling. It is essential to understand the correlation between different experimental parameters because this can help quantify the various heat transfer mechanisms occurring on the heater surface. Experimental validation and calibration of these correlations also enable reliable estimates to be derived for different segments of the boiling curve – such as CHF, MHF and for film boiling heat flux values as a function of wall superheat as well as for nucleate boiling heat flux values as a function of nucleate site density (it is assumed implicitly that the wall superheat and liquid sub-cooling conditions are specified in these analyses). Thus, the bubble departure diameter and bubble departure frequency correlations are needed as a means to estimate the heat transfer from various heater surfaces and configurations.

The analyses of the trends of bubble departure diameter and the correlations provide the means to exploit heater surface configurations to enhance CHF, which can enable better thermal management schemes to be implemented (such as for electronic chip cooling). The correlations available in contemporary literature however suffer from the drawback of having a wide margin of variability. The data used to produce many of these correlations are also widely scattered, with large uncertainty values and often no discernible trends can be identified. Lack of repeatability of experiments often add to the enigma and reduce the reliability of these correlations. This necessitates careful implementation of experimental protocols for the purpose of generating reproducible data. Literature review suggests non-uniformity and scattered correlation trends. There are many correlations that provide specific trends for bubble dynamics for different heater

surfaces during pool boiling of various fluids in each boiling regime (e.g., PNB, FDNB, CHF, FB, LP, etc.).

The investigation of bubble dynamics has been explored extensively in the literature for conventional heater surfaces. However, only few reports exist in the literature for investigation of bubble dynamics on nano-structured heater surfaces (e.g., for bubble departure diameter or frequency correlations). The analyses of experimental data obtained from flow visualization experiments of bubble dynamics during pool boiling for various boiling regimes can provide additional insights about the coupling of thermal and hydrodynamic processes. This, in turn, can enhance our understanding of the coupled transport processes during pool boiling on conventional heater surfaces and heaters with nano-structured surfaces.

1.3 Literature Review

Boiling and condensation are ubiquitous in various thermal management applications. To name a few, applications include: climate control systems (e.g., HVAC), desalination, and electrical power generation ([6] [7] [8] [9]). Surface texturing has been demonstrated to enhance boiling and condensation heat transfer by modulating the surface energy and surface roughness [7]. Different fabrication techniques for texturing of heat exchanging surfaces have been explored in the literature, such as, the top-down method (lithography with surface etching) or the bottom-up method (chemical oxidation) [8]. Generally, lower values of CHF is undesirable as it can lead to instability during pool boiling. Therefore, various schemes to enhance CHF has been explored extensively in the

literature. Contemporary techniques employed for enhancing CHF include: oxidation to improve wettability, vibration of heaters for augmenting bubble departure, surface coatings for increasing effective heater surface area, heater rotation to promote bubble departure, fluid vibration for improved liquid circulation supply, and imposing electric fields for modulating wettability as well as increasing liquid renewal [10]. The scope of this literature review is focused on surface coatings.

Conventional machining involves the traditional method of polishing, grinding or sand blasting. Most of these methods generally function to increase surface roughness of the material so that additional nucleation sites are created [11]. Surface coating techniques involve more invasive processes, and include vapor deposition, atomic layer deposition, sputtering, exposure to nanofluids, and spin coating. Chemical fabrication processes include wet etching and oxidation. These methods typically yield surface coatings containing nanowires which are patterned through photochemical etching. Micro/nano-fabrication processes (e.g., typically used in MEMS/NEMS) can be adapted for fabricating nanostructured surfaces, which uses a combination of photolithography for etching and material deposition (e.g., by Physical Vapor Deposition/ PVD or Chemical Vapor Deposition/ CVD). This is adapted from techniques used in microfluidics, electronics fabrication/ semiconductor manufacturing (CMOS processes), microsensor fabrication, and nano/bio-fabrication [11].

A major proportion of the literature reports have focused on the behavioral studies that explored the variation in CHF for various types of surface textures. A small proportion of the reports in the literature have utilized these behavioral approaches to delve deeper,

i.e., by attempting to correlate these experimental results with the molecular interactions. This approach has enabled the identification of the underlying causes for the anomalous trends observed in the experimental measurements. For instance, Hu and Sun [12] discussed the effect of Kapitza resistance on heat flux values observed in boiling experiments performed using water on gold nanoparticle coated heater surfaces. In this study the values of Kapitza resistance was predicted to decrease with increased in the height of the nanoscale patterns on the heater surface. However, boiling in general was not observed to modulate the Kapitza resistance of the water-gold interface [12]. Heater size and height of the nanoscale patterns were described to be critical parameters in determining the level of boiling heat flux enhancement. Kwark et. al. [13] deduced that heater size, pressure and orientation were important for determining pool boiling performance. The authors also discussed that heat flux values were very sensitive to the variation in wettability (i.e., increased wettability would decrease resistance for bulk fluid movement).

Microfabrication techniques were used for enhancing the effective surface area as well as for integrating heater surfaces with temperature sensors. A few studies in the literature have utilized microsensors that were integrated with artificially sculpted micro-cavities on a heater surface to correlate their effect on the resulting bubble dynamics in pool boiling. Hutter et. al [14] reported that at atmospheric pressure the values of bubble nucleation density, departure diameter and frequency were not affected by the introduction of micro-cavities during nucleate pool boiling on a silicon surface (that was integrated with a micro-heater and temperature microsensors). However, increasing the pressure by

0.5 bar decreased the wall superheat significantly, with a concomitant increase in the bubble departure diameter. Hutter et. al. [15] in a separate study using these microsensors found good agreement with previous literature reports on bubble nucleation at lower values of wall superheat. However, bubble nucleation was found to be weakly sensitive to the cavity depth or system pressure. Hence, microfabrication techniques can be leveraged to enhance boiling heat flux as well as for experimental probing of the heater surface temperature.

Reports in the literature have explored various schemes for surface modifications with the aim of enhancing boiling heat flux for the same wall superheat (or achieve higher values of CHF, either higher or lower values of excess temperature). Some of the literature reports focused on enhancing the nucleate boiling heat transfer coefficient compared to plain surfaces ([9] [16] [17] [18]), while other reports focused on utilizing nanoparticle deposition on heater surfaces using nanofluids to realize enhancement of CHF [19], as well as achievement of boiling incipience at lower values of wall superheat ([16] [18] [20]). Increased wettability of nanostructured heater surfaces was reported to yield higher water adsorption and increased capillary wicking ([13] [21] [22] [23]). Hence, the underlying theme in these studies demonstrate that micro/nano-fabrication techniques can be utilized to realize nanostructured surfaces that can dramatically enhance pool boiling heat flux values. Increase in the surface roughness of the heater surface causes augmentation of the active nucleation sites during pool boiling ([18] [24] [25] [26]). It was also reported that the there is a concomitant increase in bubble departure frequency while the bubble departure diameter was decreased ([20] [24] [26] [27]). Higher values

of contact angle was associated with lower values of wall superheat at which boiling incipience was observed [22]. Similar observations were also recorded in condensation experiments where reduction in the wettability of the heat exchanging surfaces resulted in higher values of heat flux ([8] [21]).

The CHF enhancement on nanostructured surfaces have been explored in a few reports in the literature. Zou and Maroo [28] performed experiments using micro/nano-scale ridges fabricated on heater surfaces composed of Silicon and Silicon Dioxide, with enhancement of CHF reported to be as much as 125% (while the surface area was estimated to increase by only 40%, for these surface structures). This demonstrates that the enhancement is mediated by other factors than just the augmentation of the effective surface area of nanostructures surfaces. The critical height for maximizing heat flux was reported to be ~450 nm for Si and ~900 nm for SiO_2. Lu et. al. [9] reported a dramatic increase in CHF on surfaces with silicon nanowires compared to plain Si surfaces. In the absence of accurate metrology techniques for surface temperature measurements the study failed to compare the level of enhancement of CHF values on a percentage basis. The CHF values reported were 124.85 ± 16.21 W/cm^2 for a 1.5×1.5 cm^2 heater surface with etched surface nanostructures (Si nano-wires) while the values for plain Si wafer heaters were reported to be 46.82 ± 6.46 W/cm^2. In a follow-on study by the same research groups the heater size was varied from 0.5×0.5 cm^2 to 2×2 cm^2. The CHF values were found to increase dramatically as the heater size was reduced. Hence, this illustrates that in the "small heater" regime the boiling heat flux enhancements observed in the experiments can

be confounded by the effect of the heater size. This phenomena will be discussed in more detail in following sections [9].

From pool boiling experiments performed using aqueous nanofluids Kim et. al. [19] reported that CHF was enhanced by 170% and 180% for nanofluids containing TiO_2 and Al_2O_3 nanoparticles, respectively. Increasing the concentration of the nanoparticles was observed to marginally enhance the CHF values for TiO_2 nanofluids but was observed to saturate for that of Al_2O_3 nanofluids. Nanoparticle deposition on the heater wire surface was observed to occur in these experiments. When these heaters with nanoparticle precipitates were used for repeating the pool boiling experiments with pure water it was observed that the values of CHF were similar to that of the nanofluids experiments. This proves that the surface effects dominate over the bulk property values of the working fluid in enhancing CHF [19].

Sathyamurthi et. al. [25] performed pioneering pool boiling experiments using heater surfaces coated with multi-walled carbon nanotubes (MWCNT) on a flat silicon wafer using Chemical Vapor Deposition (CVD) techniques. Two different values of MWCNT thickness were employed in these studies. The thickness of the MWCNT coatings were chosen to be 9 micrometers (Type A MWCNT) and 25 micrometers (Type B MWCNT). Pool boiling experiments were performed for both nucleate and film boiling regimes for both saturated liquid and subcooled conditions. Type B MWCNT coatings enhanced the CHF in saturated boiling by 58% and Type A MWCNT coatings enhanced the CHF in nucleate boiling by 62%. This is the only report in the literature involving carbon nanotubes for both film and nucleate boiling regimes [25]. This study also

contradicted observations by Launay et. al. that CNT coatings improved boiling heat transfer values only at very low values of wall superheat. The experiments by Launay et. al. [29] involved carbon nanotubes (CNT) coatings on silicon surfaces that were etched to realize pin-fin arrays. Hence this technique enabled the fabrication of hierarchical (or hybrid) surfaces containing micro-sized pin-fins with nanocoatings on them.

In a separate study, Sathyamurthi et. al. [30] reported that Type B MWCNT yielded distinctly higher values of heat fluxes in nucleate and film boiling for saturated and subcooling conditions. Extending the height of the MWCNT only marginally increased the wall superheat required for attaining CHF. CNT coating on a bare silicon wafer was also reported to enhance CHF values by 63% at a liquid subcooling of 10°C [20].

El-Genk and Ali [17] performed saturated pool boiling experiments for PF-5060 on Copper heaters with micro-porous surface layers with varying thickness. The authors reported that the CHF values and the nucleate boiling heat transfer coefficient to be 40% ~ 75% higher than those reported on plane surfaces. The thickness of the porous layers were estimated to be 171 microns.

Ujereh et. al. [18] performed pool boiling experiments on heaters with patterned CNT arrays. The experiments were performed in the "small heater" regime for a heater size of 1.27 x 1.27 mm^2 involving both silicon and copper heater surfaces. While the authors reported enhancement in CHF and heat transfer coefficient values these results seem to be derived from confounded experiments – since the experiments were performed in the "small heater" regime. Silicon surfaces with CNT arrays showed higher levels of

enhancement compared to that of copper surfaces with CNT arrays. Since silicon surfaces were typically smoother and had less nucleation sites to begin with – CNT coatings were observed to cause higher level of enhancement in CHF. Coverage of CNT on the surface was also manipulated to understand the extent of the enhancement, but these experiments were inconclusive. Hence, the authors concluded that full coverage of CNTs on the heater surface is necessary for significant levels of enhancement in the boiling heat flux values. Rahman et. al. [31] performed pool boiling experiments using bio-templated nanostructured surfaces. Tobacco Mosaic Virus (TMV) was precipitated from aqueous solution and then coated with thin films of Nickel and Teflon in order to realize surfaces with different contact angles: super-hydrophilic (~9°), super-hydrophobic (~163°) and mixed hydrophilic-hydrophobic (~70°). Hybrid surfaces (Teflon and Nickel coatings on TMV) yielded lower levels of CHF enhancement (~70%) compared to that of a pure nickel coated surface (~140% enhancement) when compared to that of a pure Teflon coated surface.

Bubble dynamics on conventional heaters has been explored extensively in the pool boiling literature. However, relatively fewer reports exist in the literature for investigation of bubble dynamics on nanostructured heater surfaces (e.g., for bubble departure diameter or frequency correlations). Contemporary literature reports involving pool boiling studies on nanostructured heaters have mainly focused on the overall heat transfer enhancement (i.e., comparing pool boiling curves for nanostructured heaters with that of plain conventional heaters). Therefore, in this study, flow visualization experiments were performed to complement the boiling curves obtained for both plain conventional

heaters and heaters with nanostructures surfaces. The aim of this study is to enumerate the variations in bubble dynamics during pool boiling on different types of heater surfaces. The analyses of experimental data obtained from flow visualization experiments of bubble dynamics during pool boiling for various boiling regimes can provide additional insights into the non-linear coupling of the thermal and hydrodynamic transport processes. This can help resolve the discrepancies between the predictions obtained from traditional mechanistic models and the experimental observations involving nanostructured heater surfaces. It is expected that results gleaned from this study can enable the re-calibration of the traditional mechanistic models to enable predictions that better match the experimental measurements (involving pool boiling on nanostructured heaters).

Previous reports in the literature indicate that typically nanostructured heater surfaces dramatically enhance the values of CHF during pool boiling (compared to that of conventional plain heater surfaces). The dynamics of the bubbles on the nanostructured heaters are also altered significantly - resulting in smaller bubbles with higher values of bubble departure frequency and bubble nucleation density.

Experimental studies involving the boiling of electrolyte solutions such as NaCl ([32], [33]) provide insights about bubble departure diameter and frequency. Hamzekhani et. al, [32] used non-dimensional analyses (Buckingham's Pi Theorem) to derive a correlation for the frequency of the departing bubbles. Schulman, Cole, Rohsenow, and Ruckenstein developed correlations for various combinations of heater surfaces and boiling fluids ([34] [35] [36] [37]). Dong, et. al [26] considered the effects of micro-structured and nano- structured surfaces on critical heat flux. Force balance models were

used to predict the bubble departure diameter under microgravity conditions. Jensen and Memmel [2] briefly summarized the correlations that were culled from the pool boiling literature.

Literature review suggests that various parameters can affect the values of bubble departure diameter. Zhang et. al. [27] stated the influence of the buoyancy force, surface tension, viscous drag, inertia force, pressure difference, and the Marangoni force on the bubble departure diameter. In contrast, results reported by Kutateladaze and Gogonin [3] provided a different set of parameters that were expected to affect bubble dynamics in pool boiling. Zuber proposed a model based on hydrodynamic interactions and thermal boundary layer that blankets the growing bubble to predict the temperature distribution in the liquid surrounding the vapor bubble [38]. This approach enables the prediction of growth rate of vapor bubble – thus enabling an estimate for the growth time of the vapor bubble prior to departure. Peyghambarzadeh [33] identified several parameters that affect bubble departure diameter – which includes: the effect of physicochemical properties such as liquid viscosity, liquid density, and polarity of the liquid.

As mentioned before, nanostructured heater surfaces enable higher bubble departure frequency due to reduction in the bubble departure diameter that accrue from several factors [27]. Glenn [20] performed experimental validation involving bubble dynamics during pool boiling of refrigerant PF-5060 on a heater coated with multi-walled carbon nanotubes (MWCNT). The results showed significant reduction in the bubble departure diameter (by approximately 300%) on MWCNT coated heater surfaces. Glenn

also compared the experimental data with predictions from the literature derived from pool boiling experiments for measuring bubble dynamics on conventional heater surfaces.

The spatio-temporal variation in distribution of heat flux under each bubble leads to the corresponding spatio-temporal fluctuation of temperature distribution on the heater surface ([49], [52]). For example, local heat flux values are predicted to reach peak values ranging from 1 ~ 10 kW/cm^2 in the vicinity of the liquid-vapor contact line of the vapor bubble on the heater surface. Correspondingly, inversion of the temperature at this contact line occurs – which are termed as "cold spots". It is estimated that 60~90% of the total heat flux occurs in the cold spot region during film boiling and ~ 50% of the total heat flux occurs in the cold spot region during nucleate boiling. Hence the thermal diffusivity of the heater material plays a crucial role in transferring heat to the boiling fluid. For the same average value of wall superheat – copper heater yields higher values of pool boiling heat flux than steal heater since copper has higher values of thermal diffusivity. This implies that heaters with surface nanostructures having higher values of thermal diffusivities can yield higher values of pool boiling heat flux.

Pool boiling literature involving nanostructured heater surfaces are replete with reports suffering from the deficiency of employing "small heaters" [17] [39] [40]. This severely limits the veracity of the results since a small heater size can cause anomalous enhancement in the values of CHF (sometimes authors reported CHF values that exceeded the thermodynamic limit). The authenticity of these measurements then become questionable and lead to controversies among results reported by different research groups.

In summary, for studies reported in the literature involving nanostructured heater surfaces, while many studies delved into the nucleate boiling regime, there is a lack of attention to film boiling regimes in these experiments. The next section summarizes the other deficiencies in the literature reports on this topic.

1.3.1 Identification of Issues in Literature Reports

A significant number of experiments in the contemporary literature disregarded the effect of heater size as an important parameter for the design of experiments. Appropriate choice of heater size and shape is crucial for preventing the confounding of experiments. Heater size needs to exceed a specific threshold value in order to be categorized as the "large heater" configuration (also termed as "infinite size heater") where the heat flux values are insensitive to the variation in the heater size. For heater size below this threshold value – the heat flux values are sensitive to the variations in the non-dimensionalized value of the heater size. The heater size is scaled with the "most dangerous" value of Taylor instability wavelength (i.e., the instability wavelength corresponding to the highest growth rate) to obtain the non-dimensionalized value of the heater size. For example, Van P. Carey et. al. [9] reported significant enhancement in the values of CHF and heat transfer coefficient for heater sizes of 0.5×0.5 cm^2 when compared to that of 2×2 cm^2. These heater sizes are in the small heater regime and therefore the CHF measurements are highly sensitive to the variation in heater size. Similarly, Ujereh et. al. also reported dramatic enhancements in CHF values for a heater with the size of 1.27 x 1.27 mm^2 [18].

Because of these inadequacies in the design of experiments, there is a huge variance in the literature data for the range of enhancement for CHF and heat transfer coefficients involving nanostructured heater surfaces. To determine the appropriate heater size for the experiments, the values of capillary length scale (l_o) and the "most dangerous" Taylor instability wavelength (λ_d) need to be determined, as follows. These parameters are then used to determine the non-dimensional heater size *L'*, as defined below in Equations (6 – 8):

$$l_o = \sqrt{\sigma / g(\rho_l - \rho_v)} \tag{6}$$

$$\lambda_d = 2\pi\sqrt{3} l_o \approx 11\ l_o \tag{7}$$

$$L' = L/\lambda_d \tag{8}$$

The threshold value for "infinite heater" configuration is derived to be *L*' > 5 ([41] [42]). Once this configuration has been achieved (i.e., in the "large heater configuration" or the "infinite size heater configuration"), the heat flux values are expected to be independent of the variation in heater size. For liquids such as water or refrigerants (e.g., FC-72) the values of l_o are estimated to be 2.5 mm and 0.7 mm, respectively. Hence the value of "most dangerous" Taylor instability wavelength is expected to be ~ 1 cm for FC-72. To attain the large heater boiling regime during pool boiling of FC-72 the heater size needs to exceed 5 cm. The level of heat flux enhancements reported in the literature for small heater regimes therefore arises from two primary parameters – the non-dimensionalized values of heater size and the surface conditions of the heater. The

proportional contribution of each parameter on the total heat flux values (as well as level of enhancement) for each wall superheat value is therefore not known apriori. In addition, the λ_d for porous substrates is known to decrease by as much as ~20% [43] which can cause the values of L' to change significantly between the plain heater and heater with nanostructured surfaces (thus confounding the experimental results even further). Therefore, comparisons between pool boiling data of a plain heater and pool boiling data of a nanostructured engineered surfaces are incompatible unless both sets of the heater configurations are deemed large enough for negligible effect of the heater size (i.e., heater size scaled with the Taylor instability wavelength, which is expected to decrease by ~ 20% on nanostructured surface).

A significant number of studies in pool boiling literature only delve into heat transfer data in nucleate boiling, compared to film boiling. Out of all the reports culled for review, only two studies investigated film boiling heat transfer data ([25] [30]). Additionally, very few studies also reported differences between subcooled and saturated conditions for bubble dynamics ([20] [25] [30]).

The studies that were conducted on small heaters suffer from other deficiencies as well, including not achieving steady state conditions before performing experimental measurements (this creates a conundrum, as the veracity of the results become doubtful). The authors in these experiments inaccurately presumed that the steady state condition can be reached in a couple of minutes. It is absolutely essential that the existence of steady state conditions be verified for ensuring that the measurements are accurate and repeatable. Holistically, the pool boiling system typically has time constants of 1~2 hours.

Hence, the experiments need to be performed for a minimum of 2 hours to ensure that steady state conditions have been achieved. The erroneous design of experiments involving “small” heater size, coupled with experimental results being acquired when the apparatus has not reached steady state conditions can lead to unreliable observations and conclusions (also jeopardizing the repeatability of experiments). Caution must be exercised, because the temporal profile of heat flux or temperature variations for sub-components (such as the heater surface) can deceptively demonstrate steady state behavior, even though the test fluid and the cooling system may not have achieved steady state conditions. Small heaters can exacerbate this error further. Therefore, small heaters do not accurately display when steady state has been achieved for the data collection to be reliable or faithful to the actual conditions that are desired in the experiments. These improper practices compromise the reliability of the literature reports since the repeatability of the experiments are questionable and flawed data are produced that arise from the incorrect design of experiments.

Another factor of utmost importance along with heat flux measurements is the accurate recording of surface temperature values (i.e., by minimizing the values of measurement uncertainty for surface temperatures and wall superheat). These measurements for the wall temperature values are used for the generation of boiling curves. A problem with reports in the contemporary literature are the flawed approaches employed for measuring the wall/surface temperature. Often times, the wall heat flux values are used to calculate the wall temperature, and the wall temperature values are not measured directly. Some studies involved mounting of wire bead thermocouples for

surface temperature measurements. Such approaches for wall temperature values can often lead to disastrous inaccuracy due to nucleation of vapor bubbles induced on the wire bead themselves, since these thermocouples have large form factors. Therefore, the surface temperature values were not measured very meticulously in these literature reports. Thermocouples glued with an adhesive to the surface (sometimes very ill suited with poor thermal characteristics) generally create repeatability issues due to the uncontrolled contact resistance between the wire-bead and the heater surface. The thermal contact resistance values may also vary between experiments, adding on to the repeatability issues. An improved method for obtaining reliable measurements for surface temperature is therefore necessary.

Park and Taya [44] developed Thin Film Thermocouple (TFT) arrays, which measured heater surface temperatures at a high spatial resolution. These T-type thermocouples were 150 nm thick and arranged in a 10 × 10 array. TFT arrays were also used by other authors on different surface materials such as silicon wafers. The efficacy of these values were reported in prior work ([45] [46]).

This aim of this study is to continue the implementation of more reliable methods for recording surface temperature using TFT arrays. Previous studies have demonstrated the efficacy of these TFT arrays for pool boiling on rectangular flat horizontal heaters [30]. Along with this verification, fractal/ chaotic features in pool boiling have been investigated [47].

Since heaters with nanostructured surfaces are considered to be an attractive option for enhancing thermal management using pool boiling (e.g., for electronic chip cooling

applications) – it is essential that experimental validation be performed for various correlations in the literature on bubble dynamics during pool boiling on various types of nanostructured surfaces. The applicability of these correlations for reliably predicting the bubble dynamics on nanostructured surfaces need to be established, especially since these correlations in the literature were essentially derived from experiments performed for various conventional heater surfaces (and it is not clear if these correlations can be extended to performing predictions for bubble dynamics on nanostructured heaters). Such studies for experimental studies involving flow visualization measurements of bubble dynamics are currently lacking in the pool boiling literature despite the numerous pool boiling heat flux measurements that were reported for various types of heaters with nanostructured heaters. Hence, the scope of this study is focused on measurement of bubble departure diameter and bubble departure frequency values for various regimes of pool boiling (i.e., at different values of wall superheat and liquid subcooling). The flow visualization experiments for film boiling also enabled the measurement of bubble growth as a function of time for conventional heater surfaces (plain silicon wafers and copper heaters) as well as nanostructured heater surfaces (involving Anodized Aluminum Oxide or "AAO" surfaces). Hence, the results from this study can enable the identification of appropriate correlations to estimate the bubble dynamics for various regimes of pool boiling on conventional heaters and heaters with nanostructured surfaces.

1.3.2 Use of Thin Film Thermocouple Arrays (TFTs)

A repeatable procedure developed by Sinha [48] for fabrication of thin film thermocouples was used for surface temperature measurement during the various boiling regimes. Thin film thermocouples are known to have reasonable measurements at quick response rates, justifying their implementation in this study. Fabrication was performed using multilayer photolithography and metal deposition followed by the "lift-off" process. Sathyamurthi [49] reported the high frequency response in TFTs due to low thermal inertia can be of the order of MHz. These thermocouples can be located where normally beaded thermocouples would interfere with the measurements. Additionally, the small feature size (form factors) and low thermal inertia helps to minimize disruption and distortions of the velocity and temperature fields measured in these studies. Ahn et. al. [50] verified the existence of "cold spots" on a heater surface exposed to a boiling liquid by measuring the temperature fluctuations using these "nano"-thermocouples, which were termed as "Thin Film Thermocouples (TFT)". The later sections provide descriptions of the fabrication and packaging as well as calibration and testing of these TFT arrays.

1.3.3 Nanofin Effect

In the past decade several experiments were reported on the measurement of anomalous enhancement in heat flux during pool boiling on horizontal heaters with nanostructured surfaces. Results from several studies demonstrated that heater surfaces involving nanostructures composed of materials with lower thermal conductivities resulted in higher values of heat flux. Singh and Banerjee [51] pioneered the thermo-

physical model called “nano-Fin Effect (nFE)” for resolving the conundrums associated with the anomalous enhancement in nano-scale heat transfer during pool boiling on nanostructured heaters. nFE models can also be used for resolving and predicting the anomalous enhancement in the thermo-physical properties of nanofluids (as well as resolving the controversies associated with both enhancement and degradation in convection heat transfer involving nanofluids under similar conditions). The authors demonstrated that nano-fins (or heaters with nanostructured surfaces) with lower thermal conductivity materials can sometimes enable higher values of CHF – since the dominant parameter affecting CHF in pool boiling is the interfacial thermal resistance at the solid-liquid interface (this is also known as the “Kapitza Resistance” and denoted as R_k). A major proportion of the total thermal resistance involving nanofins is R_k and this is the most dominant parameter that controls the heat flux at the nano-scale. A consequence of nFE is the enhancement of specific heat capacity of nanofluids (i.e. colloidal suspension of nanoparticles). Interestingly, predictions from nFE implies thermal diodes exist at the nanoscale where – for the same temperature difference between the solid and fluid phases – the heat flux is higher for cold fluids compared to hot fluids when exposed to nanoparticles or nanofins (i.e., nanostructured surfaces).

In order to determine the overall effect of the Kapitza resistance, numerical simulations have been performed for studying the thermal boundary resistance between the interfaces. Non-equilibrium methods in molecular dynamics simulations are utilized to calculate interfacial thermal resistance. The lumped capacitance model provides a convenient strategy for estimating the temperature distribution between a nanofin and the

surrounding fluid. Various researchers have also studied solid-liquid interactions to determine how intermolecular forces between the liquid and solid atoms play a key role in determining the interfacial thermal resistance. The chemical composition and chemical structure of the fluid molecules also play a dominant role in modulating the resulting interfacial thermal resistance values. The resistance values are strongly dependent on the vibration frequencies of the atoms in the fluid molecules and test fluid. Molecular structures of the boiling surface can also modulate the interfacial thermal resistance (e.g., due to the variation in the length of polymer chains, presence of isomers, or proportion of the different chemical structures of the molecules in the mixtures). Energy can be transferred through Van der Waals interactions. This interaction is considered to be one of the primary mechanisms of the total thermal energy transferred from nanofins or nanoparticles to the fluid molecules. Also, chemical concentration gradients induced by the nanostructures can also lead to a concentration gradient mediated heat transfer process (i.e. thermophoresis).

Due to surface adsorption of the fluid molecules on a solid (e.g. on nanoparticles and nanofins) a semi-solid phase of fluid molecules with higher density (also called as "compressed phase") is expected to form on the surface of the nanostructures. The density of this newly formed phase was often found to match the solid phase density of the solvent material (i.e., the bulk fluid phase). The adsorption of the solvent molecules on the nanoparticle surface therefore also induces concentration gradient for the molecules in the fluid phases [51].

Three different mechanisms arise from the complex interactions during energy transfer. The first is the interfacial thermal resistance, as previously discussed, the second is thermal capacitance from the fluid molecules forming a compressed layer, and the third is the bias in heat transfer values (or diode effect) based on direction of the temperature drop. This bias is driven from the concentration gradient of the fluid molecules to the bulk fluid from the solid nanofin surface. The diagram below depicts how thermophysical interactions between the nanofin interface and fluid molecules may occur.

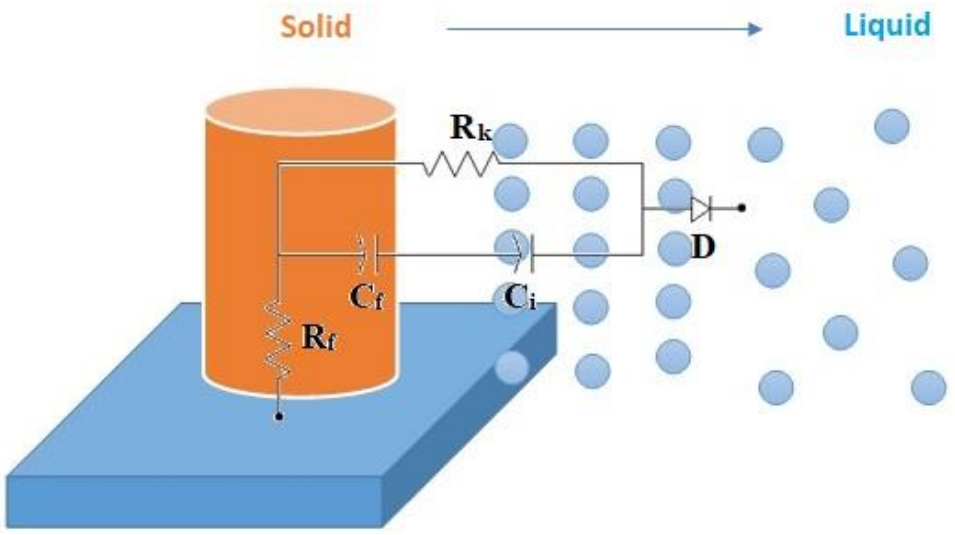

Figure 1-2 Schematic representing the thermal/electric network of the interactions between the solid and liquid molecules. Rk represents interfacial thermal resistance, Rf represents thermal conduction resistance of solid, Cf represents thermal capacitance of nanofin, Ci represents thermal capacitance of compressed layer, and D represents the thermal bias of the compressed layer.

Inter-molecular interactions between the nanofin structure and fluid molecules (also referred to as solvent molecules) can cause density oscillations for the number of

molecules per unit volume. Molecular dynamics simulations (MD) have shown that fluid molecules are attracted to the nanofin surface (solid wall) which can create a layer of semi-solid phase on the nanofin surface, which is also called the “compressed layer” [51]. This layer has a density that is different than the bulk of the fluid phase. The nanofin thus induces the formation of a third phase with a higher chemical potential or concentration than the bulk phase of the fluid. Additionally, this layer can also have a different specific heat capacity and thermal conductivity, causing another mechanism for thermal energy storage. This mechanism lets the additional chemical potential induced by the nanofins to act effectively as a thermal capacitor. The MD simulations have shown that the compressed layer of the fluid molecules has a higher thermal capacitance, primarily because of the higher density than the bulk fluid [52].

Compressed layer formation can occur due to the adhesive inter-molecular forces between the liquid and solid phases. Wetting on the solid surface from the fluid can occur if the adhesive forces are higher than the cohesive forces, or the inter-molecular forces between molecules of the same species. MD simulations gave results for compressed layer thicknesses with different fluid-solid combinations. These simulations were also used to determine density oscillations for the compressed phase with different materials. Different density profiles were analyzed by Yang [52] for nanofins with SiO_2, Si, and Ni. While the material properties for the fluid were unchanged for each simulation, the density oscillations were observed to vary significantly (for the compressed phase). This shows that the material property of the nanofin can modulate the properties of the semi-solid phase formed by the fluid molecules. The variation in the

density oscillations were dependent on the inter-molecular interactions (which varied with the composition of both the liquid phase and the solid phase). Figure 1-3 below demonstrates the variation of the density profiles for different nanofins [52].

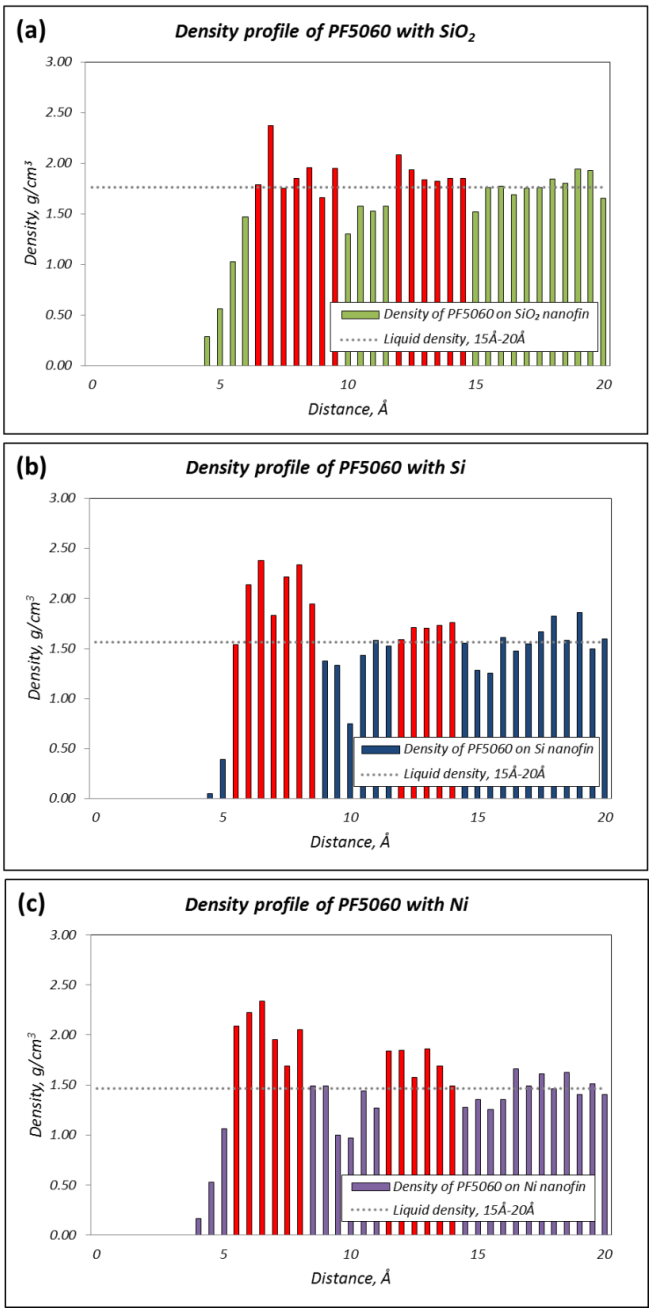

Figure 1-3 Comparison of density oscillations between (a) NiO2, (b) Si and (c) Ni and the fluid solvent phase. The regions marked in red are the compressed phase of the surface. Plots courtesy of Dr. H. Yang [52].

The following transport mechanisms modulate the magnitude of heat transfer in a fluid medium:

1.) Conduction or temperature gradient (modeled by Fourier's Law)
2.) Mass transfer or diffusion through the chemical concentration gradient (modeled by Fick's Law, or "Sorret effect"), or
3.) A combination of the two (also called the "Duffour effect").

Different situations can arise with these transport mechanisms, involving both a temperature gradient and a concentration gradient oriented in the same direction, or the temperature gradient and concentration gradient oriented in opposite directions. When each of these gradients are oriented in opposite directions, the net heat transfer is impeded Two specific cases are outlined in which the situations mentioned above can occur:

Case 1: Heat transfer from the hot solid nanoparticle or nanofin to the cold liquid. Temperature and concentration values decrease away from the solid surface. Heat transfer and mass transfer due to the temperature gradient and concentration gradient respectively are oriented in the same direction.

Case 2: Heat transfer occurs from hot liquid to cold solid nanoparticle or nanofin. In this case, the temperature gradient for conduction heat transfer is oreinted in the opposite direction from the concentration gradient for mass diffusion. The temperature gradient induces conduction heat transfer from the liquid to the solid, while the concentration gradient decreases from the solid to the compressed layer of the fluid (with higher chemical potential).

Figure 1-4 below demonstrates how the two cases can impact energy transfer.

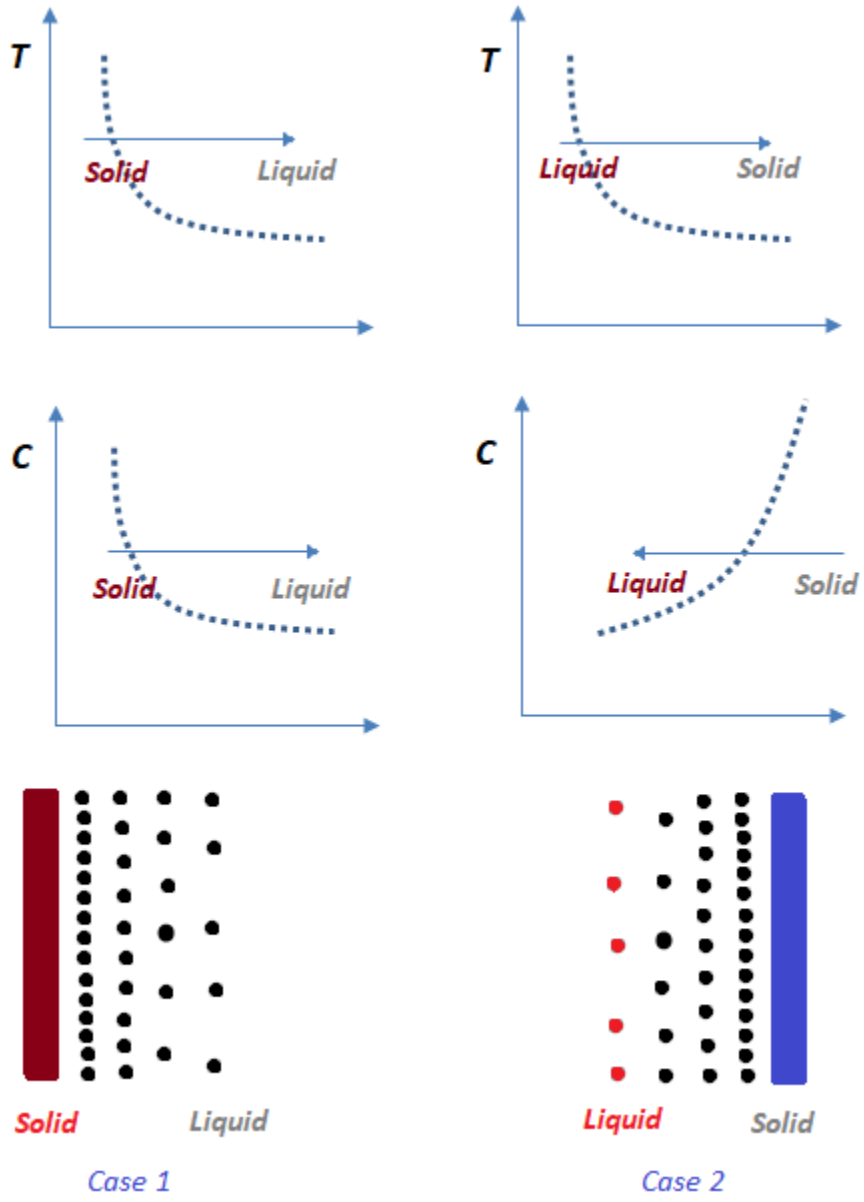

Figure 1-4 Diagram depicting heat transfer mediated by a temperature gradient and a concentration gradient. Both solid and liquid phases are represented, and the dark circles represent the molecules in the compressed layer.

Therefore, the net heat transfer cannot be the same for both of these cases. The heat transfer from the hot solid to liquid in Case 1 is hypothetically higher than the heat transfer from the hot liquid to the solid in Case 2. Hence, this acts as a thermal diode where the magnitude of heat transfer is different in two directions (for the same temperature drop) [52].

1.4 Motivation and Goal

This study is motivated by the urgent need in various engineering applications (such as thermal management applications) for enhancing pool boiling heat flux. Several studies have demonstrated anomalous enhancement in the pool boiling heat flux on nanostructured heater surfaces. The hydrodynamic interactions involving bubble dynamics have not been explored extensively in the literature. This is a large gap in understanding the transport phenomena associated with pool boiling heat transfer. Insights into the bubble dynamics during pool boiling on heater surfaces with nanostructured surfaces can enable the development of optimized engineered surfaces for maximizing heat flux in pool boiling which can enable the development of energy efficient devices and thermal systems.

Hence, the goal of this study is to analyze pool boiling experimental data involving both heat flux measurements as well as flow visualization experiments performed using high speed and high resolution digital image acquisition apparatus for the purpose of gathering insights into the dynamics of bubbles in various pool boiling regimes. This will also help to correlate the behavioral information regarding bubble dynamics in various

pool boiling regimes with the resulting heat flux values. This study is focused on performing experimental validation of the various correlations in the literature (that were obtained from experimental data involving conventional heater configurations). This study will enable the identification of the appropriate correlations that can reliably predict bubble dynamics during pool boiling on conventional heaters as well as heaters with nanostructured surfaces. This study will also help to calibrate the correlations that are most appropriate for these configurations.

A function structure depicting various transport mechanisms and experimental parameters involved in pool boiling is shown in Figure 1-5. The first bottleneck in the transfer of heat from the nanostructured surface to the surrounding fluid is governed by the nano-Fin Effect (nFE). As mentioned before, nFE comprises of several interfacial thermal impedances – which includes: (1) interfacial thermal resistance (or "Kapitza Resistance", R_k); (2) interfacial thermal capacitance (due to surface adsorption of fluid molecules at the solid-fluid interface); and (3) interfacial thermal diode (due to concentration gradient induced in the fluid phase caused by surface adsorption of fluid molecules on the nanofins). The interfacial resistance as well as interfacial capacitance are in parallel (since they occur across the same temperature drop) and are in turn, in series with the interfacial thermal diode. It can be expected that during pool boiling heat transfer from the surface nanostructures to the fluid molecules is primarily modulated by the interfacial impedances, that is modeled by the "nano-Fin Effect (nFE)" – following which - secondary thermal impedances govern the thermal and hydrodynamic interactions (such as fluid wicking). The heat transferred to the fluid phase results in the generation of an

ensemble of molecules with high kinetic energies, which in turn leads to the formation of liquid-vapor interfaces. In this process, a critical ensemble of fluid molecules (exceeding the threshold kinetic energy necessary for the inception of vapor bubble) congregate in clusters of different sizes. Clusters of these molecules that exceed a critical size lead to the nucleation of individual vapor bubbles through the formation of a vapor-liquid interface (or meniscus). At this stage several parameters affect the further transport of mass and thermal energy – which includes: transient heat transfer (formation of thermal boundary layer), latent heat of evaporation (evaporation resistance), capillary wicking (i.e., "wickability" of the nanostructures), as well as bulk fluid convection induced by periodic formation, growth and departure of vapor bubbles in the liquid pool.

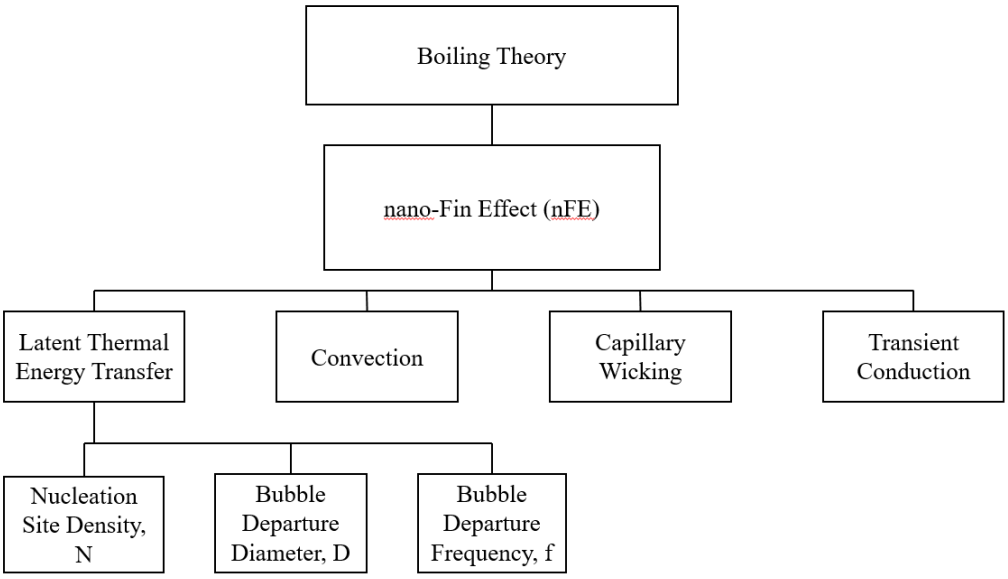

Figure 1-5 Function diagram showing the relation between different transport mechanisms for pool boiling on nanostructured heater surfaces.

1.5 Objective

Equation 1 shows that for boiling regimes dominated by latent heat transfer – the most sensitive parameter is the rate of vapor generation on the heater surface (since, vapor density and latent heat capacity are properties of the fluid). This implies that three variables enumerated in Equation 2 determine the rate of vapor generation: N, d_D and f. The nucleation site density (N) depends on the manufacturing process employed for fabricating the heater surface and is therefore not a focus of this study. Therefore, the objective of this study is to perform experimental measurements for pool boiling heat flux in various boiling regimes as well as perform flow visualization experiments of bubble dynamics on the heater surface in order to determine the effect of heater configuration (e.g., plain silicon wafer, bare copper surface and AAO nanostructures) on the bubble departure diameter (d_D) and bubble departure frequency (f). In a few of the flow visualization experiments for film boiling regime the experimental data for bubble height as a function of time were also obtained. This enabled the estimation of the history of growth rate of the vapor bubbles after inception and before departure from the heater surface.

1.6 Scope

Pool boiling experiments were performed using refrigerant (PF-5060, Manufacturer: 3M Corp., Minneapolis, MN) for liquid subcooling of 5°C and 10°C at atmospheric pressure conditions involving three different configurations of horizontal heaters: bare copper, plain silicon wafers, and Anodized Aluminum Oxide (AAO). Boiling

curves were plotted based on the measured values of heat flux that were obtained at different values of wall superheat. The boiling curves generated in this study were compared with literature data to benchmark the performance of the plain heaters and heaters with nanostructured surfaces. To assess the repeatability of the experimental data – two sets of experiments were performed for each boiling curve. Experimental data were recorded for both nucleate boiling and film boiling regimes.

A digital flow visualization apparatus was used to record bubble dynamics on the heater surface using a high speed digital camera (500 ~ 1000 frames/ second) and at high resolution (0.5 ~ 1 Mbyte/ frame). The digital images were then analyzed using image processing tools to measure the bubble height as a function of time (in film boiling regime) as well as the bubble departure diameter (for both nucleate and film boiling regimes). The temporal sequence of the digital image data was also used to estimate the growth time of bubbles as well as the bubble departure frequency at a particular location. The results from the AAO heater was compared to that of the bare heaters (copper and silicon wafer) to determine the effect of the nanostructures on bubble departure diameter and bubble departure frequency (especially in nucleate boiling regime). These measurements are analyzed in the discussion section of this publication to explore potential causality for the observed changes in the bubble dynamics on the plain and nanostructured heaters. The experimental results were also compared with predictions obtained from correlations in the literature with the objective of identifying the correlations that are most consistent for predicting the bubble dynamics on each of these three heater configurations.

1.7 Overview

The fabrication techniques for the Thin Film Thermocouple (TFT) arrays for surface temperature measurements are described in Chapter II. A brief description of the experimental apparatus is provided in Chapter III followed by the description of the experimental procedure that was utilized to obtain the experimental data analyzed in this study. In Chapter IV experimental data was analyzed and the nuances of these results were discussed, which include:

(1) Heat flux was plotted as a function of wall superheat and liquid subcooling (boiling curves);

(2) Measurements for bubble height as a function of time (for film boiling regime), as well as bubble departure diameter and bubble departure frequency (for both nucleate and film boiling regimes);

(3) The estimates for the measurement uncertainty of these experimental data.

The results are summarized and conclusions derived from this study are provided in Chapter V. The detailed results from this study are listed in tables and in appendices at the end of this publication.

2 MICRO/NANO-FABRICATION PROCEDURE

2.1 Thin Film Thermocouple Fabrication

Thin Film Thermocouple (TFT) arrays were fabricated using conventional photolithography techniques. Thermocouples are used extensively for temperature measurement in various engineering applications. The thermoelectric effect (or Seebeck effect) is the governing principle for the operation of thermocouples. The Seebeck effect is used to calculate the magnitude of the electric potential between two junctions of different conducting materials in mutual contact (thermocouples) where the generated electromotive force (emf) is proportional to the temperature differential between the two junctions (and the constant of proportionality is termed as the Seebeck coefficient). This effect is leveraged for temperature measurements to be performed by measuring the voltage that is generated between two pairs of thermocouples maintained at different temperatures. Calibration of thermocouples affords better accuracy of the temperature measurements. Therefore, each pair of electrical junctions (composed of two different electrical conductors) that are used to measure voltage as a function of temperature difference is formally known as a thermocouple.

Various materials are selected as thermocouples (such as pure metals or alloys) depending on the temperature range desired for the specific operation. For this study, K-type thermocouples were used. K-type thermocouples involve the junction of Chromel (90% Nickel + 10% Chromium) and Alumel (95% Nickel + 2% Manganese, 2% Aluminum and 1% Silicon). K type thermocouples are typically used for temperatures ranging from 0°C to 1100°C. Therefore, in this study the K-type thermocouples were

selected as the components for nanofabrication of the Thin Film Thermocouple (TFT) arrays. Since thermocouples were needed to measure surface temperature during boiling, conventional wire bead thermocouples would not be appropriate, due to their large form factor (size) which can cause disruptions of the transport mechanisms and affect the surface temperature transients of the heater surface. Erroneous measurements would then occur with inaccurate temperature fluctuations, especially for the wall temperature (T_w) measurements. Therefore, Thin Film Thermocouple (TFT) arrays were fabricated since they enable temperature measurements with high spatial and temporal resolution. Such measurements can then be utilized to estimate the temperature gradients and transient rates. The TFT thickness was limited to 200 nm to minimize any perturbations of the transport mechanisms during pool boiling. If the thickness of TFT were chosen to be below 200 nm, the junction would cease to behave like a thermocouple because of scattering effects involving phonons. Figure 2-1 shows the processing steps that were used for TFT fabrication. TFT array fabrication was performed at the Materials Characterization Facility (MCF) at Texas A&M University. The author acknowledges the help of Dr. Hongjoo Yang, Mr. Binjian Ma, and Mr. Yi Wang for the micro/nano-fabrication of the TFT arrays on silicon wafers that were used in this study.

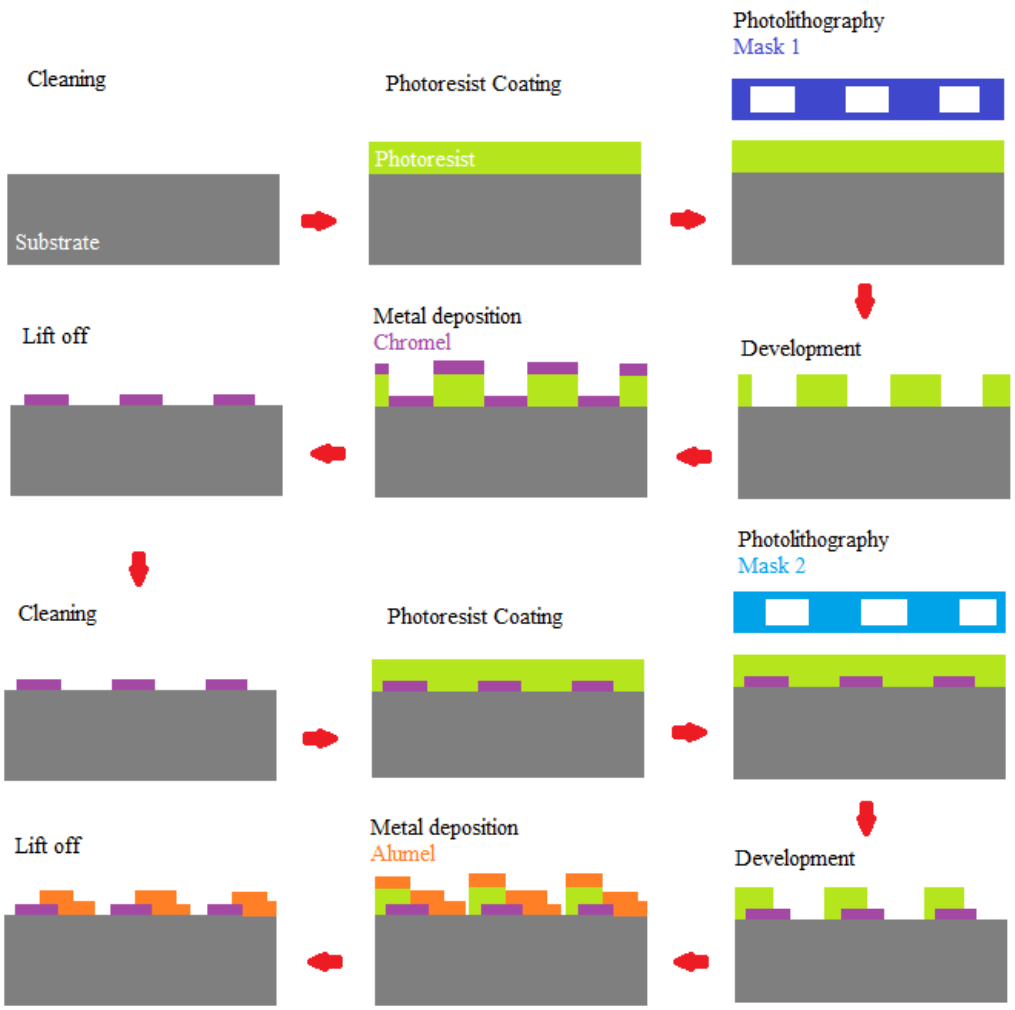

Figure 2-1 Schematic showing the processing steps for nanofabrication of Thin Film Thermocouples (TFT) arrays.

2.1.1 Photolithography

Two different layouts were designed for the photomasks for the nanofabrication of the arrays of chromel and alumel junctions. Commercial printing services (Southwest Printing, Bryan, Texas) was used for obtaining the desired photo-film masks. The

photolithography for the Chromel and Alumel layers were completed at the Materials Characterization Facility (MCF), at Texas A&M University. The steps for a typical photolithography process involve designing the layout of the patterns, printing out the mask through printing services, cleaning the wafer, photoresist spin coating, photo exposure (UV), curing and development of the exposed photoresist with the desired layout. These steps are very important for making the TFT arrays. Potential malfunctioning of the TFT junctions may occur if the photoresist pattern is not developed properly on the wafer substrate, causing the Chromel and Alumel metal patterns to be defective. Table 2-1 lists the details of the processing conditions [52].

Table 1 Photolithography recipes for TFT Fabrication [52]

Dry Cleaning	Reactive Ion Etcher		Bake	Hot Plate	
	Power	350 W		Temperature	115°C
	Time	5 min		Time	1 min
	O_2	20 sccm			
			UV exposure	Mask Aligner	
Spin Coating	Spin Coater			Power Density	14 mW/m^2
	Speed	3000 rpm		Time	1 min
	Time	1 min			
	Acceleration	500 rpm/s	Development	Time	1 min

2.1.1.1 Mask Design

Two different layouts (patterns) were used for printing the photomasks for fabricating the Chromel and Alumel junctions. The patterns typically used are shown in Figure 2-2 below for the masks used to pattern the chromel and alumel layers [52].

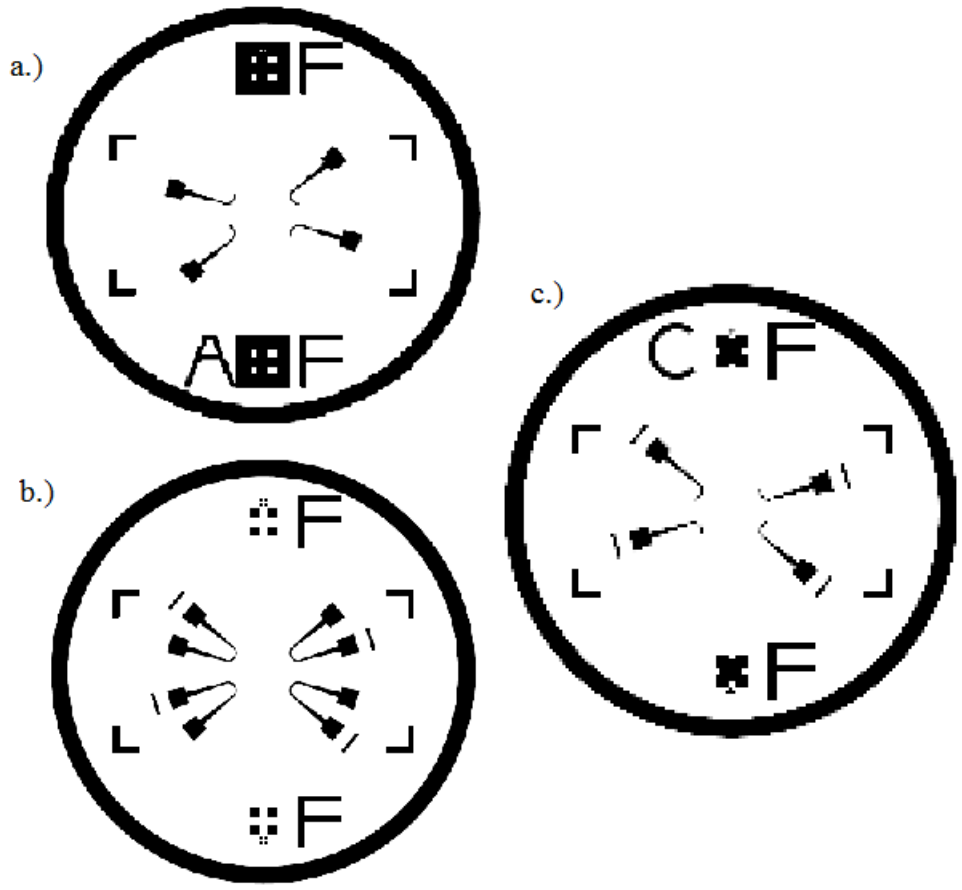

Figure 2-2 Photomask layouts for the silicon wafers depicting the: (a) Alumel layer, (b) combined layout, and (c) Chromel layer . Figures courtesy of Dr. Binjian Ma and Dr. Yang [52].

The 3 inch wafers were used for performing control experiments (without any nanostructures on the surface). The two metal layers were aligned for realizing the thermocouple junction using alignment patterns designed in the two mask layouts. Computer Aided Design (CAD) tools were used for designing the layouts of the photomasks (e.g. Solidworks v2010, Dassult Systems). The desired critical dimension was 200 nm for the chromel and alumel junctions. Bond pad arrays were designed in the layout

for connecting the thermocouple junctions to the data acquisition systems. These bond pads were designed to be about a 1 mm square. The thermocouple wires were connected to the bond pads (e.g., using conducting adhesives) for digital data acquisition of sensor measurements and automated recording of the temperature values.

2.1.1.2 Wafer Cleaning Step

The wafers (which were produced by commercial vendors) can potentially be contaminated from undesired chemical exposure or dust from the atmosphere, so wafer cleaning is a very important step. Acetone, DI water and oxygen plasma Reactive Ion Etch (RIE) are used for the initial cleaning steps for the wafer. The wafer was immersed in an acetone and DI water solution, washed in DI water, and blow dried with compressed nitrogen gas. Then, the wafer was placed on a hotplate at 115°C for ten minutes to remove any remaining residual water. The Reactive Ion Etcher (CS-1701, March Plasma Systems) was used to remove organic residue.

2.1.1.3 Photoresist Spin Coating

For spin coating, a photoresist (Positive type, SC 1827, Rohm and Haas Electronic Materials) was used. A spin coater (WS-650S, Laurell) was used to obtain a desired photoresist thickness of 3 µm. The wafer was spin coated at 3000 rpm for one minute, based on the recipe supplied by the photoresist vendor. The wafer was then placed on a hot plate for one minute at 115°C for a pre-exposure bake. Table 2-1 in section 2.1.1. lists additional details about the processing conditions.

2.1.1.4 UV Exposure

After the wafer was coated with photoresist it was exposed to UV on a mask aligner (Q4000, Quintel). The UV exposure was performed for 1 minute to align the designed mask pattern with the wafer using an optical microscope. The chromel pattern did not require alignment (for the first mask), but the alumel pattern required very careful alignment (for the second mask) since the chromel pattern was already realized on the wafer (along with the mask alignment patterns already printed on the wafer surface from the photolithography step and liftoff that was already performed with chromel). The intensity of the UV light source was set at a value of 14 mW/cm^2. Table 2-1 lists additional details about the processing conditions.

2.1.1.5 Development

After UV exposure, the wafer was immersed in a developer solution (MF-319, Rohm and Hass Electronic Materials) for one minute to finalize the desired photoresist pattern. Since the photoresist was positive, the developer solution removed the exposed photoresist. Then, the wafer was rinsed thoroughly in DI water for one minute, and finally blow-dried with compressed nitrogen gas.

After the photolithography step was completed, the final pattern was scrutinized with an optical microscope to confirm that no defects were caused during the previous steps for the desired pattern on the wafer. If a defect was found, the photoresist was removed using a photoresist stripper solution, and the process steps were repeated from

the start. Additional details for the equipment used can be found on Texas A&M University's AggieFab Nanofabrication Facility website.

2.1.2 Physical Vapor Deposition (PVD)

For deposition using a thermal evaporator, metals with a high melting point cannot be considered. The metal alloys used in this study (chromel and alumel) have a high melting point, so an electron beam evaporator (CHA electron beam evaporator, CHA industries) was used for deposition, which was located at the MRC/NNIN node in the University of Texas at Austin. The photoresist pattern in the wafer was used for the deposition of the target metals and alloys [52].

An adhesion layer between the wafer substrate and the deposited metal thin films is often required to improve the yield of the batch fabrication process. Titanium is usually suitable for this function, and can be deposited at a 20 nm thickness prior to the target material deposition. Since the minimum thickness of the vapor film layer in film boiling is projected to exceed 10 μm [53], no significant perturbations from the TFT arrays (with 200 nm thickness) are expected to occur for the transport mechanisms in pool boiling in the film boiling regime. The ratio of the vapor film thickness to the thickness of the individual metal layers (i.e., the TFT array) is more than 50. Therefore, the thickness of the TFT array will have minimal impact on the vapor layers and are unlikely to cause disruptions or distortionsof the surface temperature measurements. The deposition rate of the metal layers was regulated at a value of 0.5 ~ 1.0 Å/s from established protocols for fabrication at MRC [52]. The quality and performance of the TFT arrays are highly

dependent on the quality of the deposited metals. The deposited metal layer is susceptible to the risk of peeling off during the lift-off process due to poor adhesion from unnecessarily high deposition rates. Most recipes involve deposition at 0.5 Å/s for metal thin films up to a 30 nm thickness. The deposition rate can then be increased to 1.0 Å/s for the rest of the metal deposition process.

2.1.3 Lift-off

The lift-off process was necessary for finalizing the pattern for the chromel or alumel layers. The substrate was immersed in a photo resist remover solution (PG remover, Supplier: Microchem Corp.) after physical vapor deposition to dissolve the remaining photoresist. While the deposited metal on the photoresist surface was removed, the metal deposited on the exposed wafer surface was not removed. The wafer is then immersed in an ultrasonic bath for 20 minutes until the excess metal was removed, or lifted off. Lastly, the substrate was cleaned off with DI water and blow dried with compressed nitrogen gas.

2.1.4 Characterization of Samples

Figure 2-3 below shows images of the wafer surfaces with patterned Thin Film Thermocouple (TFT) arrays. Surface micromaching techniques were used for ensuring the successful fabrication of the TFT arrays. The optical microscopy image in the figure shows the junction of the chromel and alumel layers obtained from this process. The procedure

for wire bonding onto the bond pads (packaging step) will be described in the following sections.

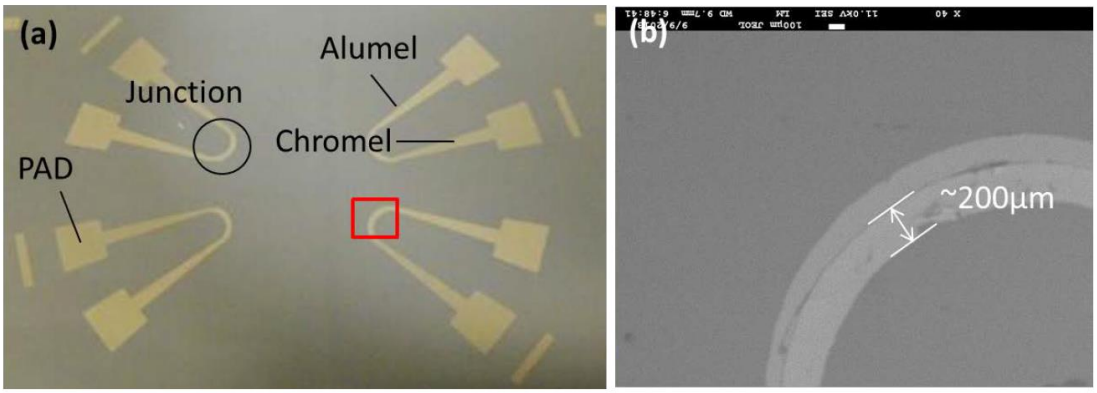

Figure 2-3 (a) Image of Thin Film Thermocouple (TFT) array on substrate, and (b) SEM image of chromel and alumel junction. Figure courtesy of Dr. Hongjoo Yang [52].

The image below in Figure 2-4 shows the TFT array on the Silicon substrate.

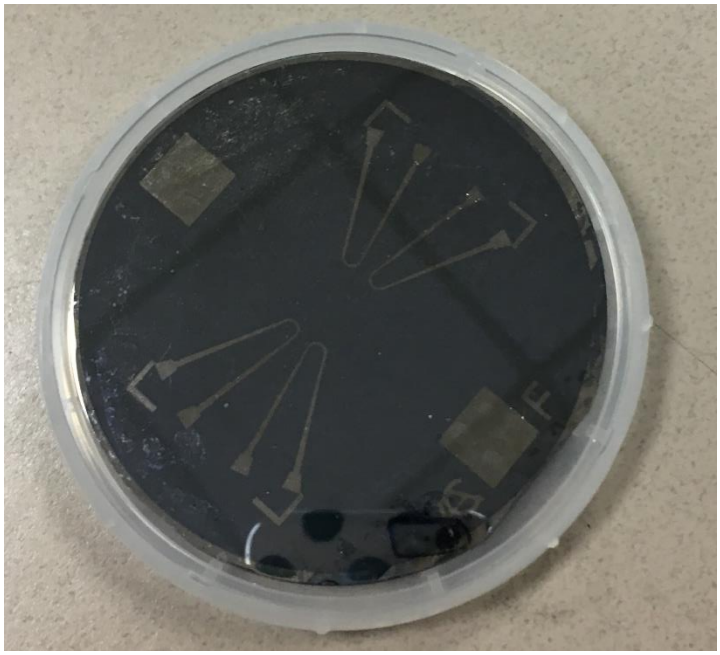

Figure 2-4 Image of TFT array fabricated on a plain Silicon surface. Figure courtesy of Dr. Hongjoo Yang [52].

3 EXPERIMENTAL STUDY

Dr. Hee Seok Ahn in 2005, a PhD student from the Multi-phase Flow and Heat Transfer Lab in the Mechanical Engineering Department at Texas A&M University, constructed the apparatus that was used for the boiling experiments in this study. The experimental apparatus includes a viewing chamber, a chiller unit, a data acquisition system, and a power supply. The test chamber that was used in these experiments consisted of a cube structure with about 15-20 cm on each side. The author acknowledges the help of Dr. Hongjoo Yang, Dr. Binjian Ma, and Mr. Yi Wang for the micro/nano-fabrication and packaging of the TFT arrays on silicon wafers that were used in this study as well as for assembling the experimental apparatus.

3.1 Packaging and Calibration of Thin Film Thermocouples (TFT)

3.1.1 Packaging of TFT

Various methods were available for the packaging of Thin Film Thermocouple (TFT) arrays to connect them individually to the data acquisition system (DAQ). The thermocouple wires were soldered on the bond-pads for the packaging step.

Nanofabrication of the TFT arrays was described in the previous chapter. K-type thermocouples were used for the assembly. These thermocouple wires (Chromel and Alumel, Supplier: Omega) were soldered with lead solder for connecting to the bond-pads. After the thermocouples were soldered, the silicon wafer substrate with the TFT arrays was heated to ~170°C on a hot plate, which corresponds to the melting point of the

soldered materials. An electrical connection was made by bonding wires to the thermocouples at the individual bond-pads and then the substrate was cooled to room temperature. In this step, the chromel bond-pad and the chromel wire were connected, and the alumel bond-pad and the alumel wire were connected, respectively.

Caution needed to be exercised while maintaining the wire assembly, as the electrical connections between the thermocouple and bond-pads were delicate. In addition, the soldered junctions were very fragile as well. Figure 3-1 shows a broken wafer with a TFT array.

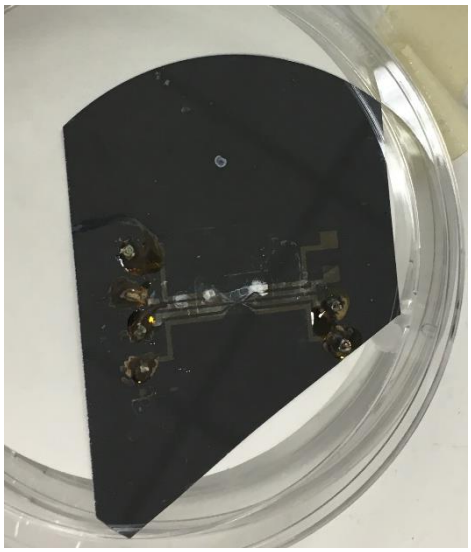

Figure 3-1 Image of a broken wafer substrate (with TFT arrays and soldered bond pads) due to mishandling. Courtesy of Dr. H. Yang [52].

3.1.2 Calibration of TFT

To begin the calibration, a commercial IR camera (FLIR i50, FLIR Systems) was used to obtain image of the thermocouples and for calibration. First, the emissivity of

silicon was culled from literature data [54] and this value was specified in the camera software. The silicon wafer substrate was then placed on a hotplate. Both the TFT and the images obtained from the IR camera were used to record the spatial variation of the surface temperature profiles. When the temperature readings were deemed consistent, a calibration curve was obtained. The calibration curves were observed to be linear and consistent for the range of temperatures measured in this study. Generally, room temperature (~290 K or 20°C) would be the lower limit and a temperature not exceeding 573 K (~200°C) would be the upper limit. The slope of the calibration curve was close to unity, and the R^2 was greater than 0.99. Figure 3-2 shows a representative calibration curve for the temperature readings and a sample picture of the surface obtained by the IR camera.

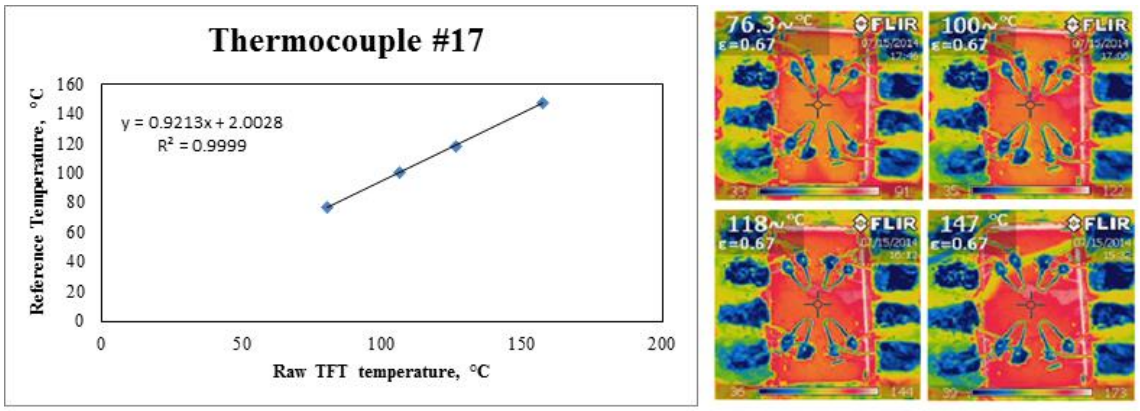

Figure 3-2 (a) Calibration curve for Thin Film Thermocouple (TFT) from IR camera images (b) Images recorded by the IR camera for surface temperature measurements. Figure courtesy of Mr. Navin Kumar.

3.2 Description of Experimental Setup

The main components of the experimental apparatus include: (1) a viewing chamber which contains the test surface and test fluid (and is covered with transparent Pyrex glass windows); (2) a chiller apparatus connected to an immersion cooling coil (for liquid subcooling); (3) power supply units which are connected to a calorimeter apparatus containing cartridge heaters inserted inside a copper block (and also includes wire-bead thermocouples for determination of the surface temperature and heat flux values); and (4) a data acquisition system (DAQ) for recording the temperatures from the thermocouples. Figure 3-3 shows the schematic for the apparatus. A high-speed digital camera (Fastec Imaging Corporation, Troubleshooter TSHRMS) was used for recording the videos for flow visualization. Images obtained from this apparatus were used to generate the data for the bubble growth rate, bubble departure diameter and bubble departure frequency.

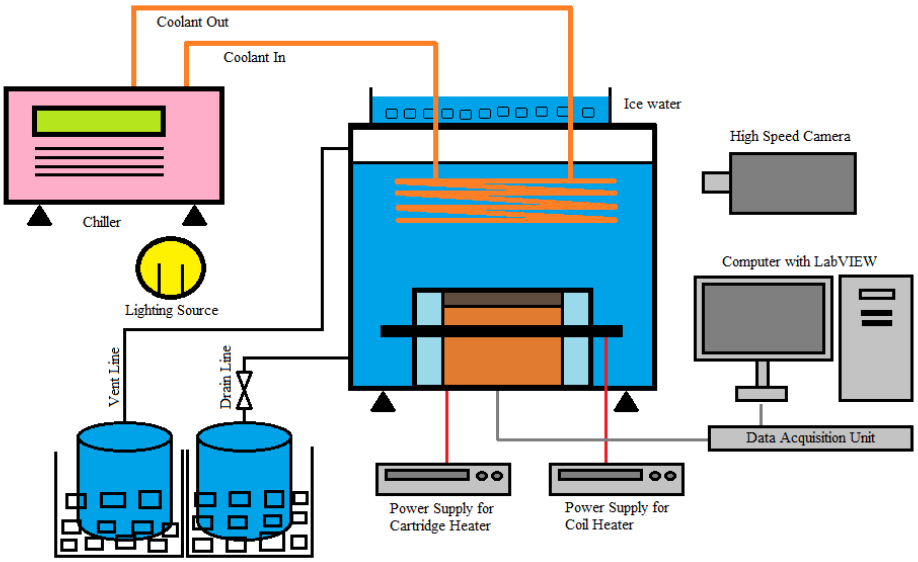

Figure 3-3 Schematic of the pool boiling apparatus.

3.2.1 Test Chamber

As shown in Figure 3-4, the cylindrical copper block has a diameter of 8.9 cm and a height of 5.1 cm. A concentric hollow stainless steel jacket with an insulated air gap surrounds the copper block. The copper block also contains 5 cartridge heaters, with three of them rated for 500 W and two of them rated for 300 W. Several bead thermocouples (K-type) were inserted into the copper block through holes machined into this calorimeter apparatus for the purpose of measuring the heat flux in the vertical direction (for estimating the boiling heat flux). Figure 3-4 shows the location of the thermocouples in the copper block. The copper block is fastened to the test chamber using six screws and leak proof gaskets (for better thermal insulation and isolation for the copper block) which are secured to the bottom steel plate of the test chamber. A stainless steel clamp is mounted

on top of the copper block/calorimeter apparatus and is also secured by screws on the steel jacket to hold test substrates (samples with or without the surface nanostructures).

Concentric to the cylindrical copper block within the boiling chamber, a coil heater is placed outside the steel jacket. This heater boils the test fluid (i.e., used before the start of experiments during the degassing step), which will be described in subsequent sections. In addition, if the cartridge heater does not provide sufficient power in order to reach the chosen bulk fluid temperature, the power output for the coil heaters can be adjusted to heat the working fluid.

The boiling test chamber is also covered with three Pyrex glass windows to allow for viewing of the test surface and the boiling fluid. The windows are sandwiched by silicone rubber gaskets to allow for insulation of the chamber, to prevent leakage of the working fluid from the test chamber. These silicone rubber gaskets are clamped using screws and steel plates.

As Figure 3-3 shows, ice water is placed on the outside top surface of the chamber. This ice water enables cooling of the top plate of the test chamber for condensation and recovery of the working fluid. The ice water is replenished periodically. A refrigerant (PF-5060) is used as the test fluid for these experiments. PF-5060 is expensive and highly volatile, necessitating recovery of the evaporated liquid during the boiling experiments. A collection bottle connected to the outlet port in the test chamber is used for recovery of the condensed PF-5060. The collection bottle is placed in container with ice water since the test chamber is surrounded by air at ambient temperature and maintained at atmospheric pressure. High-speed and low-speed digital cameras were placed facing towards the

boiling chamber for image acquisition (in flow visualization experiments). The videos were analyzed for locating the bubble nucleation sites, detecting bubble inception and calculating bubble growth rates, bubble departure diameter and bubble departure frequency.

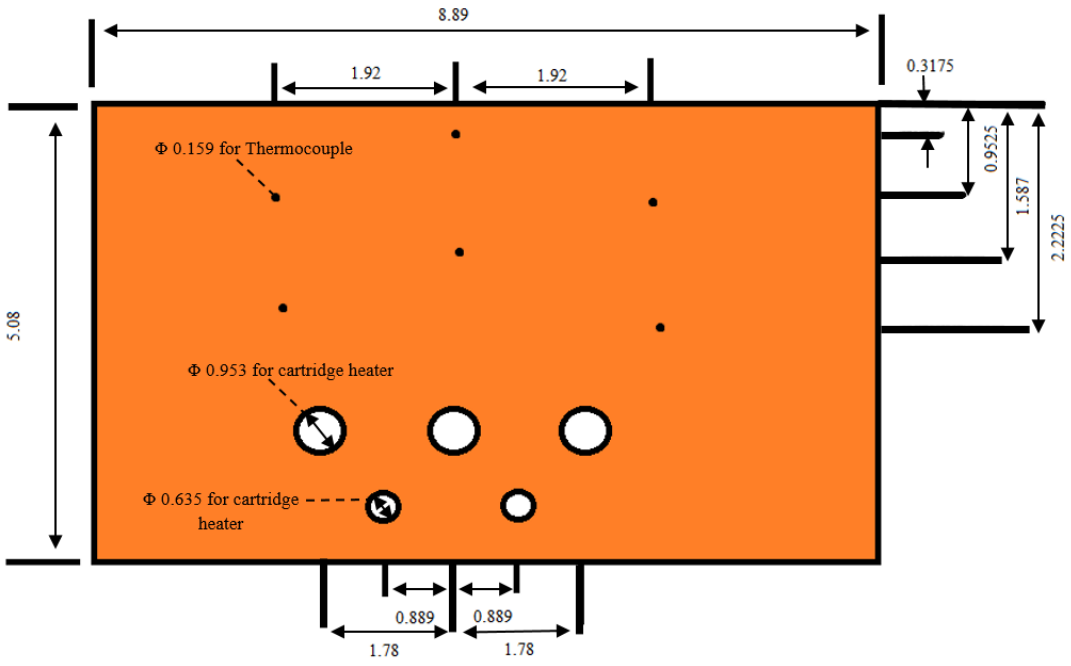

Figure 3-4 Diagram of the cylindrical copper block heater apparatus (Image not to scale, unit: cm).

3.2.2 Subcooling Apparatus

In this study, experiments were performed for either saturated or subcooled liquids. Liquid subcooling is defined as the temperature difference between the bulk or liquid pool temperature and the saturation temperature. For subcooling experiments, a cooling coil is immersed in the test fluid to reduce the bulk fluid temperature to the desired subcooling value. The chilled liquid (which is generally ethylene glycol or in this case – tap water)

flows inside the coiled copper tube and serves as a heat exchanger for achieving the desired subcooling. The cooling coil is connected to a chiller bath with adjustable temperature control (Mode: 9612, Manufacturer: Polyscience). Therefore, if the experiments were performed with 5°C subcooling, the bulk fluid temperature is maintained at 51°C, and if the experiments were performed at 10°C subcooling, the bulk fluid temperature is maintained at 46°C. Temperature for the bulk liquid was measured using wire-bead thermocouples placed close to the heater surface inside the test chamber. The bulk fluid temperature was maintained at a desired value by periodically adjusting the temperature of the chiller bath.

3.2.3 Power Supply Unit

Depending on the experimental conditions desired, the test surface is secured with steel clamps on the copper block heater/calorimeter apparatus. The power for the copper block is supplied by five cartridge heaters (3 each of 500W rating and 2 each of 300W rating) which are placed in the bottom portion of the copper block. The power supply is connected to these cartridge heaters (Manufacturer: Amrel, Model No.: SPS120-10-0020, Power rating: 1 kW). An ammeter is clamped on to the heaters to measure the current. The heater coil concentric to the steel jacket is connected to a rheostat to adjust energy input into the coil heater for heating the test liquid.

The heat flux was measured by a set of commercial K-type thermocouples that were inserted in to the copper block. The thermocouples were calibrated using a NIST

calibrated mercury thermometer by placing them in a water bath maintained at a constant temperature.

3.2.4 Data Acquisition Unit

A high-speed data acquisition (DAQ) system was used to record the temperature data obtained from the thermocouples. The components of the system are a NI SCXI-1102C terminal block and PCI-6251 DAQ board (Manufacturer: National Instruments, Austin, TX). A graphical user interface (GUI) was constructed using LabVIEW 71 (Manufacturer: National Instruments, Austin, TX) for automated control of the digital data acquisition. The temperature data from the thermocouples was acquired at 200 Hz. In conjunction, temperature data of the test surface was also recorded using TFT arrays. The GUI also helped in maintaining bulk liquid temperature so burnout conditions would not be reached. Figure 3-5 shows the boiling apparatus and its various components: the boiling chamber, the chiller unit, power supply unit and data acquisition unit.

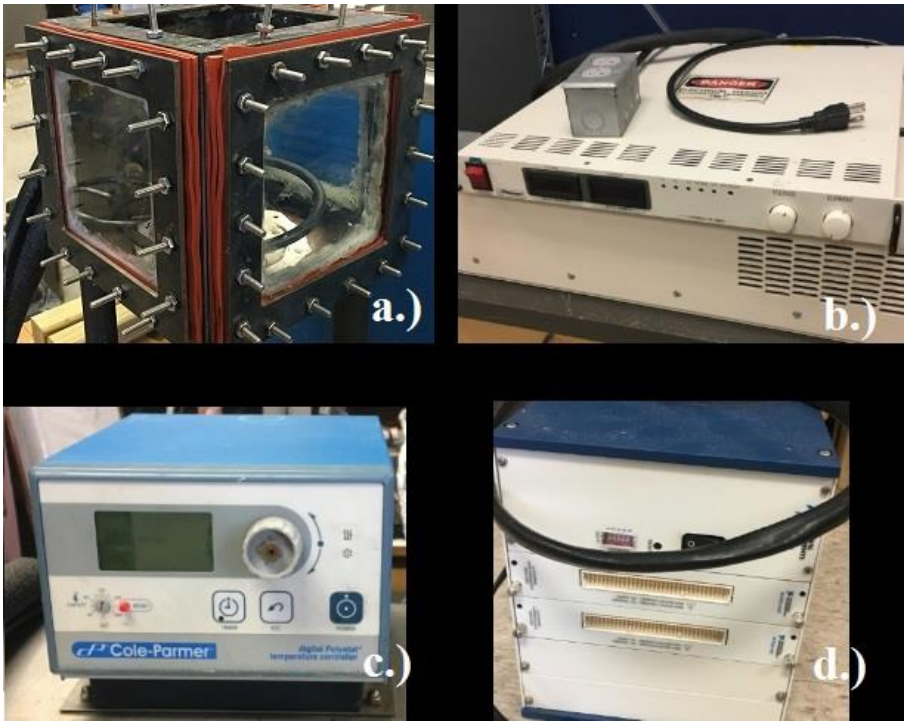

Figure 3-5 Images of the pool boiling apparatus: (a) viewing chamber, (b) power supply unit, (c) subcooling chiler unit, and (d) data acquisition unit (DAQ).

3.2.5 Test Samples

Since a test surface was not mounted for bare Copper experiments, the values for wall superheat and wall heat flux were analyzed from the thermocouple recordings in the Copper calorimeter apparatus. Plain silicon wafers and silicon wafers with TFT arrays (3 inch diameter) were also utilized for a separate set of experiments that were performed in this study. Both of these experimental sets were designed as a control to compare with the nanostructured surface (e.g., for studying the bubble dynamics).

Anodic Aluminum Oxide (AAO) surfaces were ordered from Synkera Technologies, Inc. The wafers were mounted on the copper cylinder using a steel clamp.

AAO surfaces provide high density, self-organized nanostructures which consists of cylindrical nanopores distributed uniformly on the surface. These pores are aligned perpendicularly on the surface of the AAO substrate. The aluminum pores form when the material is electrochemically oxidized, or anodized in specific electrolytes. Generally, the pore diameter is tunable from five to several hundred nm, with a pore areal number density that ranges from 10^{12} to 10^{9} cm^{-2}. AAO confers several advantages: it is optically transparent, electrically insulating, chemically inert, and thermally and mechanically robust [55]. Figure 3-6 shows the pore structures in the aluminum substrate, and the cellular matrix that forms after the anodization process.

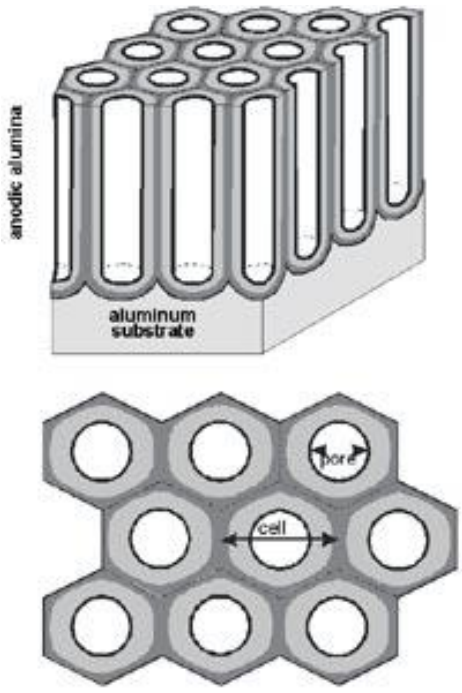

Figure 3-6 (a) Schematic for the structure of pores achieved through anodization of aluminum substrates, and (b) cellular matrix that forms after anodization. Picture provided by Synkera, Inc. [55] Cell size used for this study was 100 nm, pore size was 16 nm, and size of substrate was 5 cm x 2 cm.

3.3 Experimental Procedure

3.3.1 Test Surface Assembly

To assemble the test surface to the cylindrical copper block, a steel clamp was mounted on the silicon wafer and the AAO surface. The working fluid (PF-5060 Manufacturer: 3M Corp.) was poured in to the test chamber, thus covering the heater surface with sufficient depth from the free surface to the heater surface (~ 5 cm). Leakage of the working fluid from the test chamber was prevented by mounting the steel clamp, the steel jacket and the cylindrical copper block on Teflon gaskets.

In order to improve thermal contact between the test surface and the copper block, high thermal conductivity grease was applied (Model: 340 Heat Sink Compound, Manufacturer: Dow Corning). A torque wrench was used to ensure uniformity of pressure around the circumference of the clamp and test substrates. Figure 3-7 shows the assembly of the test surface in the test chamber.

Depending on the test surface, different clamp configurations are used for the study. While both are circular in shape, one steel clamp has a rectangular window of 31.8 mm × 58.7 mm in dimension, and the other steel clamp has a concentric circular window of 63.5 mm diameter. These different shaped clamps are used depending on which test surface is mounted in the boiling test chamber. The size of the opening in the clamp determines the size of the heater surface exposed to the working fluid during the boiling experiments.

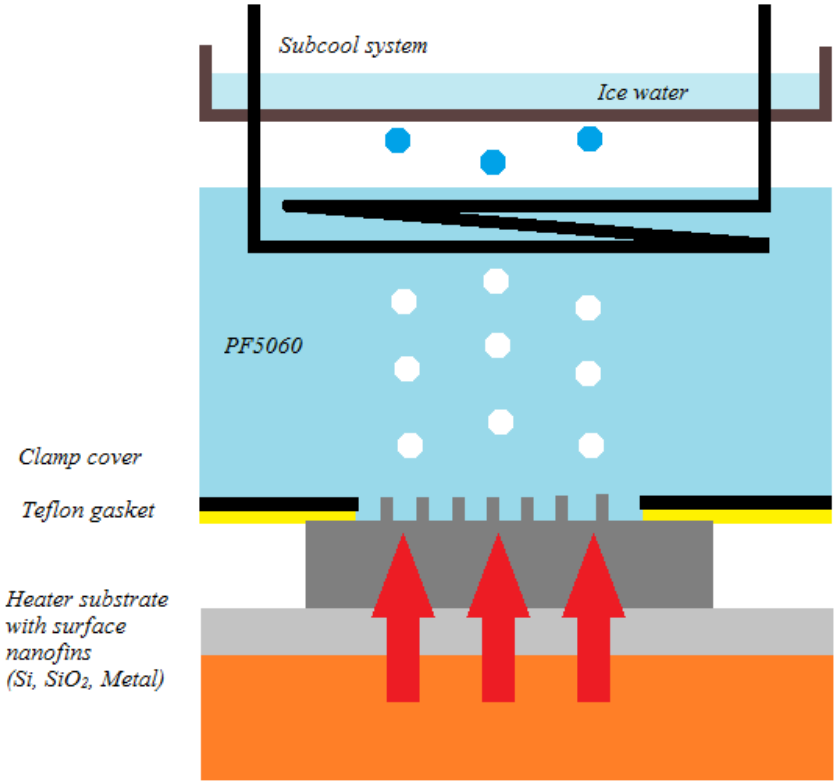

Figure 3-7 Schematic showing the assembly of the test surface during the pool boiling experiments.

3.3.2 Leakage Test and Degassing Step

Before commencement of any experiments leakage test was performed. DI water was poured into the test chamber. The bottom of the test chamber was monitored for leaks. If leaks were detected, a torque wrench was used to tighten a few of the six screws that are located on each side of the optical window and the steel jackets. Once the leakage test was completed, the water was drained and the water was allowed to dry from the test chamber by exposing it to the ambient air. Finally to complete the assembly the top steel

cover of the test section was mounted and the nuts were tightened to afford a good seal. Silicone glue was used to help seal the top steel cover to minimize vapor loss.

Air (and specifically oxygen) dissolves readily in the working fluid (PF-5060, 3M Corp.). This can be a nuisance for the boiling experiments as unexpected nucleation may occur and may slightly skew the results. Dissolved gases can reduce the wall superheat needed to initiate nucleation and erroneously modulate the heat flux at boiling incipience. In order to circumvent this, the test liquid was degassed before any experiment. This was completed by heating the test liquid to its boiling point (for PF-5060 the boiling point is 56°C under ambient conditions). During the degassing step the test liquid was heated using both the coil heater and the cartridge heaters. The total power applied from both of these heaters typically varied in the range of 300 W to 500 W. Thus, pool boiling would occur in the test chamber prior to the commencement of the actual experiments. This condition was maintained for at least three hours so trapped gasses would be removed from the cavities of the heater surface. The degassing step is necessary to ensuring repeatability of the boiling curves generated from the experiments, improve measurement uncertainty and thus the reliability of the experimental data generated from these experiments.

3.3.3 Heat Flux Calculation

By employing Fourier's Law of heat conduction the heat flux in the calorimeter apparatus can be estimated using the following equation [1]:

$$q_c" = k\frac{T_1 - T_2}{L_c} = \frac{k\Delta T}{L_c} \quad (9)$$

This equation is used to find the heat flux values in the axial direction of the cylindrical copper block, where $q_c"$ is the heat flux in the vertical direction, k is the thermal conductivity of copper, while T_1 and T_2 are the temperatures of the thermocouples aligned in the vertical direction within the copper block. ΔT represents the difference between in temperature between the two thermocouples that are aligned in the same vertical plane, and L_c represents a characteristic length or distance between the two thermocouples located and aligned in the same vertical plane. Once steady state conditions are achieved during the boiling experiments, the heat flux values are obtained using Equation (9), based on the temperature data recorded from the copper block. The air trapped between the cylindrical copper block and the steel jacket serves effectively as a thermal insulator (since air has a thermal conductivity of 0.024 W/(m·K) compared to ~400 W/(m·K) for copper). This validates the assumption that heat loss in the radial direction is negligible compared to heat loss in the axial direction. Neglecting heat losses in the vertical direction, the heat flux in the vertical (axial) direction in the cylindrical copper block is assumed to be lost through the test surface in contact with the boiling liquid, and is formulated as:

$$q"_c \cdot A_c = q"_w \cdot A_w \; ; q"_w = \frac{q"_c A_c}{A_w} \quad (10)$$

In the above equation, $q_w"$ represents the wall heat flux through the test surface, A_c is the projected area of the cylindrical copper block, and A_w is the project area of the

surface in contact with the fluid. The Klein and McClintock method was used to calculate the measurement uncertainty for heat flux, as follows:

$$\frac{\omega_q}{q} = \sqrt{\left(\frac{\omega_{\Delta T}}{\Delta T}\right) + \left(\frac{\omega_{\Delta y}}{\Delta \mathrm{y}}\right) + \left(\frac{\omega_K}{K}\right)} \tag{11}$$

In this equation, ω represents the statistical uncertainty for the specific variable, while ΔT and Δy represent the temperature difference and spatial distance between the two thermocouples that are used for the temperature measurements and are aligned in the same vertical plane in the copper block. To measure the uncertainty value for the heat flux, uncertainty values for the temperature, spatial distance and thermal conductivity values need to be estimated. The thermal conductivity of copper was estimated to have an uncertainty value of ± 1.0% (from tables of material properties available in the literature), while the spatial distance between thermocouples was estimated to have an uncertainty of ± 3.0% (accuracy of machining). The measurement uncertainties for heat flux and wall superheat values were obtained by plotting the boiling curve with a confidence interval of 1σ, (where σ is the standard deviation value obtained from the statistical analysis of the measured temperature and heat flux data).

3.3.4 Experimental Procedure

The experimental procedure implemented in this study was based on previous studies ([25] [30] [52]). PF-5060 was selected as the test fluid due to its lower boiling point at 56°C (compared to water at 100 °C). Since stable film boiling conditions are usually achieved at high wall superheats (estimated to be ~50 °C for PF-5060 and hence

wall temperatures exceeding 100°C) the choice of PF-5060 was compatible with the experimental apparatus and was envisioned not to cause any damage to the experimental apparatus when dryout conditions were reached. This fluid (PF-5060) is a dielectric, which means it acts as an electric insulator and can rapidly quench electric discharges. This trait makes it ideal for electronic chip cooling operations.

After steady state conditions were achieved in the pool boiling experiment, temperature data was recorded using the digital data acquisition apparatus for each value of wall superheat. The power source is switched on to activate the coil heater and cartridge heaters after the leakage test and degassing step is completed. The chiller unit is used to maintain uniform subcooling of the test liquid (e.g., by maintaining the working liquid at 46°C for achieving 10°C subcooling and at 51°C for achieving 5°C subcooling). The bulk liquid temperature equilibrates to 56°C for saturated pool boiling conditions and the chiller unit is not required for these experiments. The condensed vapor lost from the boiling test liquid (PF-5060) is collected in a container placed in a bucket containing ice. The working liquid is also frequently replenished in the test chamber. The temperature data is recorded for each test surface and the experiments are performed to generate boiling curves ranging from the Critical Heat Flux (CHF) and Minimum Heat Flux (MHF) conditions. The first four data points were typically measured after reaching steady state conditions and before reaching CHF condition. Subsequently another four data points were measured after achieving steady state conditions and before reaching MHF conditions (i.e., the Leidenfrost point).

When steady state conditions were met for each data point in the experiment, the digital data acquisition apparatus (DAQ) was used to record the temperature data from the thermocouples and TFT array. The temperature data obtained from the wire bead thermocouples inserted into the cylindrical copper block (calorimeter apparatus) was used for calculation of the wall heat flux values. Temperature measured by the TFT arrays was used to calculate the wall superheat values. Boiling curves were plotted based on the heat flux values and wall superheat values (as well as from the appropriate estimates for measurement uncertainty) obtained from each set of experiments for each liquid subcooling. Typically, steady state conditions were achieved in ~2 hours for each data point in the boiling curve during nucleate boiling and in ~3 hours for each data point in the boiling curve during film boiling. Steady state condition was defined as the situation where the variation in the temperature data recorded by the wore-bead thermocouples (as displayed in the LabVIEW GUI) did not change by more than 1°C during a 5-10 minute period. After achieving steady state conditions, the temperature measurements were recorded by the DAQ for each component: such as, the TFT array located on the heater test surface, the wire bead thermocouples inserted in the copper block and in the bulk fluid. In tandem, videos of the bubble dynamics was recorded using two sets of camera (a high speed and a low speed camera). The frames of images obtained from the recorded videos were used subsequently for flow visualization analysis.

After recording the videos and temperature data for a given steady state condition, the input power to the cartridge heaters was increased by raising the voltage in small increments (e.g., about 5 V increments). After incrementing the input power there was a

waiting time of approximately 2 ~ 3 hours before steady state conditions were achieved once again. The required subcooling conditions were also maintained and monitored by adjusting the liquid temperature flowing from the chiller into the cooling coil.

After achieving CHF conditions, caution must be exercised for the system to traverse the transition boiling regime before achieving steady film boiling conditions (in order to ensure that the system does not become unstable or undesirable conditions leading to burnout does not occur). The power input for the cartridge heater is increased incrementally to achieve film boiling conditions, and then the power input is progressively decreased to avoid the test surface from reaching the maximum rated temperature of the cartridge heaters (which is rated at 200°C). This experimental protocol is termed conventionally as a "power controlled" experiment. This implies that the pool boiling experiments are performed by controlling the heat flux values and letting the system response stabilize to different values of wall superheat. In this approach the temperature of the test surface can increase dramatically after CHF condition and before steady state film boiling conditions are achieved. Hence, these types of experiments require careful monitoring of the temperature recorded in real time to prevent system instabilities or catastrophic failures. Additionally, the continuous and stable vapor blanket that forms on the test surface in the film boiling regime - essentially acts as an effective insulating vapor film. When this condition is reached, the power has to be reduced incrementally to avoid burnout, ensuring the pool boiling apparatus does not undergo any damage. As always, the chiller unit flow rate and temperature are also modulated so that the bulk fluid would be maintained at the required temperature for ensuring subcooled or saturated conditions.

Once steady film boiling conditions are achieved the Leidenfrost point is reached by incrementally decreasing the power input to the pool boiling system for each steady state condition. The system is cooled down once the Leidenfrost point has been reached, and the temperature data has been documented. The recorded values of temperature is compiled and post processed in order to plot the boiling curve for each set of experiments. The boiling curves generated from different sets of experiments are then compared to enumerate the corresponding dominance of various transport mechanisms. If needed, repeatability of the experiments can be verified by repeating the whole procedure immediately after completing each set of experiments.

4 EXPERIMENTAL RESULTS AND DISCUSSION

The author acknowledges the help of Dr. Hongjoo Yang, Mr. Binjian Ma, and Mr. Yi Wang for performing the pool boiling experiments and obtaining the raw data which were then analyzed and reported in this study.

4.1 Data Reduction and Uncertainty

4.1.1 Boiling Curves

The boiling curves were obtained by plotting the wall heat flux as a function of wall superheat. The wall superheat was obtained from the temperature values recorded by the TFT arrays (for silicon wafer) or by extrapolating the temperature gradients obtained from the thermocouple data (for copper and AAO). As described in Chapter 3, the heat flux values were obtained by using 1-D Fourier's Law of heat conduction.

The Kline-McClintock method was used for estimating the measurement uncertainty values in the heat flux for the boiling curves. The equation specifically used in this case has slight variation from the equation mentioned in Chapter 3. The relative uncertainty was calculated for the heat flux calculations using the following:

$$\frac{\omega_q}{q} = \sqrt{\left(\frac{\omega_k}{k}\right)^2 + \left(\frac{\omega_{T1}}{T_2 - T_1}\right)^2 + \left(\frac{\omega_{T2}}{T_2 - T_1}\right)^2 + \left(\frac{\omega_{\Delta y}}{\Delta \mathrm{y}}\right)^2} \tag{13}$$

Similar to Chapter 3, the uncertainty for each value is denoted with a subscript. Thermal conductivity for copper was found in literature to be 401 W/m-K, with a measurement uncertainty assumed to be ± 1%, while Δy represents the distance between the two

thermocouples, and its representative uncertainty is estimated to be around ± 3%. The uncertainty of the temperature measurements is found by solving the root sum square (RSS) of the precision and bias uncertainties. Based on the DAQ resolution, the bias uncertainty is estimated to be ± 0.05°C. A 95% confidence interval was assumed for the precision uncertainty of the measurements.

The average of the six heat flux values from the thermocouples is the reported value for each data point. The uncertainty of this average heat flux value was calculated by finding the root mean square (RMS) of the six pairs of the thermocouples. The uncertainty of the average heat flux was estimated to range from 0.68 – 0.80 W/cm^2. Additional information regarding the measurement uncertainty estimates are provided in Appendix A.

4.1.2 Departure Diameter

To calculate bubble departure diameter, a calibration factor was used to translate the measurement of bubble size in pixels (in the digitized images) to the physical length scales. The calibration factor was calculated by dividing the width of the heater in millimeters (i.e., the size of the opening in the steel clamp) by the width of the heater measured in pixels (as obtained from the digitized images). The units for the calibration factor were obtained as mm/pixels. The calibration factor ranged from 0.032 – 0.047 mm/pixels, depending on the frame size. Once this value was calculated from the measurements, the departure diameter was calculated by using the following equation:

$$d_D = \frac{y_1 - y_2}{CF} \tag{14}$$

In this case, y_1 and y_2 are the measured distance (horizontal coordinates) from side to side of each bubble in pixels and CF is the calibration factor as mentioned before. Since the bubbles are spherical, the diameter measurements involve the estimation of the spans (from side to side and top to bottom of the bubble). Then these measured values are averaged to produce the mean value for the diameter of the bubble. These measurement are then compiled and used for comparison (e.g., for differnet experimental conditions).

The measurement uncertainty for the measured values of departure diameter was calculated using the Kline-McClintock method. The blurry edges of the bubbles in the captured frames were the dominant contributors to the net measurement uncertainty. The uncertainty value ω_y of the measurements y_1 and y_2 were estimated as ± 5 pixels. The measurement uncertainty for the departure diameter was estimated using the following equation:

$$\omega_{d_D} = \frac{\sqrt{2}\omega_y}{CF} \tag{15}$$

The measurement uncertainties for departure diameter are tabulated in Appendix A.

To obtain effective comparison between different experimental conditions it was necessary to estimate the measurement uncertainties for each experiment. The RSS of the bias and precision uncertainties were used for obtaining the average values of departure diameter. The bias error was assumed to be the same as the measurement uncertainty of the samples in the group. The precision error was based on the 95% confidence interval

for each group of data. This can be calculated by averaging the standard deviation of the group and the number of samples in the group. Table 2 lists these values.

For image processing, the measurement uncertainty was calculated by using two separate measurements of the diameter and height of the bubbles. The measurement uncertainty for any specific bubble was the difference of these two separate measurements (and then converted to a percentage value). The percentage value could be obtained from measured values of bubble height and diameter (either in pixels or in millimeters).

4.1.3 Departure Frequency

Bubble departure frequency was calculated in Hz, using the following equation:

$$f = \frac{FR}{t_1 - t_2} \tag{16}$$

where, *FR* represents the frame rate of the image acquisitions (either 1000 or 500 frames per second), while t_1 and t_2 represents the time elapsed in between successive frames for each bubble departure. This was documented through reporting the frame number and the number of frames that passed in between each nucleation event. The numerator was entirely dependent on the frames per second for the video footage. For 1000 fps, each frame is 1 ms apart while for 500 fps each frame is 2 ms apart.

An overall uncertainty value was obtained for groups of measurements after calculating the ”Root Mean Square (RMS)” errors, which is the square root of the standard deviation for each uncertainty measurement divided by the average of the uncertainties. The equations below shows the procedure for estimating the measurement uncertainty for bubble departure frequency:

$$\omega_{f1} = \frac{\omega_t}{(t_2 - t_1)} \tag{17}$$

$$\omega_{f2} = \frac{\sigma_{\omega_f}}{\overline{x_{\omega_f}}} \tag{18}$$

$$\overline{\omega_f} = \sqrt{(\omega_{f_1}^2 + \omega_{f_2}^2)} \tag{19}$$

Measurement uncertainties ranged from ± 20 Hz (at 50 Hz) to ± 0.1 Hz (at 6.9 Hz). The frequency measurements were made using the high speed videos (that were acquired at either 500 fps or 1000 fps). The choice of each video for the calculations was mediated by the clarity of view for individually selected bubble nucleation sites. It was observed that often the videos acquired at higher frame rates (i.e., 1000 fps) provided more crisp images and therefore suffered from lower values of measurement uncertainties.

Measurement uncertainties for all of the frequency measurements are tabulated in the Appendix.

4.2 Boiling Curves

Comparisons of boiling curves between various test surfaces was performed in this study. A boiling curve shows the dependence of heat flux (q'') on wall superheat ($T_w - T_{sat}$). These comparisons also help to ensure that the experiments are repeatable. Figure 4-1 summarizes the boiling curves for all of the experiments performed in this study. Experimental data for both nucleate and film boiling regimes are shown in this figure. As

expected, the wall heat flux values increase with increase in subcooling for the same values of wall superheat. As expected lowest levels of CHF are achieved for bare silicon wafers and AAO substrates demonstrate higher levels of pool boiling heat flux values than silicon. Also, as expected, copper heaters have significantly higher levels of CHF. However, AAO substrates demonstrate highest levels of heat flux values for lower wall superheats.

Comparisons with prior reports in the literature show that for boiling curves obtained for Copper heaters CHF occurs at lower wall superheats (than that of the measurements obtained in this study, where CHF was observed to occur at wall superheat values of ~40°C). This discrepancy has been investigated and potential sources of error have been identified. The possible sources of error are discussed subsequently in this section.

Figures 4-2 and 4-3 show the experimental data only for the nucleate boiling regime (without and with error bars, respectively). The plots for the boiling curves show that higher values of heat fluxes are achieved with AAO substrates for lower values of wall superheat. However, at higher values of wall superheat significantly higher values of heat fluxes are achieved with a copper heater.

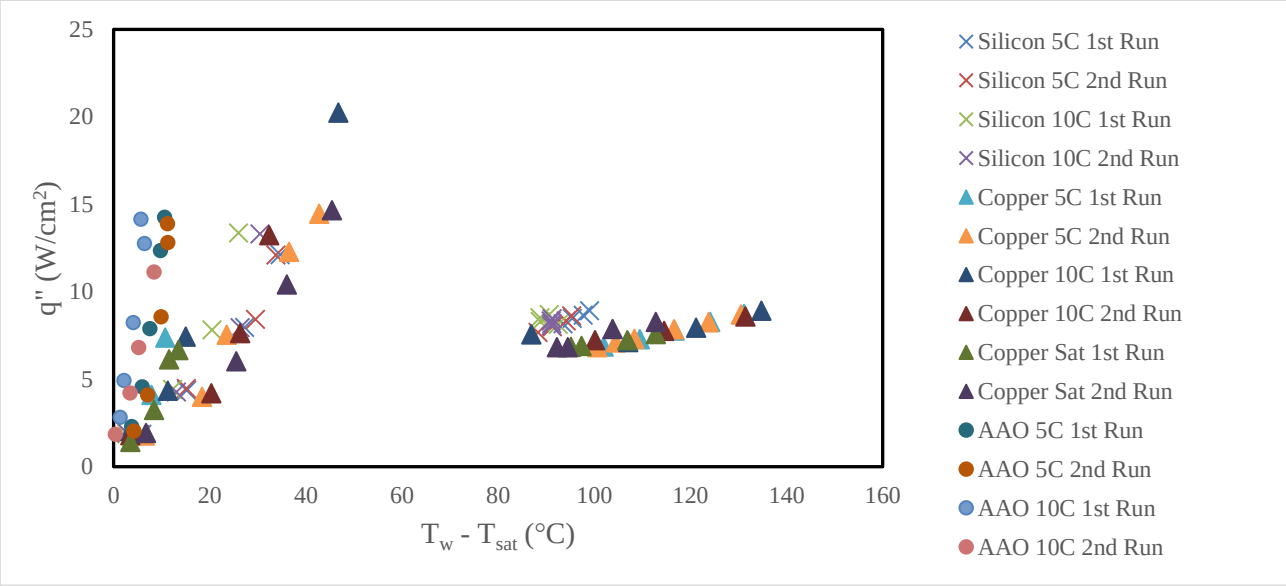

Figure 4-1 Plots for boiling curves for both nucleate and film boiling regimes.

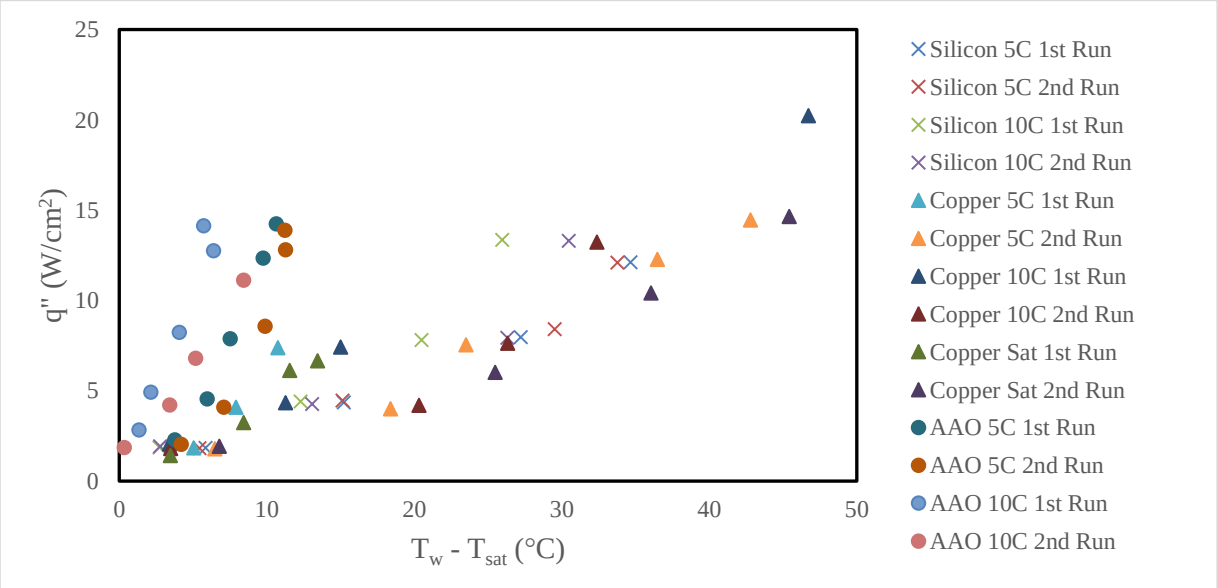

Figure 4-2 Plots for boiling curves for nucleate boiling regime.

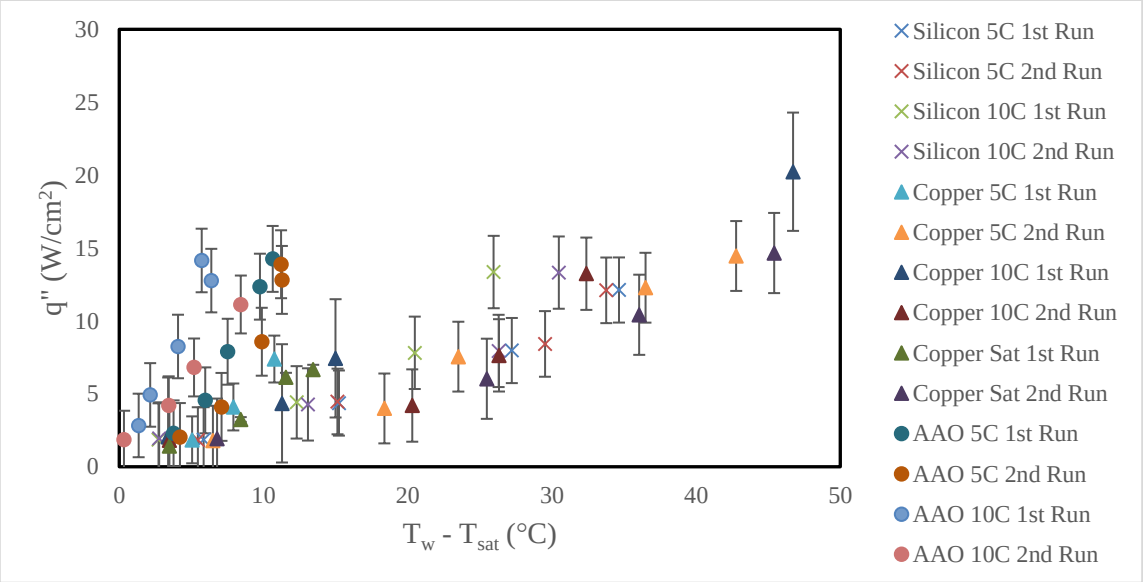

Figure 4-3 Plots for the boiling curves for the nucleate boiling regime with error bars.

For the AAO surfaces, pool boiling experiments were performed only for the nucleate boiling regime (since the temperature in the copper block/calorimeter apparatus exceeded the maximum temperature rating when the experiments progressed toward CHF condition into transition and film boiling regimes). Also the flow visualization experiments were difficult to perform for AAO substrates due to enhanced turbulence in the liquid pool that made it challenging to acquire images of vapor bubbles with sufficient clarity (compared to the experiments performed using copper heaters and silicon wafers).

The experimental results for silicon wafers are plotted in the boiling curves shown in Figure 4-4 and Figure 4-5. The experimental data is found to be repeatable within the bounds of the measurement uncertainty. Also, these results are observed to be consistent with previous report in the literature ([25], [20]).

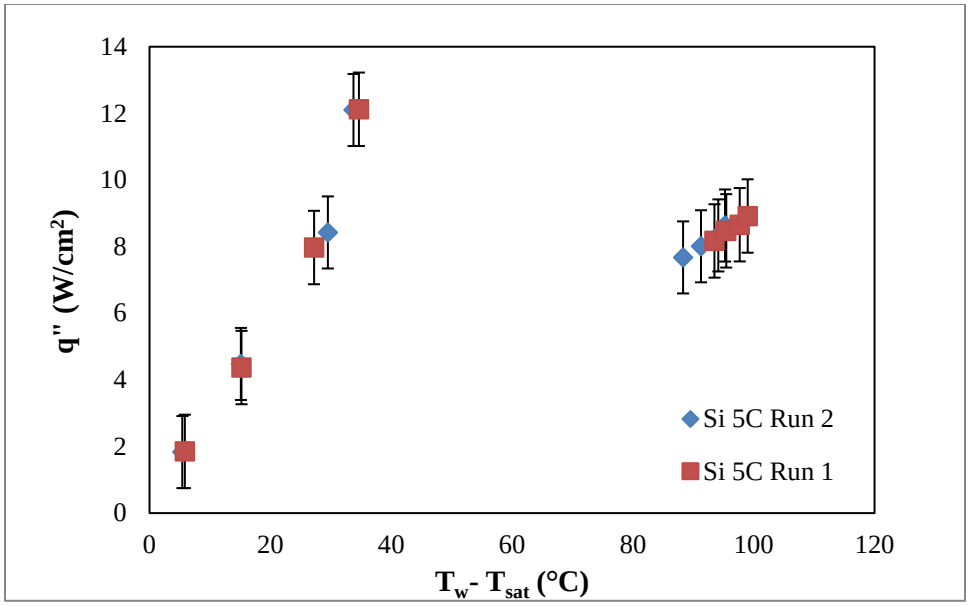

Figure 4-4 Boiling curve for Silicon at subcooling of 5°C.

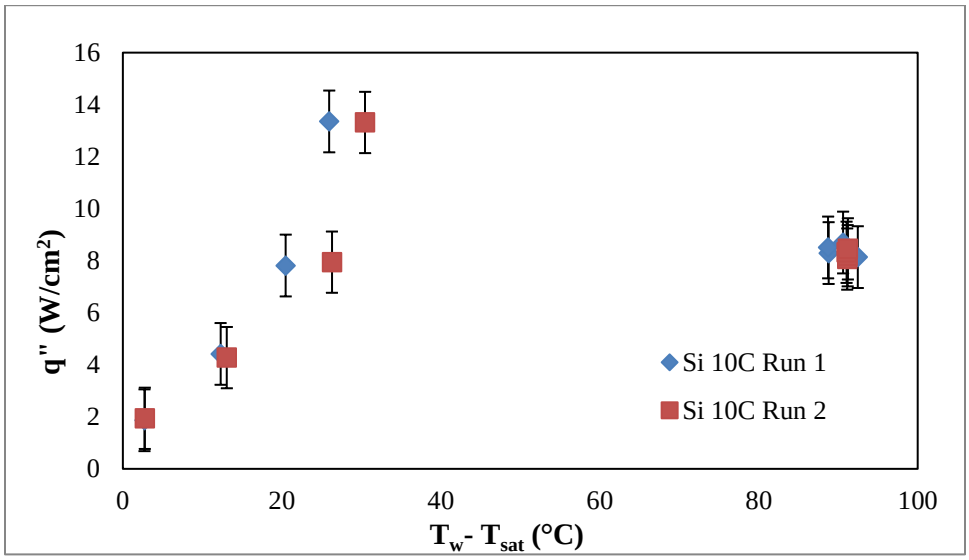

Figure 4-5 Boiling curve for Silicon at subcooling of 10 °C.

The CHF for Silicon for a subcooling of 5°C was 12.1 W/cm^2 ± 3%, while for a subcooling of 10°C the CHF is observed to be 13.4 W/cm^2 ± 2.5%. The CHF for Copper

has more variation compared to Silicon. This variation may allude to the fact that the results for Copper had less repeatability. The various CHF values for each run at 5°C subcooling, 10°C subcooling and saturation conditions is tabulated in the Appendix. The boiling curves for Copper in different subcooling and saturation conditions are plotted in Figures 4-6, 4-7 and 4-8. As mentioned before, true CHF conditions could not be achieved for experiments performed using the AAO substrates. The boiling curves for the AAO substrates in the nucleate and pool boiling regimes are plotted in Figure 4-9 and Figure 4-10.

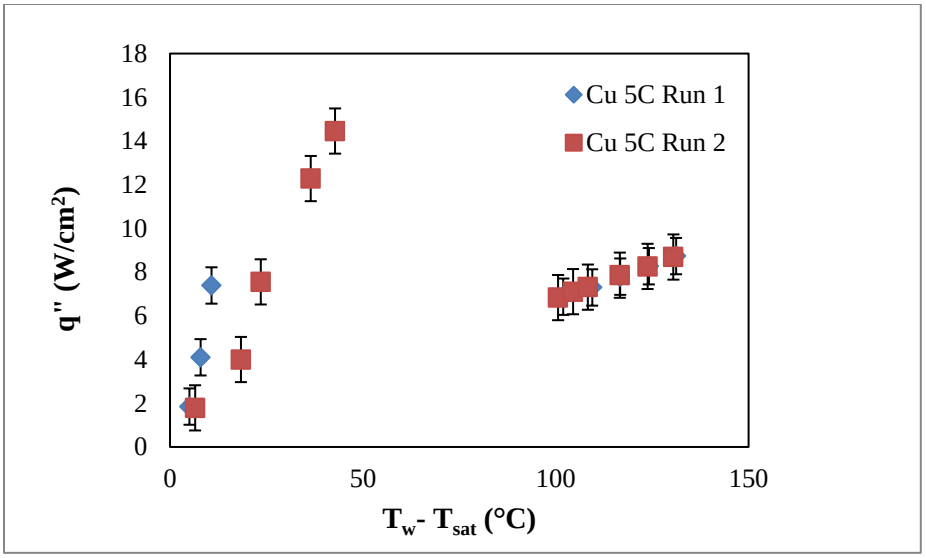

Figure 4-6 Boiling curve for Copper at subcooling of 5°C.

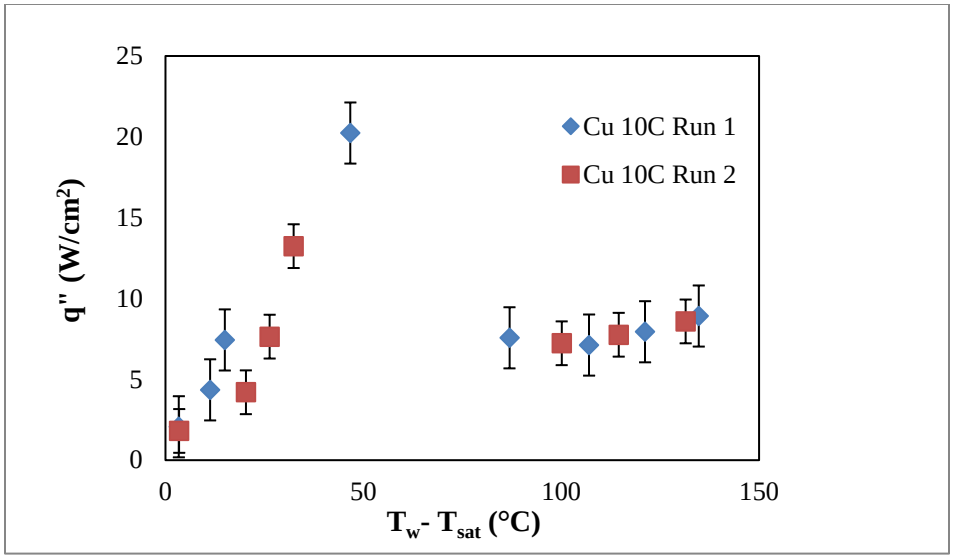

Figure 4-7 Boiling curve for Copper at subcooling of 10°C.

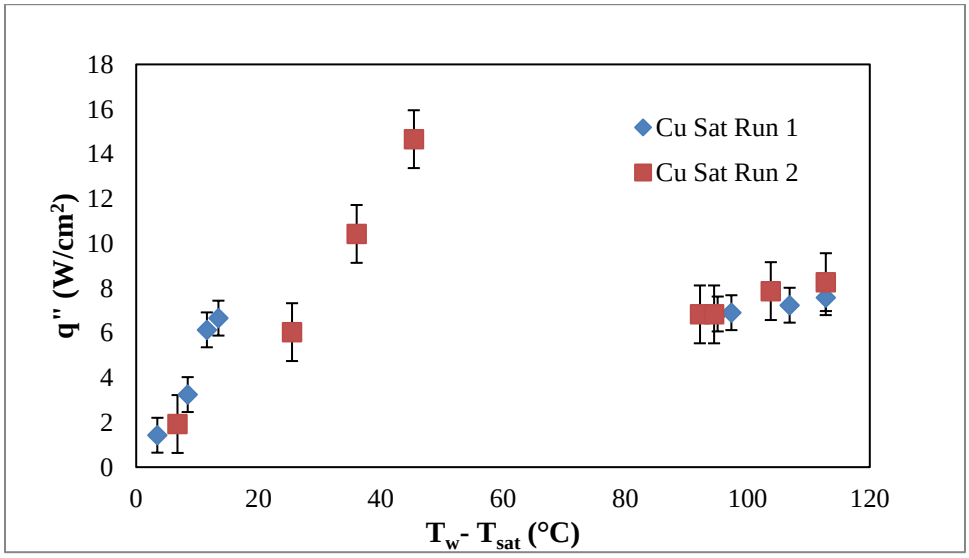

Figure 4-8 Boiling curves for Copper for saturated pool boiling conditions.

Copper reached the highest CHF at 10°C (20.5 W/cm^2), although it had an extremely high superheat (50°C) to reach it. The CHF for Copper at a subcooling of 5 °C was recorded to be 14.5 W/cm^2 ± 4%. The CHF for Copper at subcooling of 10 °C was observed to be

13.23 W/cm^2 ± 3%. The CHF for copper for the saturated pool boiling experiments was recorded to range from 6.6 to 14.7 W/cm^2 ± 5%. The CHF value at subcooling 5 °C is expected to be marginally higher than that of the saturated case. However, these experimental results show that the CHF value at subcooling of 5 °C is marginally lower than that of the saturated case. Therefore, these data points are within the limits of measurement uncertainty and a definitive conclusion cannot be drawn about which of the CHF values are larger.

Moreover, small discrepancies are observed for the results for the Copper boiling curve. Sources of error that have been identified as potential causes for the observed discrepancy include calibration errors for the thermocouples or human error involving the assembly of the experimental setup (such as the Copper surface not being polished entirely before the start of the experiments).

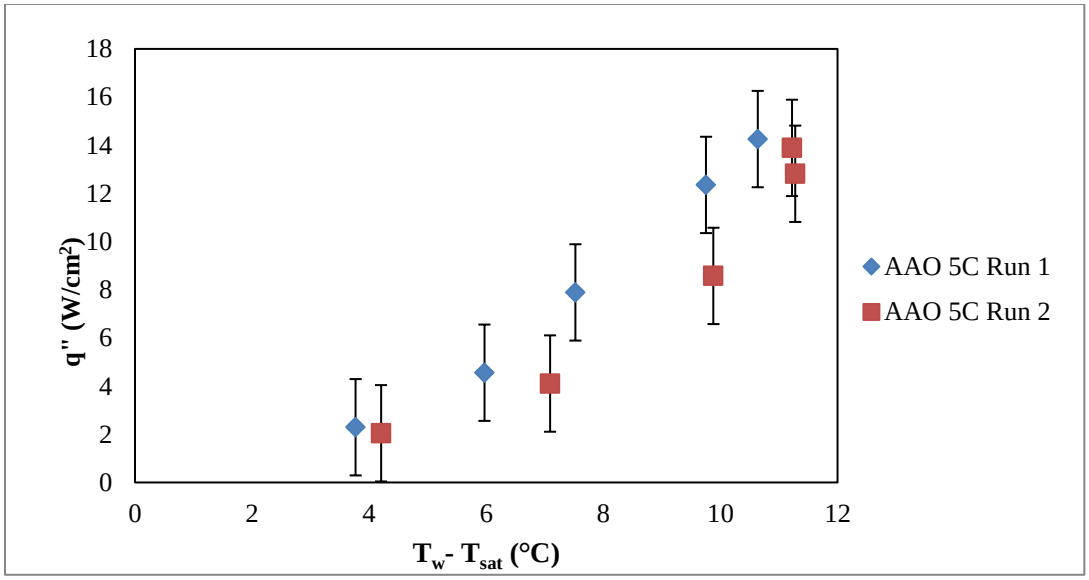

Figure 4-9 Boiling curve for AAO at subcooling of 5 °C.

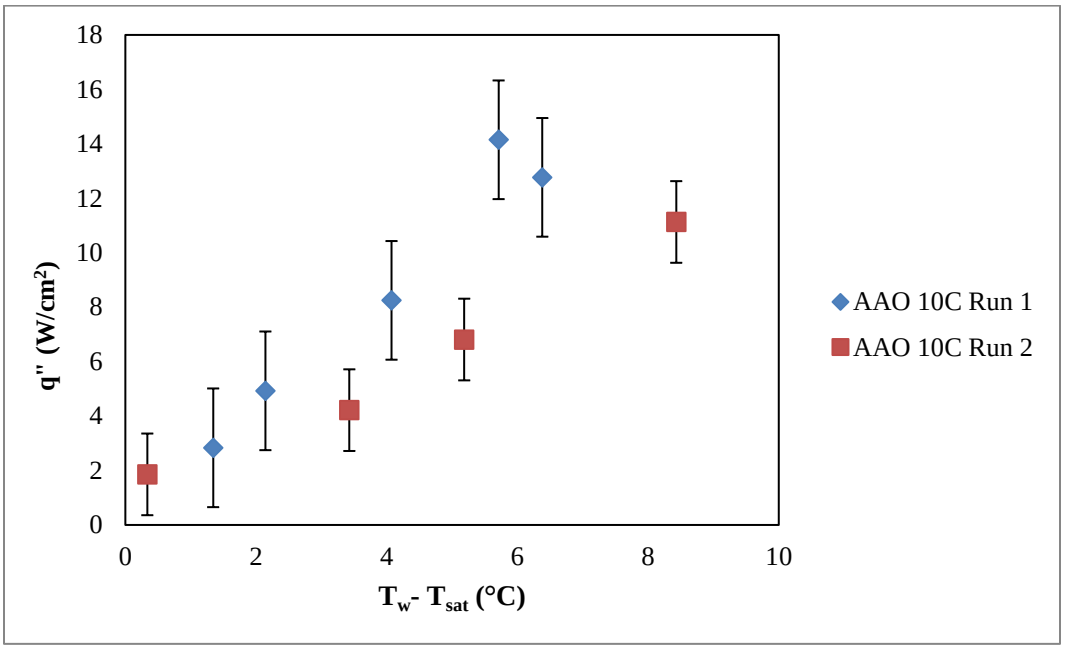

Figure 4-10 Boiling curve for AAO at subcooling of 10 °C.

While the boiling curve for AAO does not show distinctively higher heat flux values approaching CHF, the heat flux values at CHF for AAO in 5°C and 10°C are achieved at lower values of wall superheat respectively, showing a definitive shift in the boiling curve compared to that of Silicon and bare Copper. Copper and Silicon both have superheats exceeding 20°C at CHF. In contrast at subcooling of 5°C for AAO CHF conditions were approached at a wall superheat of ~ 11°C. Hence, for lower values of wall superheat, enhancement in heat flux was observed to occur for AAO substrate (nanostructured surface) compared to heaters with plain surfaces (copper and silicon).

The boiling curves for AAO show that boiling incipience occurred at lower values of superheat (than the plain heaters). CHF enhancement for AAO substrates was marginal

in these experiments (compared to that of bare silicon wafers). Further investigations are needed to determine whether AAO can truly affect the CHF compared to plain surfaces.

4.3 Analysis of Images

With the completion of each experiment, high speed videos were recorded for the test surfaces for subsequent analysis of the bubble dynamics. These high speed videos were split into frames with a MATLAB script, with appropriate file names for each frame to indicate elapsed time of the video. Bubble dimensions were determined through various image processing programs, such as a custom made in-house code developed by a former student (VisualBasic® application developed by Stephen Gauntt, former M.S. student at the Multi-Phase Flow and Heat Transfer Laboratory at Texas A&M University) and using Microsoft Paint. Height and diameter (in pixels) of nucleating bubbles were measured from the heater surface using these programs. The measurements for each selected bubble (in pixels) were also converted to millimeters, by multiplying the measurements with a calibration factor (as mentioned in the prior sections). This calibration factor was found by measuring the width of the heater in pixels from these images and then dividing it by the width of heater (measured using a measuring scale in millimeters). The bubble dimensions were then input into various spreadsheets for each test. The bubble departure frequency was measured by finding the number of frames that elapsed between two consecutive bubble departure events at a chosen location. The difference of the time elapsed between these frames was the elapsed time – which is the time period for bubble

departure. The inverse of this time period value is considered to be the bubble departure frequency at that wall superheat.

Figure 4-11 shows a sample image of a bubble departing from the heater surface (AAO Substrate). Uncertainty was generally higher for images analyzed for the AAO surface due to graininess of the video and the smaller size of the bubbles. One way to ensure the bubble measurement was more accurate was to look for a reflection of the bubble formation on the surface. The bubble departure diameters, heights and departure frequencies were all within a specific range in a given video.

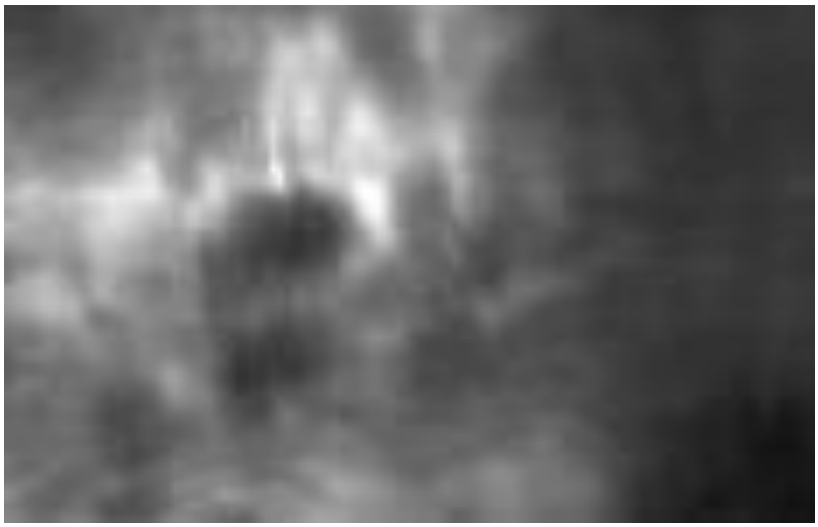

Figure 4-11 Image acquired from the flow visualization experiments at subcooling of 5 °C on AAO surface at wall superheat of 2.14 °C. The bubble reflection can be seen on the surface. This bubble is approximately 0.11 mm in diameter.

4.3.1 Departure Diameter

Bubble departure diameter measurements were recorded for each test surface in every experiment. To account for the bubble's sphericity, the bubble's height and diameter were measured and a mean value was calculated from the average of the measurements to

account for the actual diameter. The neck of the bubble during departure from the surface was included in the measurements. It was observed that the region of the bubble neck accounted for approximately 30% of the total height of the bubble.

Figure 4-12 shows a distribution of the bubble departure diameters for the different test surfaces in both film boiling and nucleate boiling at different values of subcooling. Figure 4-13 shows a distribution of the bubble departure diameters for the different test surfaces in nucleate boiling at different values of subcooling. The results show that the bubbles generated on the nanostructured surface (AAO substrates) are consistently smaller than that of the plain surface (approximately 50% smaller).

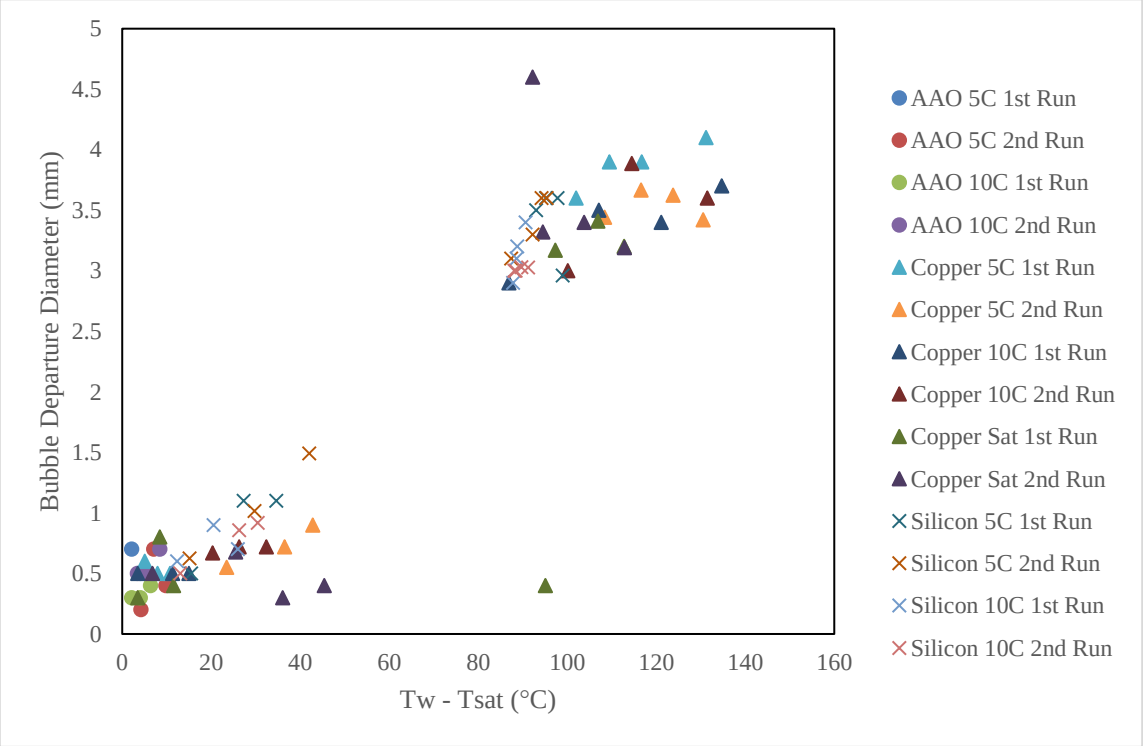

Figure 4-12 Departure diameters recorded at various values of wall superheat for the heater substrates compiled for all the experimental measurements in this study.

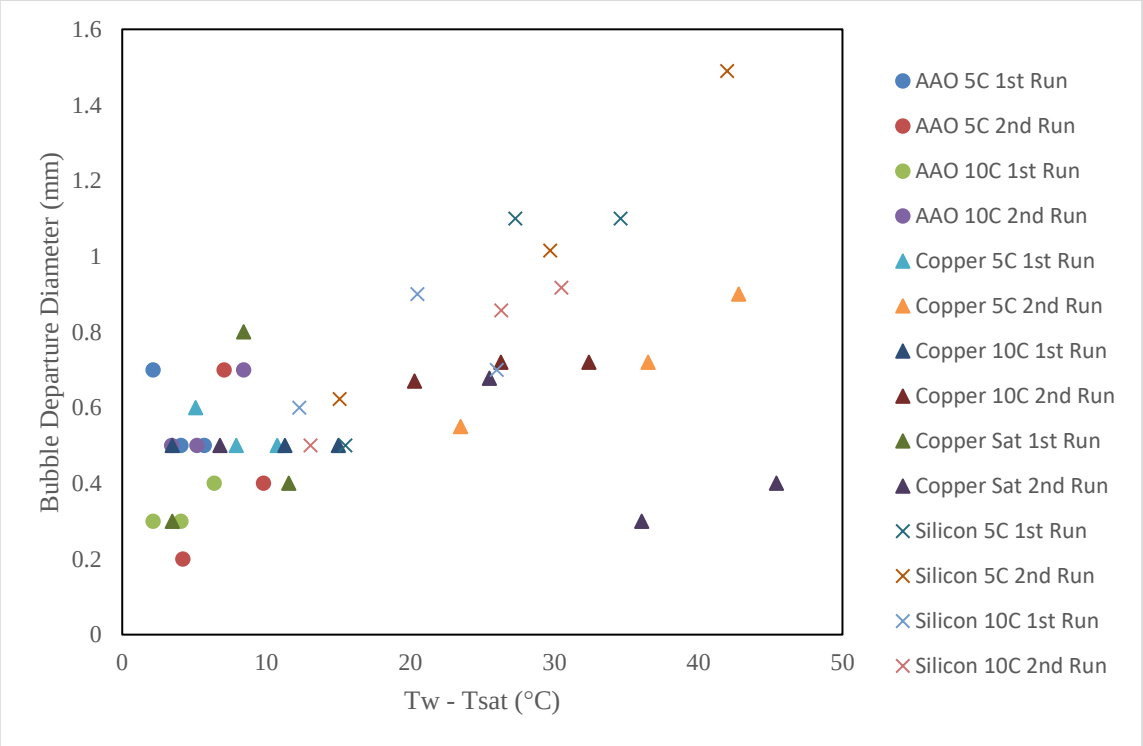

Figure 4-13 Departure diameters recorded at various values of wall superheat in the nucleate boiling regime for the heater substrates compiled for all the experimental measurements in this study.

Both Silicon and bare Copper surfaces had much larger bubble departure diameters ranging from 2.9 to 4.1 mm in film boiling. Bubbles departing from the AAO surface had less variation, ranging from 0.2 to 0.7 mm in nucleate boiling. Holistically however, the bubbles grew in size as the superheat increased. Bubbles from the AAO surface were generally 12.5-45% smaller at lower superheats compared to their Silicon or Copper counterparts, (0.47 mm to 0.54 mm or 0.86 mm respectively). The departure diameter was also smaller at 10°C subcooling versus 5°C subcooling for all the surfaces. Images obtained for experiments involving saturated pool boiling as well as subcooling of 5 °C and 10 °C had similar values of bubble departure diameters for the bare Copper surface.

Table 2 displays the average departure diameters for each surface and their absolute measurement uncertainty.

Table 2 Average departure diameters and absolute uncertainty for each surface (dimensions in mm)

Average d_D for Bare Silicon							
Regime	5 °C Subcooling			10 °C Subcooling			
	Run 1	Run 2	Both	Run 1	Run 2	Both	All
Nucleate	0.9	1.043	0.971	0.733	0.758	0.746	0.859
ω_{nuc}	0.167	0.147	0.157	0.133	0.103	0.118	0.138
Film	3.415	3.4	3.408	3.15	3.015	3.082	3.245
ω_{film}	0.29	0.275	0.283	0.275	0.21	0.243	0.263

Average d_D for AAO							
Regime	5 °C Subcooling			10 °C Subcooling			All
	Run 1	Run 2	Both	Run 1	Run 2	Both	
Nucleate	0.567	0.433	0.5	0.333	0.567	0.45	0.475
ω_{nuc}	0.1	0.0467	0.073	0.05	0.06	0.055	0.064

Average d_D for Bare Copper										
Regime	5 °C subcooling			10 °C subcooling			Saturated			All
	Run 1	Run 2	Both	Run 1	Run 2	Both	Run 1	Run 2	Both	
Nucleate	0.533	0.723	0.628	0.5	0.703	0.602	0.5	0.47	0.485	0.543
ω_{nuc}	0.1	0.083	0.092	0.1	0.077	0.0883	0.098	0.095	0.096	0.092
Film	3.875	3.539	3.707	3.375	3.5	3.435	3.260	3.628	3.444	3.439
ω_{film}	0.225	0.313	0.269	0.2	0.263	0.231	0.15	0.23	0.19	0.210

Bubble dynamics on AAO substrates is expected to result in smaeer values of bubble diameter at departure (than that of Copper and Silicon heater surfaces). These results are consistent with prior literature reports (where nanostructured surfaces typically

reduced the bubble departure diameter and increased bubble departure frequency, due to lower effective contact angles for nanostructures surfaces -arising from longer contact line lengths).

A large number of correlations exist in the literature for predicting bubble departure diameter and bubble departure frequency values during pool boiling. A selected list of these correlations were culled from the literature and were included in this study for comparison with the experimental data obtained in this study. These correlations are typically expressed as a function of Bond number, defined as:

$$Bo = \frac{g d_D^2 (\rho_l - \rho_v)}{\sigma} \tag{20}$$

These correlations are listed below:

1. Ruckenstein [37]:

$$Bo^{\frac{1}{2}} = \left[3 * \pi^2 * \frac{\rho_l \alpha_l^2 g^{\frac{1}{2}} (\rho_l - \rho_v)^{\frac{1}{2}}}{\sigma^{\frac{3}{2}}} \right]^{\frac{1}{3}} Ja^{\frac{4}{3}} \tag{21}$$

where

$$Ja = \frac{\rho_l c_{pl} [T_w - T_{sat}]}{\rho_v h_{fg}} \tag{22}$$

2. Jensen & Memmel [2]

$$Bo^{\frac{1}{2}} = 0.19(1.8 + 10^5 K_1)^{\frac{2}{3}} \tag{23}$$

where

$$K_1 = \left(\frac{Ja}{\mathrm{Pr}_l}\right)^2 \left\{ \left[\frac{g \rho_l (\rho_l - \rho_v)}{\mu^2} \right] \left[\frac{\sigma}{g(\rho_l - \rho_v)} \right]^{\frac{3}{2}} \right\}^{-1} \tag{24}$$

3. Cole [34]

$$Bo^{\frac{1}{2}} = 0.04Ja \tag{25}$$

where Ja is defined from Eq. (14).

4. Kutateladze & Gogonin [3]

$$Bo^{\frac{1}{2}} = 0.25(1 + 10^5 K_1)^{\frac{1}{2}} \qquad \text{for } K_1 < 0.06 \tag{26}$$

where K_1 is the same one defined from Eq. (23).

5. Zuber [38]

$$Bo^{\frac{1}{2}} = \left[\frac{\sigma}{g(\rho_l - \rho_v)}\right]^{-\frac{1}{6}} \left[\frac{6k_l(T_w - T_{sat})}{q"}\right]^{\frac{1}{3}} \tag{27}$$

6. Cole & Schulman [35]

$$Bo^{\frac{1}{2}} = \frac{1000}{P} \tag{28}$$

and the units for pressure (P) is in mm Hg.

7. Cole & Rohsenow [36]

$$Bo^{\frac{1}{2}} = C(Ja^*)^{\frac{5}{4}} \qquad \text{for } P_{system}/P_{critical} < 0.2 \tag{29}$$

where

$$Ja^* = \frac{T_{sat} c_p \rho_l}{\rho_v h_{fg}} \tag{30}$$

and $C = 4.65 \times 10^{-4}$. This value is for fluids other than water. The unit for T_{sat} is in Kelvin for Eq. (30).

8. Fritz [56]

$$Bo^{\frac{1}{2}} = 0.0208\theta \tag{31}$$

where, θ is the static contact angle expressed in degrees.

9. Borishanky & Fokin [57]

$$\frac{d_D}{d_F} = -\frac{C}{d_F} + \sqrt{\frac{C^2}{d_F^2} + 1} \tag{32}$$

where

$$C = \left(\frac{6}{g}\right)\left(\frac{\rho_l}{\rho_l - \rho_v}\right)\left(\frac{\rho_v}{\rho_l}\right)^{0.5}\left(\frac{q^{"}}{h_{fg}\rho_v}\right) \tag{33}$$

and d_F is the diameter from Fritz's correlation Eq. (31).

Figures 4-14, 4-15, and 4-16 shows a comparison of the experimental data for bubble departure diameters obtained for Copper heaters compared to the predictions from the correlations listed above. Figures 4-17 and 4-18 shows a comparison of the experimental data for bubble departure diameters obtained for Silicon wafers compared to the predictions from the correlations listed above. Each figure shows results for both Run 1 and Run 2 for their respective surfaces. For copper and silicon, a general trend of increasing departure diameter was observed with increasing wall superheat. However, for AAO, there was anomalous variation and less consistency in departure diameter for increasing wall superheat.

The variation of departure diameter for the 3 surfaces did not show any definitive trends when considered holistically. The experimental data for copper at 5°C subcooling showed significant variability, and a general trend showing decrease of departure diameter with increasing superheat. This matches the trends predicted by the correlations of Cole

and Schulman as well as that of Cole and Rohsenhow. For bare Copper at 10°C subcooling, one data point is in agreement with the correlation of Kutateladze and Gogonin's, but the remainder of the data points deviates to a lower slope, with significantly lower values of departure diameter. Experimental measurements for bubble departure diameter for the Copper heater in saturated pool boiling experiments had the most variability. In general, the measured values of bubble departure diameter for copper matched the trends predicted by Zuber's correlation. The data at lower wall superheat follows almost a parabolic trend.

After plotting the experimental data, it is observed that for two of the points for Silicon at 5°C subcooling were aligned within the range of predictions obtained from the correlation of Kutateladze and Gogonin., Hence the predictions from the correlation were consistent with approximately half of the experimental data. The bubble departure diameter measurements for Silicon at 10°C subcooling showed much wider variability, with some of the data sets showing conformity with predictions from Zuber's correlation and some of the data sets showing conformity to that of Cole and Rohsenhow.

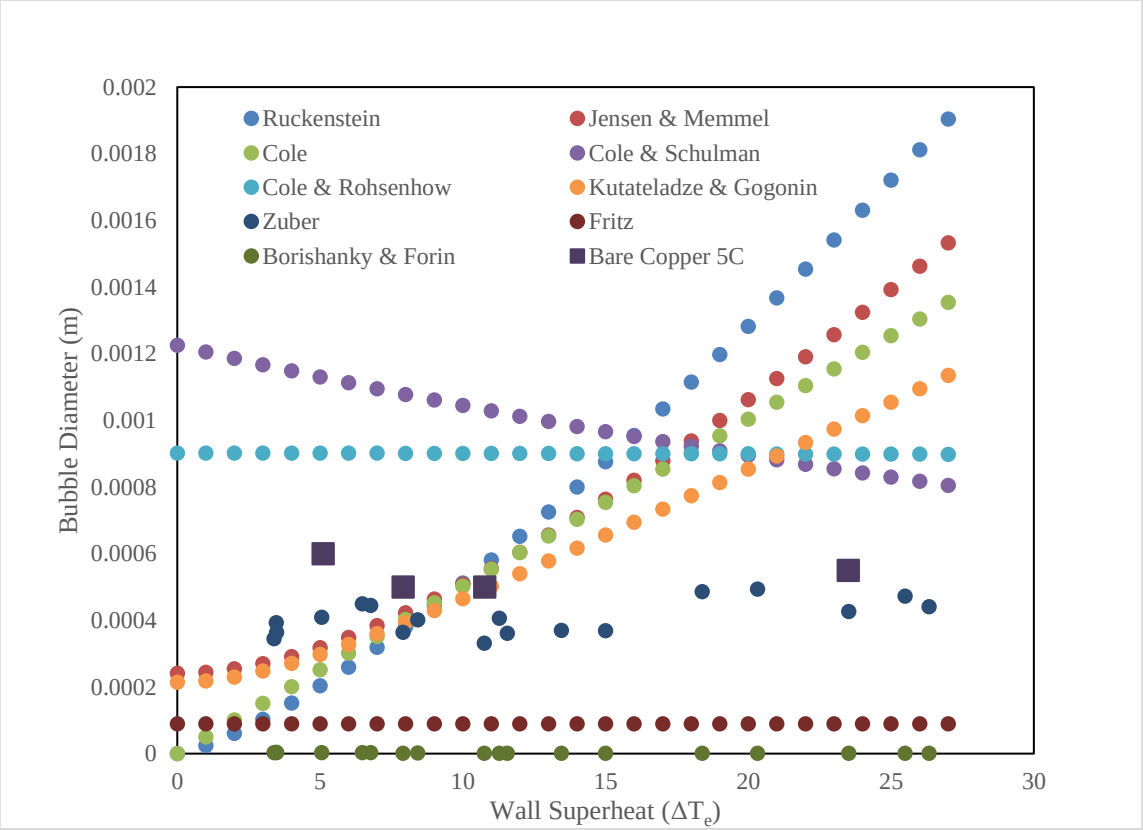

Figure 4-14 Comparison of the measured departure diameter for Copper heater at 5 °C subcooling and the predictions from the selected correlations as a function of the wall superheat.

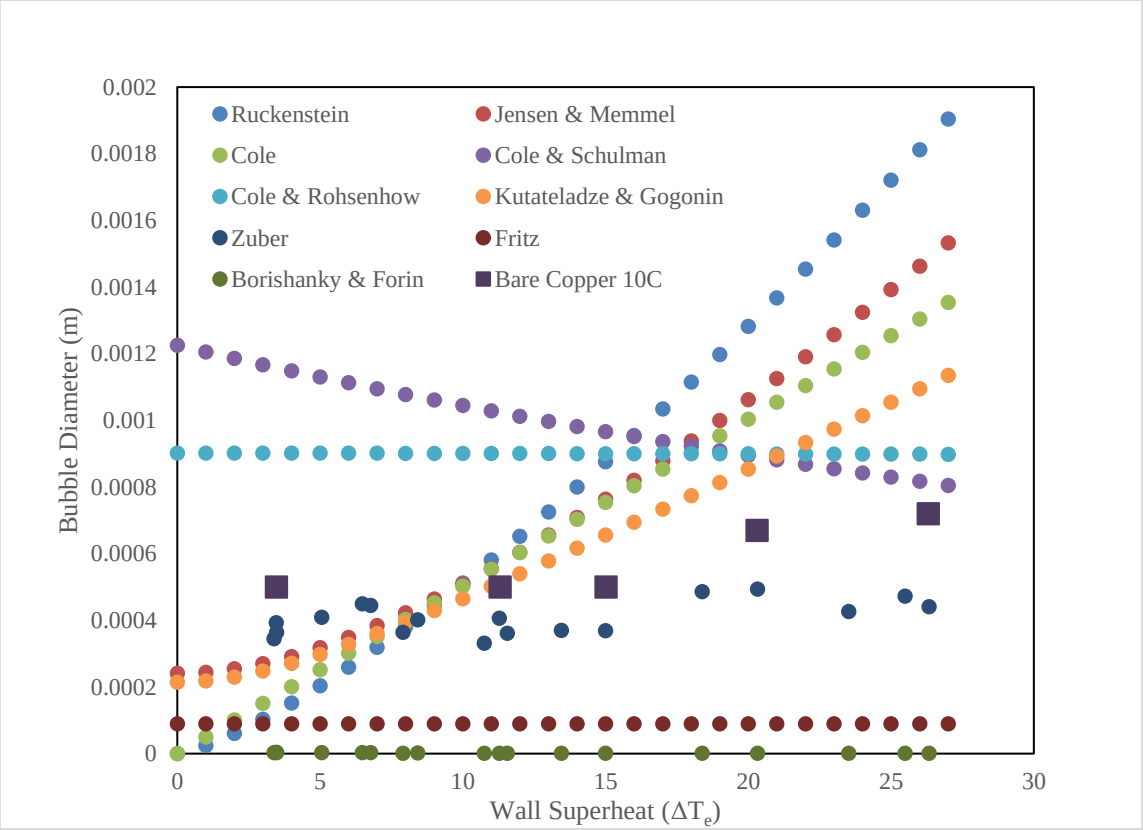

Figure 4-15 Comparison of the measured departure diameter for Copper heater at 10 °C subcooling and the predictions from the selected correlations as a function of the wall superheat.

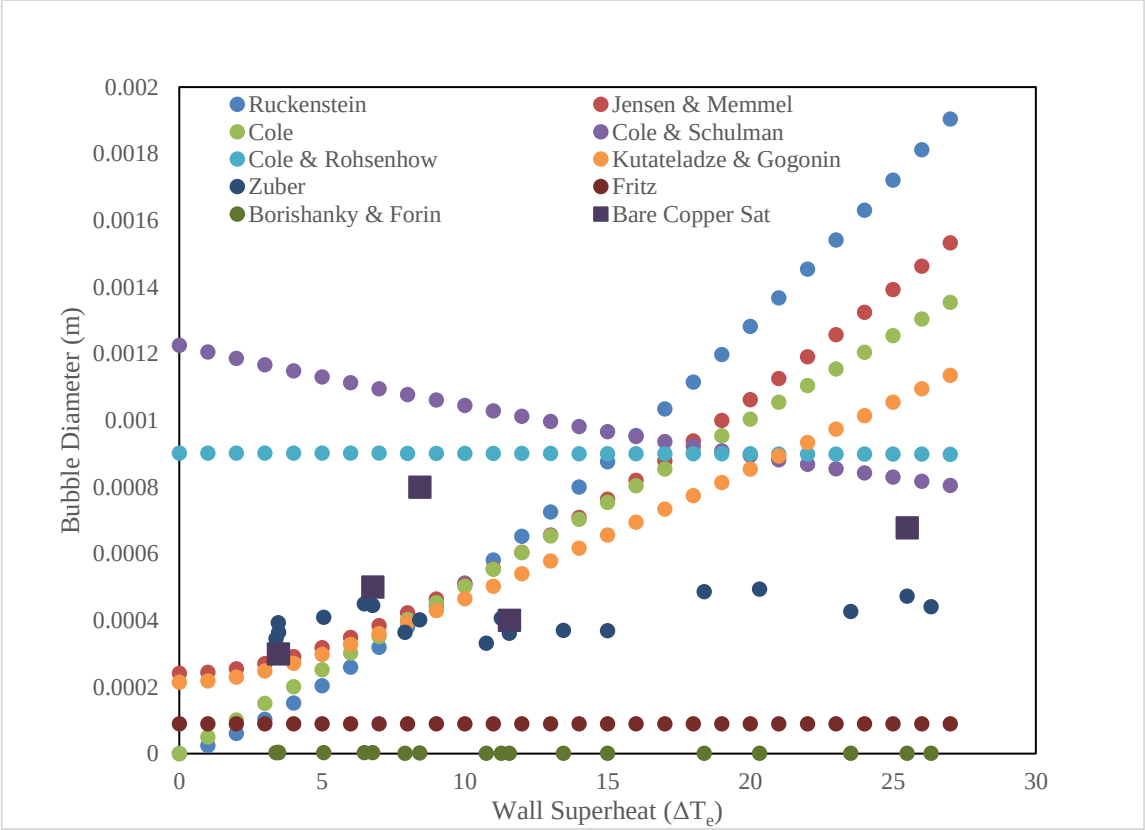

Figure 4-16 Comparison of the measured departure diameter for Copper heater at 0 °C subcooling and the predictions from the selected correlations as a function of the wall superheat.

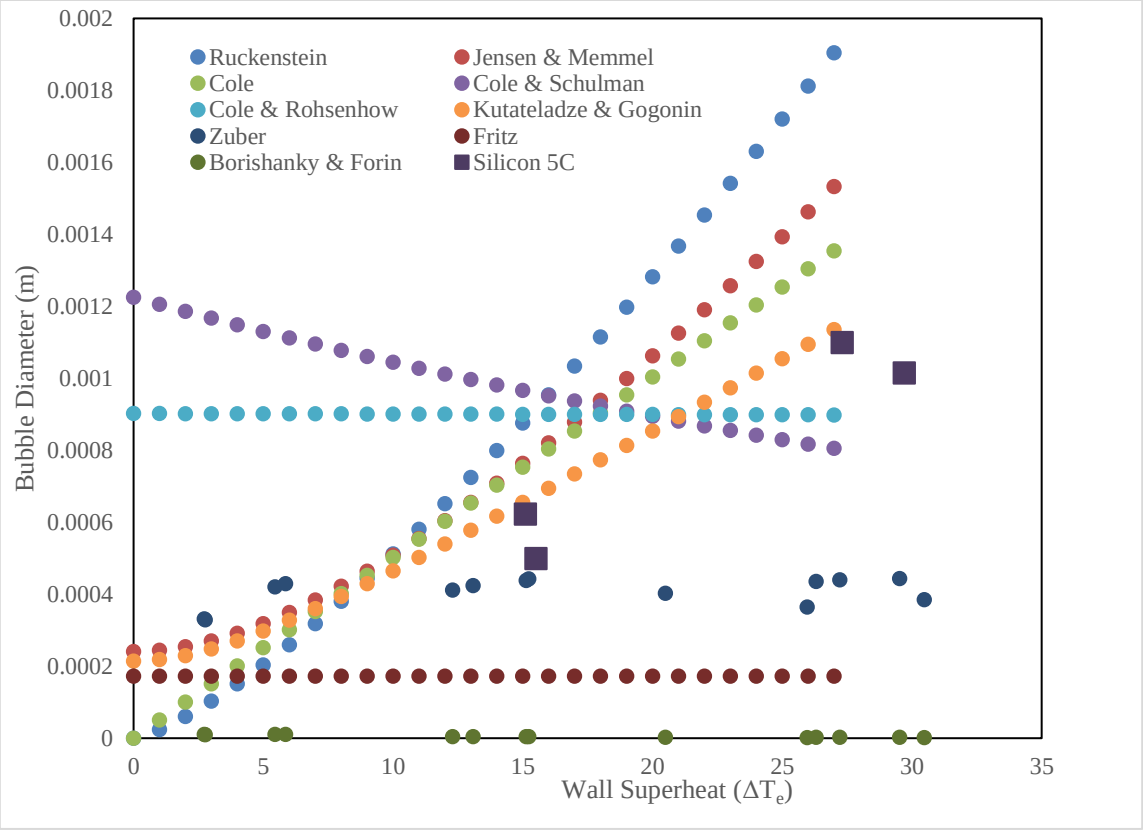

Figure 4-17 Comparison of the measured departure diameter for Silicon wafer at 5 °C subcooling and the predictions from the selected correlations as a function of the wall superheat.

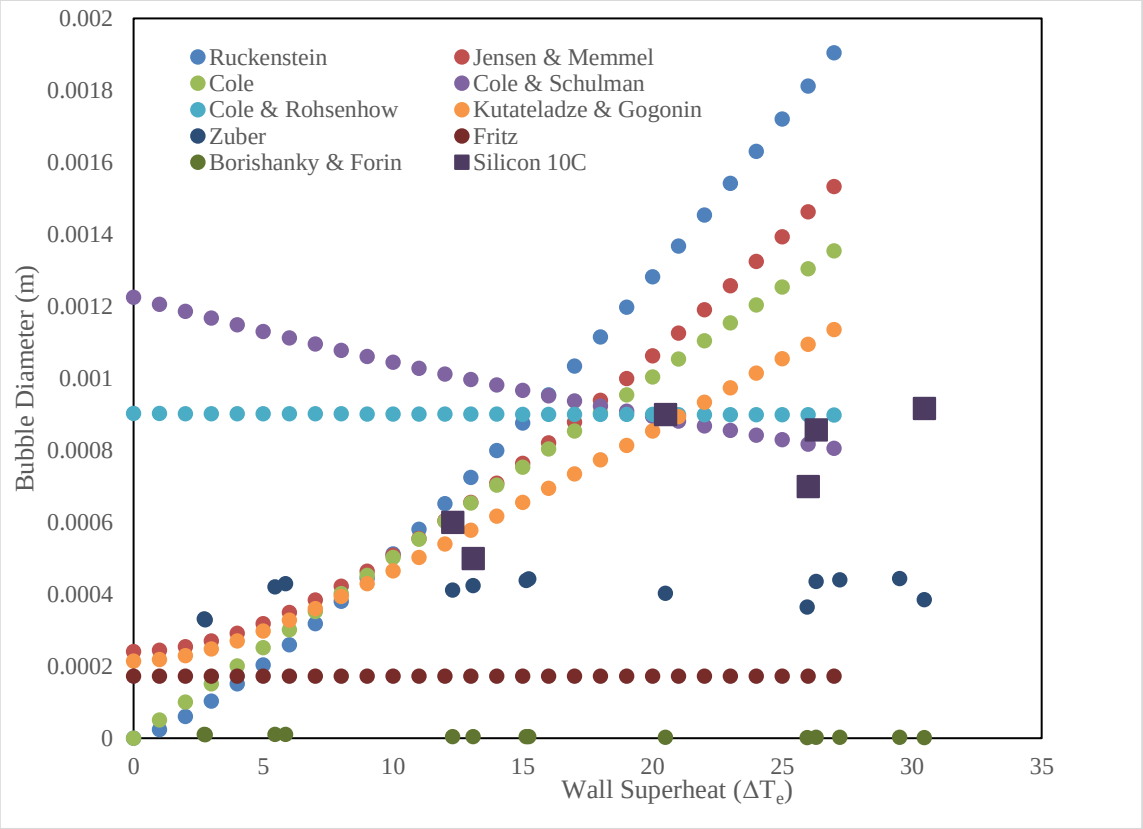

Figure 4-18 Comparison of the measured departure diameter for Silicon wafer at 10 °C subcooling and the predictions from the selected correlations as a function of the wall superheat.

The overall data for bubble departure diameter for AAO substrates showed a wide variability. The data for bubble departure diameter for the smaller values in the 5 °C subcooling experiments were observed to conform to the predictions obtained from the correlation proposed by Kutateladze and Gogonin. The data for bubble departure diameter for the smaller values in the 10 °C subcooling experiments were observed to conform to the predictions obtained from the correlation proposed by Jensen and Memmel (especially with the slight parabolic trend displayed at lower values of wall superheat).

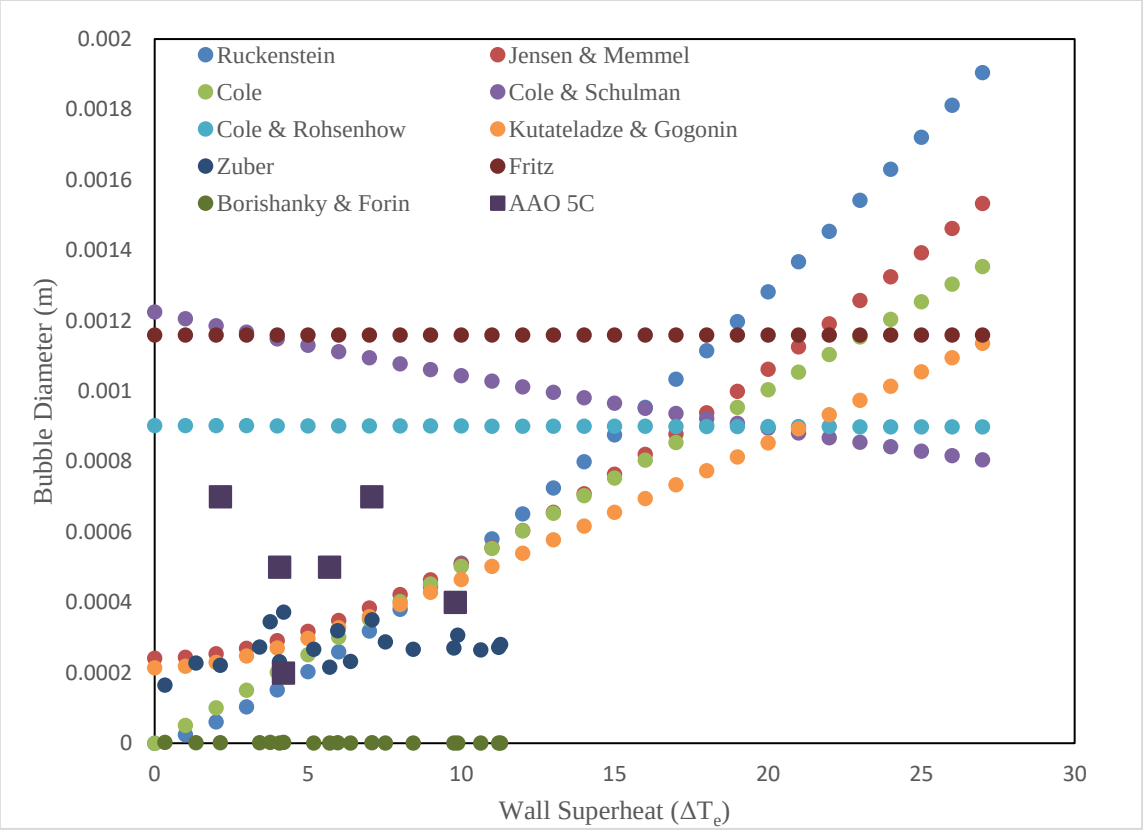

Figure 4-19 Comparison of the measured departure diameter for AAO substrates at 5 °C subcooling and the predictions from the selected correlations as a function of the wall superheat.

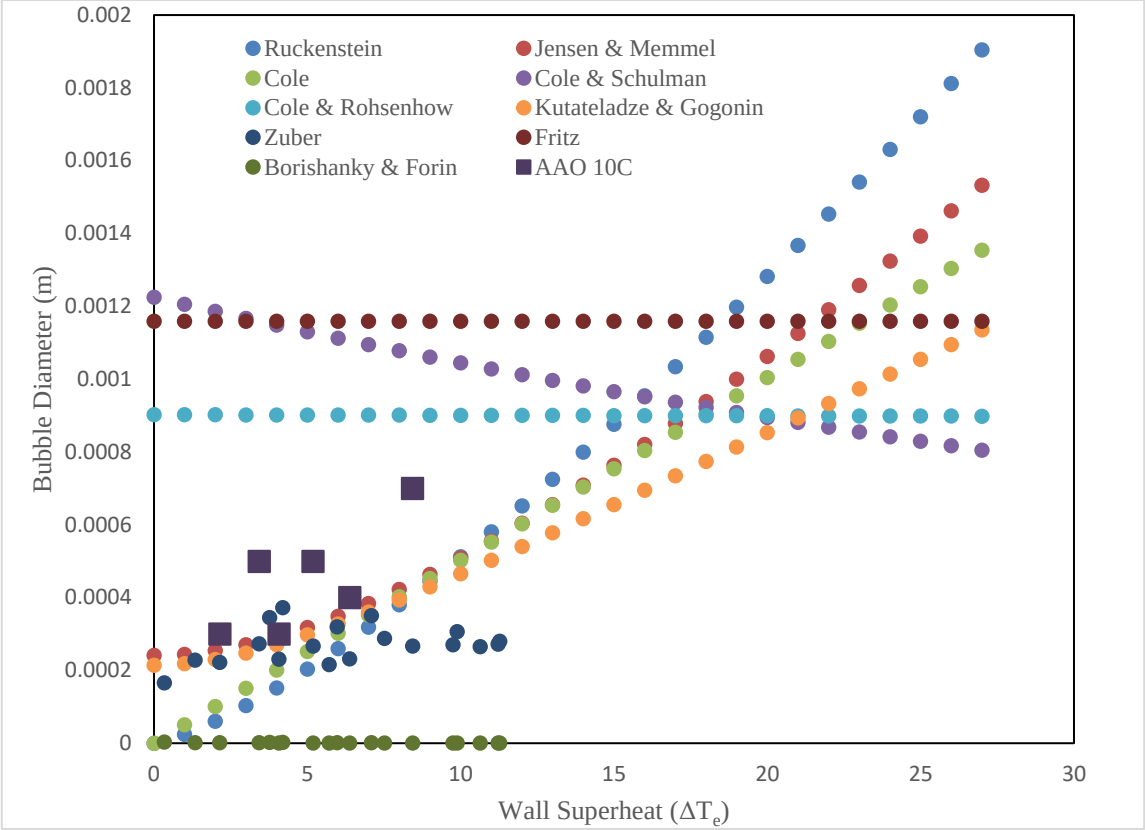

Figure 4-20 Comparison of the measured departure diameter for Copper heater at 10 °C subcooling and the predictions from the selected correlations as a function of the wall superheat.

Satisfactory agreement of the experimental data with the predictions from some of the correlations for the AAO surface is most likely coincidental, since the correlations do not account for properties of the nanostructured surfaces. The fluid properties are the most important factors in these correlations, as buoyancy force, surface tension and drag force play a dominant role in determining the values of bubble departure diameter. However these properties do not change considerably for different heater surfaces (except for the contact angle values).

In addition, these correlations were developed for plain surfaces (before heaters with nanostructured were in vogue). Since the boiling curves for each of the samples were within similar ranges, using boundary layer analyses (such as in Zuber's correlation) would not account for any significant differences attributable to different types of heater surfaces or material. The only parameter that changes significantly for different heater substrates, therefore, is the contact angle. The contact angles were measured to be (for PF-5060): 5 °C, 9.65 °C, and 65 °C for Copper heater, Silicon wafer, and AAO substrates, respectively. The departure diameters predicted by Fritz's correlation accounts for the variation in contact angle. However, none of the departure diameter data matched with Fritz's correlation spectacularly, which means that for a more appropriate correlation that is consistent for the AAO surface, additional factors would need to be taken into account to accurately predict the departure diameter.

The smaller departure diameters can be explained by exploring the equilibrium force diagram for a bubble at the point of departure. When a bubble departs, the buoyancy force (F_b) marginally exceeds the sum of the gravitational (F_g) and surface tension (F_s) forces acting on the bubble. Inertial and drag forces are excluded for simplification of the problem. Therefore, the forces are balanced at the point of bubble departure. Figure 4-21 demonstrates the forces acting on a vapor bubble.

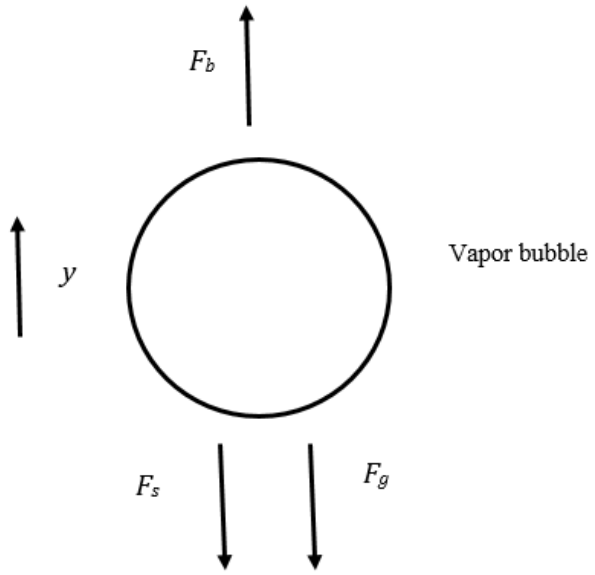

Figure 4-21 Equilibrium force diagram of the bubble, showing buoyancy force F_b, surface tension force F_s, and force of gravity F_g, acting on the bubble at the point of departure from a heater surface.

The expression for these forces are shown below:

$$F_b = \frac{\pi}{6} g \rho_l d_D^3 \tag{34}$$

$$F_g = \frac{\pi}{6} g \rho_v d_D^3 \tag{35}$$

The equation for surface tension force F_s is

$$F_s = C_g \sigma D_{cl} \tag{36}$$

where σ represents the surface tension, D_{cl} is the three-phase contact line length where the liquid and vapor interface occurs, and C_g is a geometric factor to limit only the vertical component of the force. Summing the forces at the point of equilibrium:

$$F_b - F_g = F_s \tag{37}$$

$$\frac{\pi}{6} g(\rho_l - \rho_v) d_D^3 = C_g \sigma D_{cl} \tag{38}$$

Departure diameter d_D is then mainly influenced by C_g and D_{cl}, since the remaining parameters are governed by the material properties of the working fluid. The physical properties of the test surfaces are included through the geometric factor C_g and the three phase contact line length (this accounts for the differences in bubble departure diameters for each test surface).

AAO surfaces have a slightly more complicated contact line configuration compared to plain surfaces. This configuration is due to the porous structure of the coating, since the liquid layer below the bubble would have multiple contact zones (inside and outside the nanopores). Vapor generation within the nanopores can potentially disrupt the contact line, causing the vapor liquid interface to traverse the gaps in between the pores (and thus have flows in non-continuum regimes). This would also cause the formation of "nanobubbles" in the nanopores (as discussed in Chapter 1). In addition, the contact line length on nanostructured surfaces are expected to be enhanced compared to that on plain surfaces. This increase in the total length of the contact line combined with the surface tension forces acting in various directions would drastically affect the C_g. This potentially causes the contact angle for AAO to be larger than for plain surfaces resulting in smaller values of departure diameter. Further research is needed to explore the effect of nanostructures on the contact line D_{cl} and the geometric factor C_g.

4.3.2 Departure Frequency

As previously stated, departure frequency (f_D) was measured by monitoring the number of frames between consecutive events of bubble departure at the same location on a heater surface. Locating individual bubbles that consistently departed from the same location was very challenging. Therefore, comparisons for frequency with different surfaces will be made for AAO in nucleate boiling with that of Copper heater and Silicon wafer. Similar comparisons were also obtained for the film boiling regime for Copper heater and Silicon wafer. Figures 4-22, 4-23, and 4-24 show the frequency measurements among the different surfaces and the measurements with uncertainty bars, respectively. The averages of the departure frequency measurements are also provided in Table 3.

Table 3 Average frequencies and absolute uncertainty for each surface

Frequency (Hz) for AAO							
	5C subcooling			10C subcooling			
Regime	Run 1	Run 2	Both	Run 1	Run 2	Both	All
Nucleate	25	45.3	35.1	18	25.6	21.8	28.5
ω_{Nuc}	46.4	33.6	40	48.7	29	38.9	39.4

Frequency (Hz) for Bare Copper						
	5C subcooling			10C subcooling		
Regime	Run 1	Run 2	Both	Run 1	Run 2	Both
Film	11	7.9	9.4	11.8	11.4	11.6
ω_{Film}	18.3	53.4	35.8	33.6	36.8	35.2
Nucleate	15	24.3	19.6	28.6	16	22.3
$\omega_{Nucleate}$	86.7	70.5	78.6	106.7	67.2	86.95

	Saturated			
	Run 1	Run 2	Both	All
Film	22.7	18.5	20.6	13.9
ω_{Film}	29.9	46.1	38	36.3
Nucleate	20.3	35.5	27.9	23.3
$\omega_{Nucleate}$	81.5	63.5	72.5	79.3

Frequency (Hz) for Bare Silicon							
	5C Subcooling			10C Subcooling			
Regime	Run 1	Run 2	Both	Run 1	Run 2	Both	All
Film	8.3	9.5	8.9	7.6	8.3	7.9	8.4
ω_{Film}	37.8	22.7	30.2	14.8	43.4	29.1	29.7
Nucleate	14.3	15.9	15.1	14	19	16.5	15.8
$\omega_{Nucleate}$	53.1	73.8	63.4	66.8	68.1	67.4	65.4

The average measurement uncertainty was calculated as a percentage value and listed in the table. The measurement uncertainty is shown to be higher for bubble departure frequency than to bubble departure diameter because fewer data points are available for these measurements (~60 measurements for frequency versus ~200 for departure diameter). Frequency measurements are increasingly more difficult to perform due to

limited availability of bubbles that consistently depart from a particular location. Scatter was also relatively larger for the departure frequency data set, as shown by the wide variability for standard deviation for frequency, which ranged from 5.5 Hz to 71 Hz. Data still shows that the average frequency for the AAO surface is significantly higher compared to that of the Copper heater and Silicon wafer surfaces (28.5 Hz vs 15.8 Hz and 23.3 Hz, respectively for AAO, Silicon and Copper). Since the quality of the videos need improvement, further verification will be needed for the frequency data with a larger set of measurements. The AAO surface demonstrates enhanced bubble departure frequency because of the smaller bubble departure diameter values. Less time is required for the bubble to reach the specified departure size, resulting in smaller time periods and larger values of bubble departure frequency.

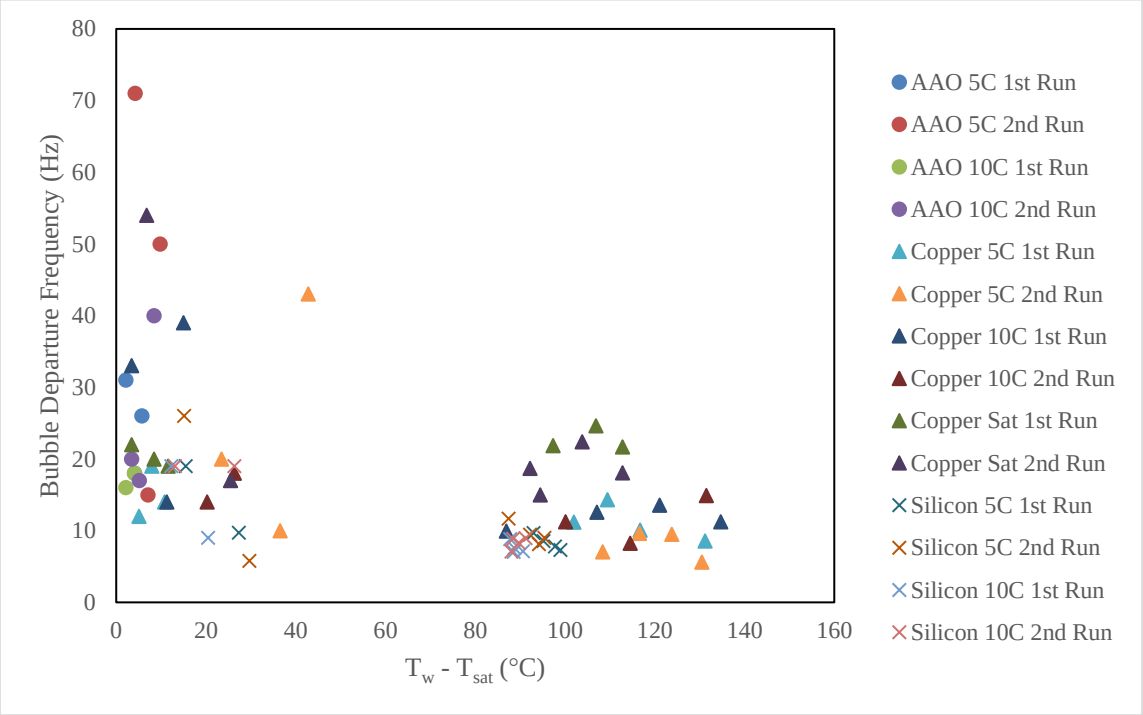

Figure 4-22 Plot of bubble departure frequency as a function of wall superheat.

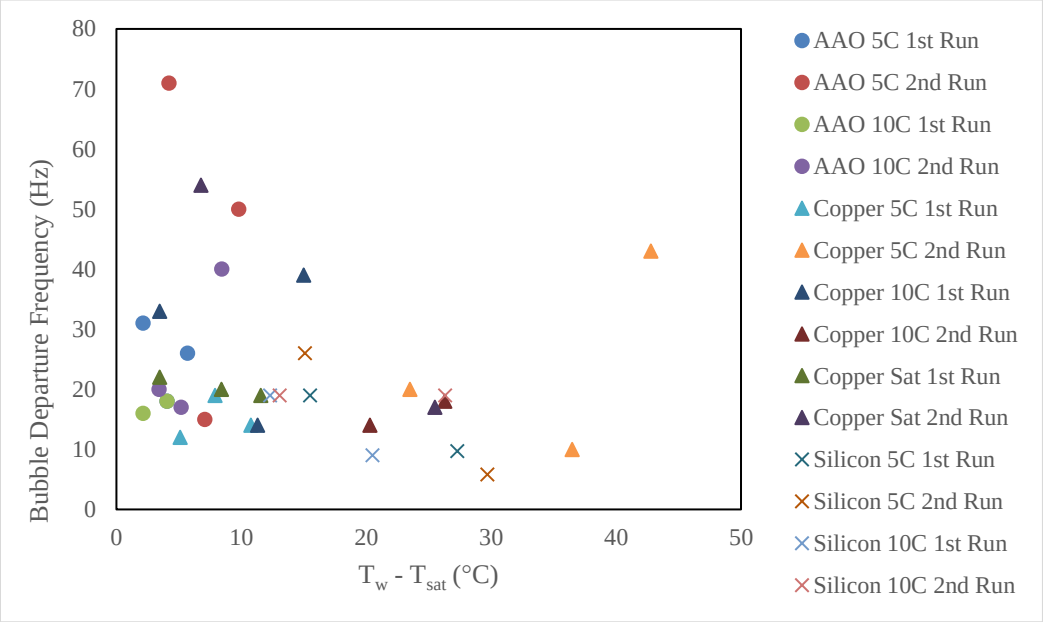

Figure 4-23 Plot of bubble departure frequency as a function of wall superheat in the nucleate boiling regime.

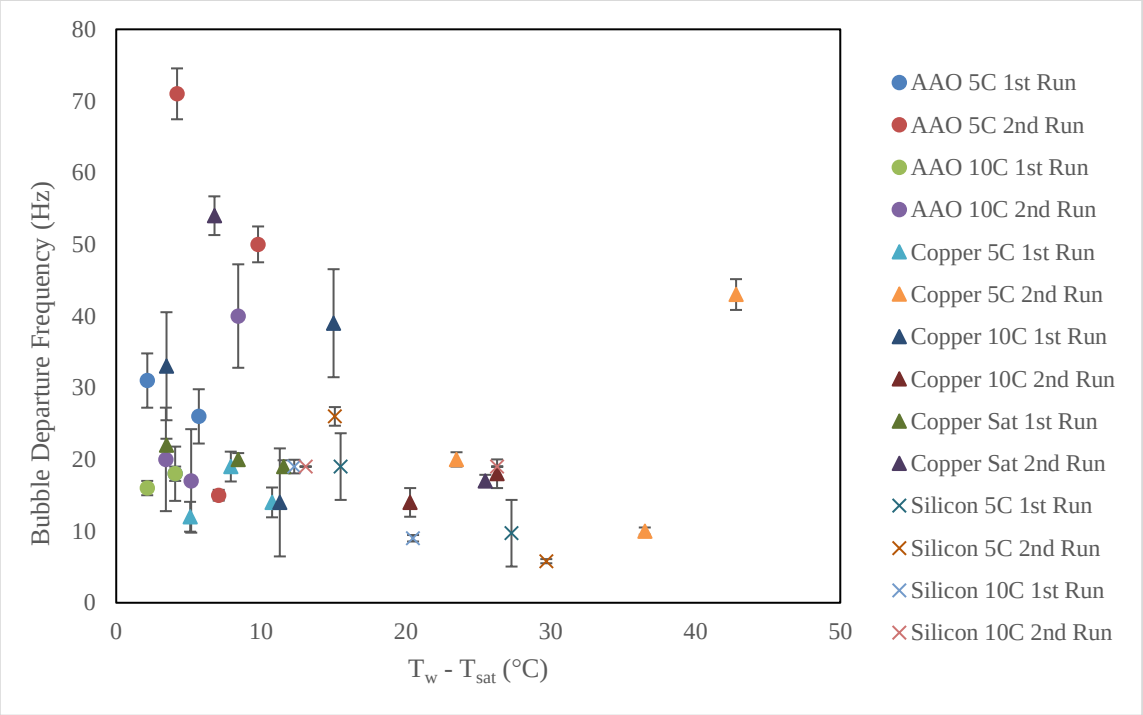

Figure 4-24 Plot of bubble departure frequency as a function of wall superheat showing estimates for measurement uncertainty in the nucleate boiling regime.

The frequency measurements showed a 22.3%-80% increase with the AAO surface compared to the plain surfaces. The departure diameter for AAO decreased by 12.5% - 45% from the plain surface departure diameters. The vapor volumetric flow rate has a cubic relationship with the departure diameter, which implies that nucleation site density would have an enhancement of about 390% in order to maintain the same latent thermal energy transfer rate. Investigations for increase in nucleation site density for CNT-coated samples were performed by Sathyamurthi et al. [25], but the enhancement in the values of nucleation site density were not quantified in this study. Glenn [20] performed calculations to estimate the enhancement in nucleation site density. The estimated maximum nucleation site density is calculated to be the inverse square of the average

departure diameter. For this study, it is estimated that there were 1.35 sites per mm^2 for Silicon, 3.3 sites per mm^2 for Copper, and 4.43 sites per mm^2 for AAO. Hence, there is significant increase in nucleation site density for AAO is (24%-228%) compared to plain surfaces. Further investigation is necessary to explore the effect of nanostructured surfaces on the nucleation site density (and how it relates to the bubble departure diameter and frequency).

4.3.3 Bubble Growth Rate

The figures displayed below are two examples of the growth rate of a bubble in the film boiling regime. Typically, the bubble would experience accelerated growth at inception and then plateau to a specific size before nucleation. In other cases, a bubble may also grow linearly with respect to time. Figures 4-25 and 4-26 show the typical path of the bubble growth rate until nucleation.

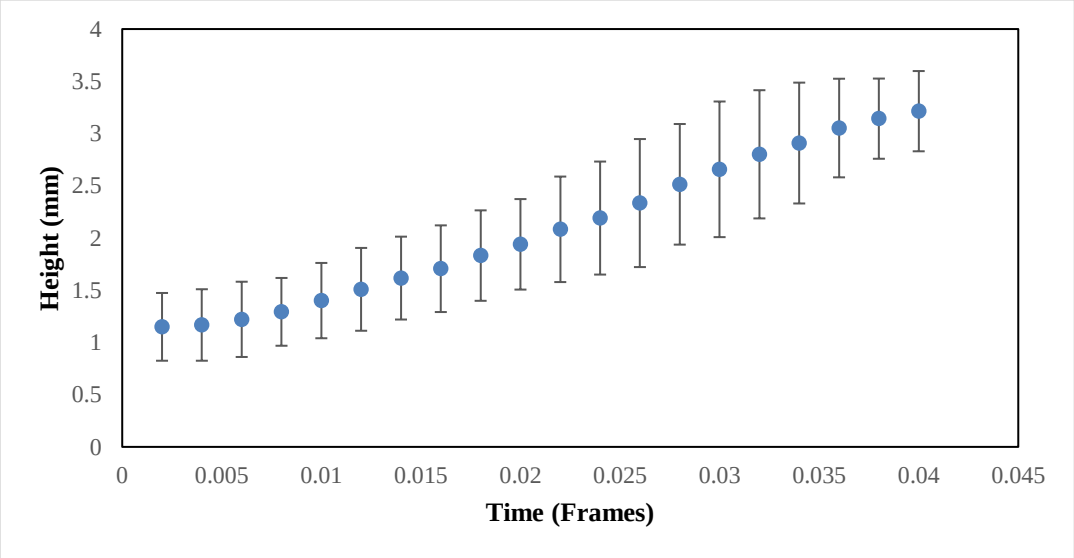

Figure 4-25 Height vs. time for a bubble at the silicon surface in 10°C subcooling and 87.8°C wall superheat

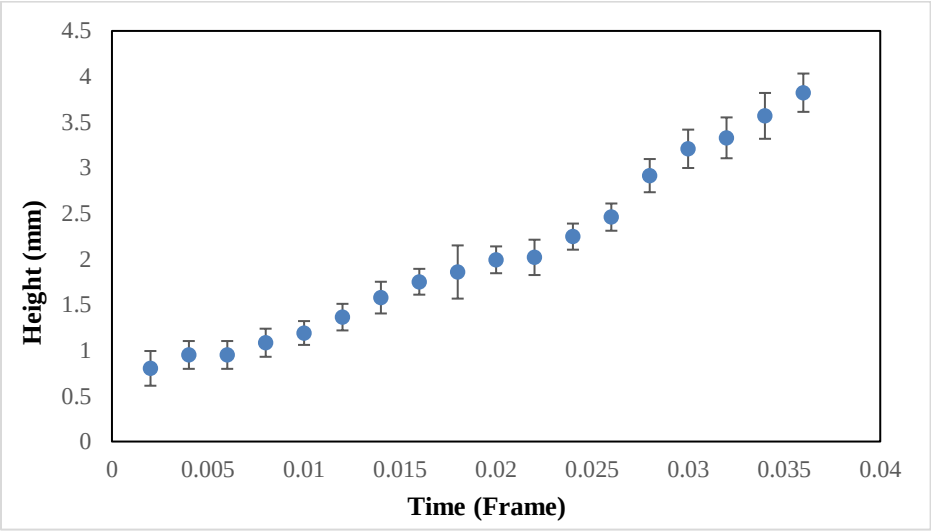

Figure 4-26 Height vs. time for a bubble at the copper surface at saturation temperature and 112.8°C wall superheat

Literature reports devoted to modeling the phenomenon of boiling incipience typically use continuum assumptions. However, AAO substrates consist of nano-pores and operate in the non-continuum flow regime. Hence, the conventional boiling inception models may not be applicable. The schematic below demonstrates a potential sequence of events that demonstrates the generation of vapor films (or supercritical phase of the test fluid) that eventually nucleate a larger vapor bubble on top of multiple nano-pores.

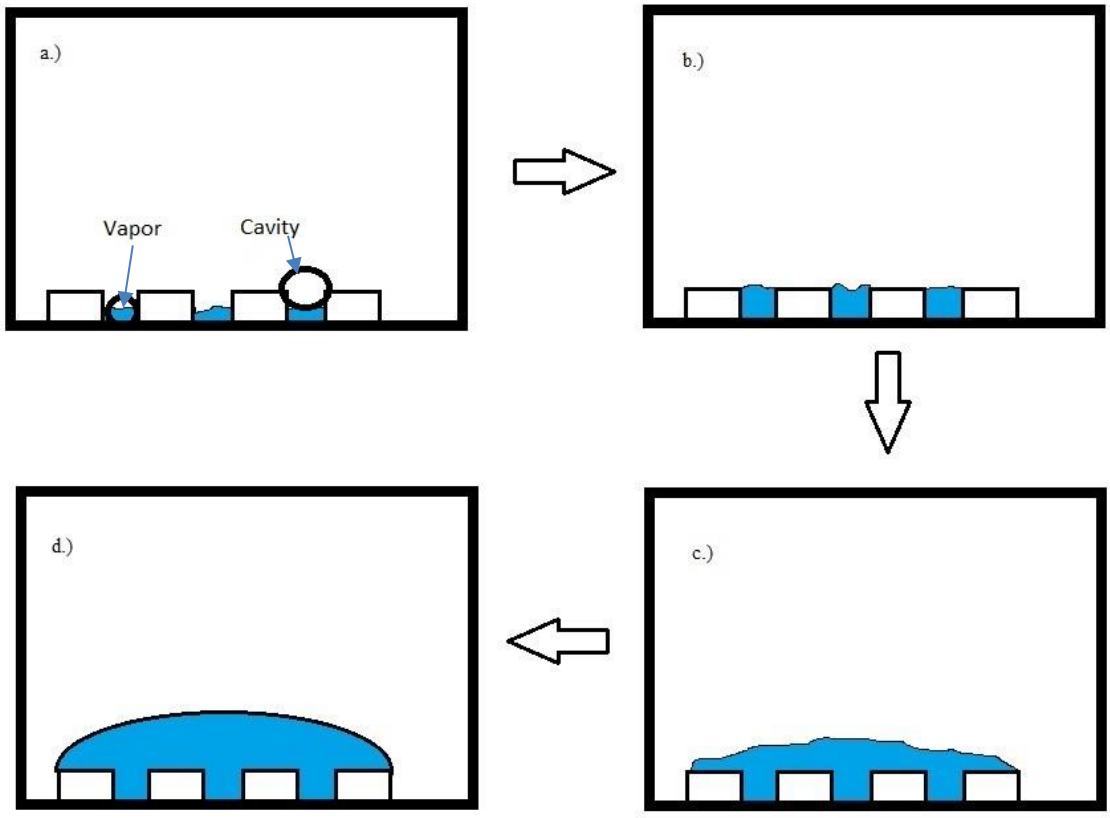

Figure 4-27 Bubble formation around the AAO nanostructure: a.) vapor (marked in blue) starts to form in between cavities (marked by the white boxes) b.) vapor builds, binding to the cavity and cohesive forces present in the liquid c.) the vapor forms a thin film as it nucleates to a bubble d.) bubble is formed and held together by surface tension.

5 SUMMARY AND CONCLUSION

5.1 Summary of Results

Pool boiling studies were performed for three different heater configurations: Copper heater, Silicon wafers, and Anodic Aluminum Oxide (AAO) substrates. The pool boiling experiments were performed for subcooled and saturated conditions. The experimental measurements involved automated recording of temperatures (from temperature nano-sensors or Thin Film Thermocouples/TFT and wire-bead thermocouples) using a digital data acquisition (DAQ) system. High speed digital image acquisition apparatus was used for flow visualization of the bubble nucleation and departure process on these heater surfaces. The experiments were performed using PF-5060 as the test fluid at atmospheric pressure. Each surface was tested in nucleate boiling at subcooling of 5 °C and 10 °C (in addition, saturated boiling experiments were performed for Copper heaters). Pool boiling experiments for the film boiling regime were performed for the plain heaters (Silicon wafer and Copper heater). After steady state conditions were achieved in each experiment, high speed videos of bubbles departing from the heater surface were acquired using the flow visualization apparatus at 500-1000 frames per second (fps). The acquired images were used to analyze the bubble departure diameter and bubble departure frequency values.

Boiling curves were obtained for each of the surfaces to enable comparison for the performance of these test surfaces for pool boiling. While critical heat flux (CHF) was around the same range for both silicon wafer and AAO substrates, Copper heater

demonstrated significantly higher values of CHF. However, AAO surfaces demonstrated significantly higher values of heat flux at boiling incipience.

Results obtained from the flow visualization experiments show that the bubble departure diameters were reduced by ~50% for AAO substrates compared to that of Silicon wafer and Copper heaters. The bubble departure frequency was enhanced by 20 - 80% for AAO substrates compared to that of the plain heaters. This implies that the bubble nucleation site density was enhanced by 25 ~ 230 % for AAO compared to that of the plain surfaces.

In addition, the departure diameter values were smaller at 10°C subcooling compared to that of 5°C subcooling (for all of the surfaces). Upon comparison of the experimental data with a selected set of correlations in the literature it was observed that the experimental data for Copper heater and Silicon wafers partially conformed to predictions obtained from some of these selected correlations. However, the data for AAO surfaces were found to marginally match these correlations – no consistent conformance was obtained between the experimental data and the predictions obtained from these selected correlations. It is likely that the similarities between the predictions from the correlations with the experimental data for bubble departure diameter for AAO substrates was mostly coincidental, since the correlations from literature did not consistently predict behavior for nanostructured surfaces (these surfaces were not in vogue at the time of development of these correlations). The correlations that were consistent with the experimental data for these heater configurations include: the Kutateladze and Gogonin correlation; and the Cole and Rohsenhow correlation. Additional investigations are

recommended for various combinations of nanopore morphologies for AAO substrates (diameter, pitch, depth, etc.).

5.2 Future Directions

A recurring problem for heater surfaces before and after boiling is fouling of heater surfaces (residue formation can affect the surface properties which in turn can affect the dynamics of bubble nucleation and departure as well as heat flux and wall superheat values). Hence fouling can affect pool boiling heat transfer significantly. Dispersed fouling can lead to formation of nanofins and cause enhancement of pool boiling heat flux. In contrast, excessive fouling can degrade the pool boiling heat flux values. This is a consequence of the "nanoFin Effect (nFE)".

Proper design of experiments are needed to analyze the effect of fouling on pool boiling. Fouling in heater surfaces can be studied by parametric variation of patterned deposition of resides on top of nanostructures surfaces. This is recommended as a future topic of investigation involving pool boiling studies for nanostructured surfaces.

Studies can also be designed to determine where nucleation occurs for the AAO surface. Since AAO substrates have nanoporous features it is difficult to ascertain the nature of bubble nucleation on these surfaces. The non-continuum flow regimes in these nanoscale cavities can violate the assumptions typically used in deriving conventional theories for heterogeneous nucleation of bubbles. Formation of nanobubbles from these nanoporous cavities beg novel theories for heterogeneous nucleation of bubbles. Development of novel theories for bubble nucleation on nanostructured surfaces can help

optimize the morphologies (cavity geometry, materials, etc.) of these nanoporous substrates.

In combination with additional bubble departure frequency measurements (as well as additional data for bubble nucleation site density and bubble departure diameter) combined with the measurements obtained from the current study, estimates for pool boiling heat flux data can be obtained with lower values of measurement uncertainty.

Additional studies are also needed to account for the effects of the static and dynamic contact line configurations on nanostructured surfaces (such as from AAO substrates). Such studies can help to predict the contact angle on nanostructures surfaces, which in turn, can help to predict the level of reduction in the bubble departure diameter for these types of heater configurations (with and without fouling).

REFERENCES

[1] Bergman, T.L., Incropera, F.P., Lavine, A.S. *Fundamentals of Heat and Mass Transfer*. John Wiley & Sons, Hoboken (2011).

[2] Jensen, M. K. and Memmel, G. J. "Evaluation of Bubble Departure Diameter Correlations." *Proceedings of the Eighth International Heat Transfer Conference*. pp. 1907-1912. San Francisco, CA, 1986.

[3] Kutateladze, S. and Gogonin, I. "Growth Rate and Detachment Diameter of a Vapor Bubble in Free Convection Boiling of a Saturated Liquid." *Teplofizika Vysokikh Temperatur* Vol. 17 (1979): pp. 792-797.

[4] Carey, Van P. *Liquid Vapor Phase Change Phenomena*. Hemisphere Publishing Corporation, New York (1992).

[5] Attard, P. "Nanobubbles and the Hydrophobic Attraction." *Advances in Colloid and Interface Science* Vol. 104 No. 1 (2003): pp. 75-91.

[6] Miljkovic, N., Enright, R., Youngsuk, N., Lopez, K., Dou, N., Sack, J., and Wang E. N. "Jumping-Droplet Enhanced Condensation on Scalable Superhydrophobic Nanostructured Surfaces." *Nano Letters* Vol. 13 No. 1 (2012): pp. 179-187.

[7] Miljkovic, N., Enright, R. and Wang, E. N. "Effect of Droplet Morphology on Growth Dynamics and Heat Transfer During Condensation on Superhydrophobic Nanostructured Surfaces." *ACS Nano* Vol. 6 No. 2 (2012): pp. 1776-1785.

[8] Enright, R., Miljkovic, N., Alvarado, J. L., Kim, K., and Rose, J. W. "Dropwise Condensation on Micro- and Nanostructured Surfaces." *Nanoscale and Microscale Thermophysical Engineering* Vol. 18 No. 3 (2014): pp. 223-250.

[9] Lu, M. C., Chen, R., Srinivasan, V., Carey, V. P., and Majumdar, A. "Critical Heat Flux of Pool Boiling on Si Nanowire Array-Coated Surfaces." *International Journal of Heat and Mass Transfer* Vol. 54 No. 25 (2011): pp. 5359-5367.

[10] Bang, I. C. and Jeong, J. H. "Nanotechnology for Advanced Nuclear Thermal-Hydraulics and Safety: Boiling and Condensation." *Nuclear Engineering and Technology* Vol. 43 No. 3 (2011): pp. 217-242.

[11] Kim, D. E., Yu, D. I., Jerng, D. W., Kim, M. H., and Ahn, H. S. "Review of Boiling Heat Transfer Enhancement on Micro/Nanostructured Surfaces." *Experimental Thermal and Fluid Science* Vol. 66 (2015): pp. 173-196.

[12] Hu, H., and Sun, Y. "Effect of Nanopatterns on Kapitza Resistance at a Water-Gold Interface During Boiling: A Molecular Dynamics Study." *Journal of Applied Physics* Vol. 112 No. 5 (2012): pp. 1-6.

[13] Kwark, S. M., Amaya, M., Kumar, R., Moreno, G., You, S. M. "Effects of Pressure, Orientation, and Heater Size on Pool Boiling of Water with Nanocoated Heaters." *International Journal of Heat and Mass Transfer* Vol. 53 No. 23 (2010): pp. 5199-5208.

[14] C. Hutter and e. al., "Nucleation Site Interaction Between Artificial Cavities During Nucleate Pool Boiling on Silicon with Integrated Micro-Heater and

Temperature Micro-Sensors," *International Journal of Heat and Mass Transfer* Vol. 55 No. 11 (2012): pp. 2769-2778.

[15] Hutter, C., Kenning, D. B. R., Sefiane, K., Karayiannis, T.G., Lin, H., Cummins, G., and Walton, A.J. "Experimental Pool Boiling Investigations of FC-72 on Silicon with Artificial Cavities and Integrated Temperature Microsensors." *Experimental Thermal and Fluid Science* Vol. 34 No. 4 (2010): pp. 422-433.

[16] Lee, C. Y., Bhuiya, M. M. H., and Kim, K. J. "Pool Boiling Heat Transfer with Nano-Porous Surface." *International Journal of Heat and Mass Transfer* Vol. 53 No. 19 (2010): pp. 4274-4279.

[17] El-Genk, M. S. and Ali, A. F. "Enhanced Nucleate Boiling on Copper Micro-Porous Surfaces." *International Journal of Multiphase Flow* Vol. 36 No. 10 (2010): pp. 780-792.

[18] Ujereh, S., Fisher, T., and Mudawar, I. "Effects of Carbon Nanotube Arrays on Nucleate Pool Boiling." *International Jounral of Heat and Mass Transfer* Vol. 50 No. 19 (2007): pp. 4023-4038.

[19] Kim, H. D., Kim, J., and Kim, M. H. "Experimental Studies on CHF Characteristics of Nano-Fluids at Pool Boiling." *International Journal of Multiphase Flow* Vol. 33 No. 7 (2007): pp. 691-706.

[20] Glenn, S. T. “Effects of Carbon Nanotube Coating on Bubble Departure Diameter and Frequency in Pool Boiling on a Flat, Horizontal Heater.” Masters Thesis. Texas A&M University, College Station, TX. 2009.

[21] S. Anand and e. al., "Enhanced Condensation on Lubricant-Impregnated Nanotextured Surfaces." *ACS Nano* Vol. 6 No. 11 (2012): pp. 10122-10129.

[22] Hsu, C. C., Su, T. W., and Chen, P. H. "Pool Boiling of Nanoparticle Modified Surface with Interlaced Wettability." *Nanoscale Research Letters* Vol. 7 No. 1 (2012): pp. 1-7.

[23] Ahn, H. S., Park, G., Kim, J. M., Kim, J., and Kim, M. H. "The Effect of Water Absorption on Critical Heat Flux Enhancement During Pool Boiling." *Experimental Thermal and Fluid Science* Vol. 42 (2012): pp. 187-195.

[24] Li, C., Wang, Z., Wang, P., Peles, Y., Koratkar, N., and Peterson, G. P. "Nanostructured Copper Interfaces for Enhanced Boiling." *Small* Vol. 4 No. 8 (2008): pp. 1084-1088.

[25] Sathyamurthi, V., Ahn, H. S., Banerjee, D., and Lau, S. C. "Subcooled Pool Boiling Experiments on Horizontal Heaters Coated with Carbon Nanotubes." *J. Heat Transfer* Vol. 131 (2009): pp. 1-10.

[26] Dong, L., Quan, X., and Cheng, P. "An Experimental Investigation of Enhanced Pool Boiling Heat Transfer from Surfaces with Micro/Nanostructures." *International Journal of Heat and Mass Transfer* Vol. 71 (2014): pp. 189-196.

[27] Zhang, Y., Wei, J., Xue, Y., Kong, X., and Zhao, J. "Bubble Dynamics in Nucleate Pool Boiling on Micro-Pin-Finned Surfaces in Microgravity." *Applied Thermal Engineering* Vol. 70 No. 1 (2014): pp. 172-182.

[28] Zou, A., and Maroo, S. C. "Critical Height of Micro/Nano Structures for Pool Boiling Heat Transfer Enhancement." *Applied Physics Letters* Vol. 103 No. 22 (2013): pp. 1-6.

[29] Launay, S., Fedorov, A. G., Joshi, Y., Cao, A., and Ajayan, P. M. "Hybrid Micro-Nano Structured Thermal Interfaces for Pool Boiling Heat Transfer Enhancement." *Microelectronics Journal* Vol. 37 No. 11 (2006): pp. 1158-1164.

[30] Ahn, H. S., Sathyamurthi, V., and Banerjee, D. "Pool Boiling Experiments on a Nano-Structured Surface." *IEEE Transactions on Components and Packaging Technologies* Vol. 32 No. 1 (2009): pp. 156-165.

[31] Rahman, M. M., King, S. M., Olceroglu, E., and McCarthy, M. "Nucleate Boiling on Biotemplated Nanostructured Surfaces." *ASME 2012 International Mechanical Engineering Congress and Exposition*. pp. 1- 8. Houston, TX, November 9-15, 2012.

[32] Hamzekhani, S., Falahieh, M. M., Kamalizadeh, M. R., and Nazari, Z. "Experimental Study on Bubble Departure Frequency for Pool Boiling of Water/NaCl Solutions." *Heat and Mass Transfer* (2015): pp. 1-8.

[33] Peyghambarzadeh, S. M., Hatami, A., Ebrahimi, A., Alavi Fazel, S.A. "Photographic Study of Bubble Departure Diameter in Saturated Pool Boiling to Electrolyte Solutions." *Chemical Industry and Chemical Engineering Quarterly* Vol. 20 No. 1 (2014): pp. 143-153.

[34] Cole, R. "Bubble Frequencies and Departure at Subatmospheric Pressures." *AIChE Journal* Vol. 13 No. 4 (1967): pp. 779-783.

[35] Cole, R., and Shulman, H. L. "Bubble Departure Diameters at Substmospheric Pressures." *Chemical Engineers Progress Symposium Series* Vol. 62 No. 64 (1966): pp. 6-16.

[36] Cole, R., and Rohsenow, W. M. "Correlation of Bubble Departure Diameters for Boiling of Saturated Liquids." *Chemical Engineers Progress Symposium Series* Vol. 65 No. 92 (1969): pp. 211-213.

[37] Ruckenstein, E. "A Physical Model for Nucleate Boiling Heat Transfer from a Horizontal Surface." *Buletinul Institutului Politehnic Bucuresti* Vol. 23 (1961): pp. 79-84.

[38] Zuber, N. "The Dynamics of Vapor Bubbles in Nonuniform Temperature Fields." *International Journal of Heat and Mass Transfer* Vol. 2 No. 1 (1961): pp. 83-98.

[39] Chen, R., Lu, M., and Srinivasan, V. "Nanowires for Enhanced Boiling Heat Transfer." *Nano Letters* Vol. 9 No. 2 (2009): pp. 548-553.

[40] Bon, B. "The Role of Surface Microstructure and Topography in Pool Boiling Heat Transfer." PhD Dissertation. University of Florida, Gainesville, FL. 2011.

[41] Lienhard, J. H., and Dhir, V. K. "Hydrodynamic Prediction of Peak Pool-Boiling Heat Fluxes from Finite Bodies." *Journal of Heat Transfer-Transactions of the ASME* Vol. 95 No. 2 (1973): pp. 152-158.

[42] Lienhard, J. H., Dhir, V. K., and Riherd, D. M. "Peak Pool Boiling Heat-Flux Measurements on Finite Horizontal Flat Plates." *Mechanical Engineering* Vol. 96 No. 4 (1973): pp. 479-482.

[43] Liter, Scott G., and Kaviany, Massoud. “Pool-boiling CHF enhancement by modulated porous-layer coating: theory and experiment.” *International Journal of Heat and Mass Transfer* Vol. 44 No. 22 (2011): pp. 4287-4311.

[44] Park, J. J., and Taya, M. "Design of Micro-Temperature Sensor Array with Thin Film Thermocouples." *Journal of Electronic Packaging* Vol. 127 No. 3 (2005): pp. 286-289.

[45] Kreider, K. G., and DiMeo, F. "Platinum/Palladium Thin-Film Thermocouples for Temperature Measurements on Silicon Wafers." *Sensors and Actuators A-Physical* Vol. 69 No. 1 (1998): pp. 46-52.

[46] Kreider, K. G., and Gillen, G. "High Temperature Materials for Thin-Film Thermocouples on Silicon Wafers." *Thin Solid Films* Vol. 376 No. 1-2 (2000): pp. 32-37.

[47] Sathyamurthi, V. “Experimental and Numerical Investigation of Pool Boiling on Engineered Surfaces with Integrated Thin-Film Temperature Sensors.” PhD Dissertation. Texas A&M University, College Station, TX. 2011.

[48] Sinha, N. “Design, Fabrication, Packaging and Testing of Thin Film Thermocouples for Boiling Studies.” Texas A&M University, College Station, TX. 2006.

[49] Sathyamurthi, V., and Banerjee, D. "Determination of Dimensionality of Pool Boiling on a Thin Horizontal Disk Under Subcooled Conditions Using Thin-Film Thermocouples." *Proceedings of 2008 ASME Summer Heat Transfer Conference*. HT2008-56378: pp. 1-11. Jacksonville, FL, August 10-14, 2008.

[50] Ahn, H. S., Sathyamurthi, V., Sinha, N., Lau, S., and Banerjee, D. "Boiling Experiments on Vertically Aligned Carbon Nanotubes and Using Surface Micromachined Thin Film Thermocouple (TFT)." *9th AIAA/ASME Joint Thermophysics and Heat Transfer Conference*. AIAA2006-2916: pp. 1-10. San Francisco, CA, June 5-8, 2006.

[51] Singh, N., and Banerjee, D. *Nanofins: Science and Applications*. Springer, New York City (2013).

[52] Yang, H. “Experimental and Numerical Investigation of Pool Boiling Heat Transfer on Engineered Nano-Finned Surfaces.” PhD Dissertation. Texas A&M University, College Station, TX. 2014.

[53] Banerjee, D., Son, G., and Dhir, V. "Conjugate Thermal and Hydrodynamic Analyses of Saturated Film Boiling from a Horizontal Surface." *ASME Heat Transfer Div Publ HTD* Vol. 334 No. 3 (1996): pp. 57-64.

[54] Sugawara, H., Ohkubo, T., Fukushima, T., and Iuchi, T. "Emissivity Measurement of Silicon Semiconductor Wafer near Room Temperature." *SICE Annual Conference*. pp. 2201 – 2204. Fukui, Japan, August 4-6, 2003.

[55] "Anodic Aluminum Oxide (AAO) - Nano & Microfabrication." Synkera, Inc., 2016. [Online]. Available: http://www.synkerainc.com/technology/nano-microfabrication/anodic-alumina.

[56] Fritz, W. "Berechnung des Maximalvolume von Dampflblasen," *Phys Z* Vol. 36 (1935): pp. 379-388.

[57] Borishansky, V. M., and Fokin, F. S. "Heat Transfer and Hydrodynamics in Steam Generators." *Trudy TsKTI* Vol. 62 (1963): p. 1.

APPENDIX

Table A1 Variation of heat flux, departure diameter, and departure frequency with superheat for Silicon at 5°C Subcooling (Run 1)

Superheat (°C)	Heat Flux (W/m^2)	Absolute Uncertainty (W/cm^2)	Departure Diameter (mm)	Diameter Uncertainty (mm)	Frequency (Hz)	Frequency Uncertainty (Hz)
5.9	1.85E+04	2.70E+03	0.47	0.09		
			0.41	0.09		
			0.42	0.09		
			0.44	0.09		
			0.59	0.14		
			0.47	0.12		
			0.48	0.12		
			0.45	0.12		
			0.71	0.12		
			0.44	0.12		
15.2	4.34E+04	2.81E+03			38.5	0.31
					18.5	0.15
					13.9	0.11
					17.2	0.14
27.2	7.97E+04	2.76E+03	0.79	0.13	11.1	0.09
			0.91	0.16	10.4	0.08
			1.16	0.19	10.5	0.04
			0.79	0.13	7.7	0.06
			0.84	0.16		
			1.73	0.32		
			1.41	0.24		
			1.31	0.24		
			1.04	0.18		
			1.26	0.26		
34.7	1.21E+05	2.74E+03	1.4	0.23		
			1.33	0.21		
			1.3	0.19		
			1.04	0.14		
			1.02	0.2		
			0.99	0.25		
			1.11	0.16		
			1.07	0.12		

			1.02	0.14		
			1.09	0.12		
93.5	8.17E+04	2.89E+03	7.03	0.29	8.2	0.07
			4.82	0.2	9.6	0.08
			7.99	0.31	12.8	0.1
			8.03	0.27	9.1	0.07
			8.06	0.24		
			8.14	0.34		
			8.81	0.34		
			9.45	0.29		
			8.11	0.29		
			5.2	0.24		
95.5	8.47E+04	2.83E+03	4	0.21	8.2	0.07
			3.49	0.33	8.1	0.03
			3.48	0.34	9.6	0.08
			3.67	0.29	8.5	0.02
			3.56	0.29		
			3.85	0.29		
			4.22	0.26		
			3.45	0.32		
			3.24	0.29		
			3.45	0.28		
97.7	8.66E+04	2.79E+03	3.81	0.2	7.5	0.03
			4.16	0.23	8.6	0.03
			3.9	0.23	7.6	0.03
			3.65	0.31	7.5	0.03
			3.23	0.31		
			3.6	0.2		
			3.04	0.26		
			3.53	0.25		
			4.25	0.25		
			3.3	0.29		
99.0	8.92E+04	2.83E+03	3.4	0.32	7.8	0.02
			2.63	0.29	13.2	0.03
			2.5	0.2	5.0	0.01
			2.58	0.23	6.9	0.01
			2.88	0.25		
			3.57	0.28		

			2.87	0.23		
			2.86	0.27		
			2.99	0.21		
			3.32	0.23		

Table A2 Variation of heat flux, departure diameter, and departure frequency with superheat for Silicon at 5°C Subcooling (Run 2)

Superheat (°C)	Heat Flux (W/m^2)	Absolute Uncertainty (W/cm^2)	Departure Diameter (mm)	Diameter Uncertainty (mm)	Frequency (Hz)	Frequency Uncertainty (Hz)
5.4	1.83E+04	2.69E+03				
15.1	4.48E+04	2.78E+03	0.56	0.08	18.5	0.07
			0.8	0.11	23.3	0.09
			0.6	0.11	28.6	0.11
			0.64	0.12	47.6	0.19
			0.58	0.11		
			0.49	0.09		
			0.66	0.14		
			0.64	0.11		
			0.68	0.11		
			0.6	0.11		
29.5	8.43E+04	2.71E+03	0.81	0.12	12.2	0.1
			0.85	0.15	5.4	0.04
			0.97	0.14	4.0	0.03
			1.03	0.14		
			0.81	0.11		
			1.33	0.17		
			0.91	0.16		
			0.87	0.12		
			1.35	0.18		
			1.23	0.19		
33.8	1.21E+05	2.73E+03	1.89	0.26		
			1.65	0.2		
			1.59	0.17		
			1.41	0.15		
			1.63	0.19		
			1.73	0.21		

			1.19	0.13		
			1.33	0.16		
			1.17	0.17		
			1.41	0.19		
88.3	7.68E+04	2.79E+03	2.88	0.28	10.6	0.09
			3.25	0.29	12.8	0.1
			2.96	0.25	12.2	0.1
			4.05	0.33	11.4	0.05
			2.97	0.28		
			2.68	0.34		
			3.24	0.3		
			3.35	0.3		
			2.78	0.19		
			2.76	0.29		
91.3	8.01E+04	2.77E+03	2.65	0.27	8.9	0.07
			3.62	0.27	9.4	0.04
			3.68	0.26	10.6	0.09
			3.08	0.27	8.9	0.07
			2.83	0.23		
			3.83	0.26		
			3.73	0.28		
			3.25	0.27		
			2.95	0.26		
			3.07	0.28		
94.2	8.34E+04	2.83E+03	3.49	0.26	7.8	0.03
			3.84	0.28	8.1	0.03
			3.17	0.27	9.2	0.04
			3.85	0.25	7.7	0.03
			3.17	0.27		
			3.38	0.24		
			3.52	0.24		
			3.98	0.29		
			3.66	0.28		
			3.89	0.23		
95.3	8.63E+04	2.80E+03	3.17	0.3	7.9	0.06
			4.3	0.38	7.0	0.06
			3.95	0.25	8.9	0.07
			3.34	0.3	7.4	0.06

			3.45	0.2		
			3.26	0.26		
			3.26	0.31		
			3.67	0.31		
			3.81	0.26		
			3.81	0.23		

Table A3 Variation of heat flux, departure diameter, and departure frequency with superheat for Silicon at 10°C Subcooling (Run 1)

Superheat (°C)	Heat Flux (W/m^2)	Absolute Uncertainty (W/cm^2)	Departure Diameter (mm)	Diameter Uncertainty (mm)	Frequency (Hz)	Frequency Uncertainty (Hz)
2.7	1.87E+04	2.74E+03				
12.3	4.42E+04	2.73E+03	0.7	0.1	55.6	0.22
			0.63	0.08	25.6	0.1
			0.53	0.05	18.2	0.07
			0.63	0.1	15.2	0.06
			0.63	0.08	12.5	0.05
			0.56	0.05		
			0.53	0.1		
			0.63	0.1		
			0.73	0.1		
			0.58	0.1		
20.5	7.82E+04	2.78E+03	0.65	0.13	8.1	0.06
			0.75	0.16	13.5	0.11
			0.8	0.16	8.8	0.07
			0.77	0.18	11.6	0.09
			1.05	0.21	7.7	0.06
			1.02	0.14		
			0.7	0.13		
			1.07	0.14		
			0.82	0.13		
			1	0.14		
26.0	1.34E+05	2.74E+03	0.77	0.11		
			0.71	0.09		

			0.64	0.09		
			0.79	0.13		
			0.58	0.09		
			0.62	0.07		
			0.62	0.07		
			0.64	0.13		
			0.83	0.11		
			0.73	0.11		
92.5	8.14E+04	3.01E+03	2.48	0.4	7.1	0.06
			2.73	0.27	7.9	0.06
			3.07	0.3	9.4	0.08
			2.93	0.22	10.2	0.08
			2.62	0.34	10.4	0.08
			2.53	0.38		
			3.26	0.36		
			3.1	0.25		
			3.39	0.31		
			2.63	0.2		
88.8	8.29E+04	2.85E+03	2.56	0.22	7.3	0.06
			3.2	0.25	6.3	0.05
			2.81	0.26	7.9	0.06
			3.28	0.24	6.9	0.05
			2.95	0.26		
			3.12	0.27		
			2.89	0.19		
			3.17	0.21		
			3.26	0.21		
			3.36	0.22		
88.7	8.51E+04	2.78E+03	3.27	0.32	7.0	0.06
			3.6	0.21	8.5	0.07
			3.17	0.24	6.9	0.06
			2.97	0.29	8.1	0.06
			3.31	0.34		
			3.39	0.27		
			3.31	0.29		
			3.25	0.32		
			2.71	0.17		
			3.02	0.16		

90.6	8.70E+04	2.79E+03	3.51	0.3	7.8	0.06
			3.46	0.36	6.9	0.05
			3.63	0.3	7.3	0.06
			3.38	0.29	6.8	0.05
			3.15	0.31		
			3.78	0.21		
			3.05	0.21		
			2.96	0.21		
			3.17	0.14		
			3.94	0.25		

Table A4 Variation of heat flux, departure diameter, and departure frequency with superheat for Silicon at 10°C Subcooling (Run 2)

Superheat (°C)	Heat Flux (W/m^2)	Absolute Uncertainty (W/cm^2)	Departure Diameter (mm)	Diameter Uncertainty (mm)	Frequency (Hz)	Frequency Uncertainty (Hz)
2.8	1.94E+04	2.68E+03				
13.1	4.28E+04	2.72E+03	0.53	0.1	20.8	0.17
			0.48	0.09	31.3	0.25
			0.56	0.1	41.7	0.33
			0.53	0.09	16.7	0.13
			0.5	0.1	10.4	0.08
			0.65	0.11		
			0.48	0.1		
			0.46	0.07		
			0.5	0.1		
			0.53	0.09		
26.3	7.95E+04	2.73E+03	0.48	0.07	29.4	0.24
			0.53	0.09	9.6	0.08
			0.46	0.07	20.8	0.17
			1.08	0.11	33.3	0.27
			1.23	0.14		
			1.03	0.11		
			0.99	0.14		
			1.1	0.11		

			0.75	0.09		
			0.91	0.12		
30.5	1.33E+05	2.77E+03	0.76	0.08		
			0.85	0.11		
			0.95	0.11		
			0.97	0.11		
			0.81	0.11		
			0.82	0.11		
			0.98	0.13		
			1.06	0.11		
			0.97	0.09		
			1	0.13		
91.1	8.06E+04	2.77E+03	2.76	0.23	6.9	0.05
			2.73	0.17	6.7	0.05
			3.1	0.18	7.4	0.06
			3.57	0.3	7.6	0.06
			3.03	0.21		
			3.07	0.26		
			3	0.24		
			3.03	0.18		
			2.98	0.15		
			2.69	0.22		
91.2	8.19E+04	2.91E+03	3.22	0.26	9.3	0.07
			3.27	0.23	13.9	0.11
			2.56	0.16	8.9	0.07
			2.93	0.21	6.3	0.05
			2.98	0.2		
			2.98	0.18		
			2.97	0.2		
			2.93	0.18		
			3.02	0.19		
			2.98	0.17		
91.1	8.32E+04	2.80E+03	2.87	0.18	7.3	0.06
			3	0.19	12.8	0.05
			3.05	0.18	10.2	0.08
			3.12	0.2	7.6	0.06
			3.14	0.22		
			3.04	0.2		

			3.06	0.22		
			3.19	0.19		
			3	0.18		
			2.84	0.17		
91.2	8.46E+04	2.85E+03	3.09	0.3	6.9	0.05
			2.84	0.27	9.8	0.08
			3.36	0.35	5.2	0.04
			3.12	0.25	24.4	0.1
			2.93	0.18		
			2.93	0.21		
			3.08	0.2		
			3.05	0.29		
			2.91	0.2		
			2.97	0.21		

Table A5 Variation of heat flux, departure diameter, and departure frequency with superheat for Copper at Saturation temperature (Run 1)

Superheat (°C)	Heat Flux (W/m^2)	Absolute Uncertainty (W/cm^2)	Departure Diameter (mm)	Diameter Uncertainty (mm)	Frequency (Hz)	Frequency Uncertainty (Hz)
3.5	1.43E+04	2.72E+03	0.31	0.1	30.3	0.12
			0.31	0.06	58.8	0.24
			0.3	0.1	22.7	0.09
			0.3	0.06	11.9	0.05
			0.3	0.04		
			0.3	0.06		
			0.3	0.04		
			0.29	0.06		
			0.31	0.1		
			0.41	0.08		
8.4	3.24E+04	2.72E+03	1.04	0.1	15.2	
			0.82	0.11	18.3	
			0.76	0.08	31.3	
			0.72	0.07	31.3	
			0.7	0.08		

			0.88	0.1		
			0.74	0.08		
			0.74	0.09		
			0.8	0.1		
			0.8	0.09		
11.6	6.14E+04	2.86E+03	0.5	0.11	41.7	0.33
			0.34	0.05	50.0	0.4
			0.43	0.07	20.0	0.16
			0.35	0.07	10.9	0.09
			0.47	0.09	23.8	0.19
			0.4	0.09		
			0.33	0.07		
			0.4	0.09		
			0.42	0.09		
			0.43	0.11		
13.5	6.66E+04	4.82E+03	0.42	0.13		
			0.36	0.08		
			0.38	0.08		
			0.39	0.13		
			0.48	0.1		
			0.53	0.15		
			0.41	0.06		
			0.36	0.08		
			0.47	0.13		
			0.33	0.13		
95.1	6.85E+04	2.95E+03				
97.4	6.90E+04	2.80E+03	3.44	0.22	33.3	0.13
			3.01	0.16	16.7	0.06
			3.09	0.18	20.0	0.08
			3.14	0.22	17.4	0.03
			3.11	0.19		
			2.95	0.16		
			3.48	0.36		
			3.03	0.17		
			3.24	0.2		
			3.2	0.27		
106.9	7.24E+04	3.36E+03	3.54	0.14	26.3	0.21
			3.48	0.16	23.8	0.19

			3.36	0.14	23.8	0.19
			3.54	0.14		
			2.78	0.13		
			3.02	0.13		
			3.48	0.16		
			3.65	0.15		
			3.79	0.15		
			3.5	0.15		
112.8	7.58E+04	3.39E+03	3.05	0.12	22.7	0.18
			3.46	0.08	23.8	0.19
			3.28	0.12	18.5	0.15
			3.02	0.12		
			2.85	0.08		
			3.32	0.08		
			4.24	0.13		
			3.21	0.09		
			3.12	0.16		
			2.70	0.08		

Table A6 Variation of heat flux, departure diameter, and departure frequency with superheat for Copper at Saturation temperature (Run 2)

Superheat (°C)	Heat Flux (W/m^2)	Absolute Uncertainty (W/cm^2)	Departure Diameter (mm)	Diameter Uncertainty (mm)	Frequency (Hz)	Frequency Uncertainty (Hz)
6.8	1.93E+04	2.70E+03	0.5	0.09	58.8	0.24
			0.5	0.07	58.8	0.24
			0.48	0.05	40.0	0.16
			0.5	0.09	76.9	0.31
			0.54	0.05	47.6	0.19
			0.47	0.05		
			0.48	0.07		
			0.45	0.05		
			0.48	0.05		
			0.41	0.07		
25.5	6.04E+04	2.78E+03	0.74	0.1	41.7	0.33
			0.64	0.08	9.3	0.07
			0.64	0.08	23.8	0.19

			0.76	0.1		
			0.76	0.09		
			0.67	0.08		
			0.64	0.08		
			0.69	0.08		
			0.64	0.08		
			0.59	0.08		
36.1	1.04E+05	2.82E+03	0.28	0.07		
			0.27	0.07		
			0.27	0.05		
			0.29	0.07		
			0.36	0.07		
			0.34	0.08		
			0.37	0.1		
			0.29	0.07		
			0.35	0.08		
			0.37	0.08		
45.4	1.47E+05	2.78E+03	0.31	0.1		
			0.34	0.07		
			0.37	0.12		
			0.44	0.13		
			0.46	0.16		
			0.28	0.06		
			0.36	0.06		
			0.46	0.16		
			0.33	0.09		
			0.35	0.09		
92.2	6.83E+04	2.95E+03	4.25	0.25	18.5	0.04
			4.77	0.27	21.3	0.09
			4.53	0.32	15.4	0.06
			4.2	0.24	19.6	0.08
			4.71	0.35		
			5.12	0.21		
			4.92	0.28		
			4.52	0.29		
			4.72	0.19		
			4.33	0.25		
94.5	6.83E+04	2.98E+03	3.37	0.12	8.5	0.07
			3.51	0.15	10.4	0.08
			3.72	0.12	17.2	0.14
			3.1	0.12	23.8	0.19
			3.16	0.13		
			3.47	0.12		

			3.07	0.15		
			3.4	0.13		
			3.13	0.12		
			3.22	0.13		
103.8	7.87E+04	3.20E+03	3.83	0.29	20.0	0.16
			3.37	0.27	40.0	0.16
			3.2	0.22	9.6	0.08
			3.91	0.29	20.0	0.16
			3.25	0.26		
			3.94	0.27		
			3.67	0.22		
			3.22	0.26		
			3.1	0.26		
			2.78	0.22		
112.8	8.27E+04	3.11E+03	3.93	0.22	20.8	0.17
			2.78	0.19	16.1	0.13
			2.87	0.17	17.2	0.14
			2.63	0.16		
			3.29	0.2		
			3.53	0.2		
			3.22	0.21		
			2.73	0.18		
			3.61	0.21		
			3.35	0.2		

Table A7 Variation of heat flux, departure diameter, and departure frequency with superheat for Copper at 5°C Subcooling (Run 1)

Superheat (°C)	Heat Flux (W/m^2)	Absolute Uncertainty (W/cm^2)	Departure Diameter (mm)	Diameter Uncertainty (mm)	Frequency (Hz)	Frequency Uncertainty (Hz)
5.1	1.85E+04	2.72E+03	0.55	0.11	13.2	0.11
			0.6	0.11	15.6	0.13
			0.59	0.11	8.5	0.07
			0.54	0.11	12.2	0.1
			0.56	0.11		
			0.54	0.11		
			0.54	0.11		

			0.53	0.11		
			0.53	0.11		
			0.54	0.11		
7.9	4.10E+04	2.65E+03	0.35	0.12	13.2	0.11
			0.38	0.12	27.8	0.22
			0.44	0.12	100.0	0.4
			0.41	0.12	11.6	0.09
			0.47	0.12		
			0.59	0.15		
			0.35	0.12		
			0.38	0.12		
			0.53	0.12		
			0.59	0.13		
10.8	7.39E+04	2.66E+03	0.44	0.13	37.0	0.15
			0.47	0.13	29.4	0.12
			0.53	0.16	10.8	0.04
			0.44	0.13	7.3	0.03
			0.5	0.13		
			0.47	0.13		
			0.47	0.13		
			0.53	0.13		
			0.47	0.13		
			0.5	0.13		
102.0	6.87E+04	2.79E+03	3.71	0.23	9.3	0.07
			3.21	0.2	12.2	0.1
			3	0.18	10.9	0.09
			3.57	0.2	12.5	0.1
			3.65	0.2		
			3.76	0.18		
			3.5	0.19		
			3.29	0.17		
			3.42	0.17		
			3.21	0.19		
109.5	7.30E+04	2.87E+03	4.12	0.26	13.5	0.11
			3.58	0.21	16.7	0.13
			4.29	0.19	13.2	0.11
			3.63	0.2	13.9	0.11
			3.96	0.23		

			4.19	0.21		
			3.68	0.21		
			3.6	0.21		
			3.42	0.2		
			3.86	0.19		
116.7	7.79E+04	2.84E+03	3.91	0.24	9.8	0.08
			3.72	0.26	13.2	0.11
			3.62	0.27	8.6	0.07
			3.26	0.25	8.8	0.07
			3.94	0.25		
			3.69	0.23		
			3.75	0.2		
			3.58	0.23		
			3.6	0.22		
			3.79	0.19		
124.1	8.27E+04	2.83E+03				
131.2	8.73E+04	2.89E+03	4.04	0.23	7.8	0.06
			4.34	0.28	8.3	0.07
			4.49	0.25	9.1	0.07
			4.72	0.3	8.8	0.07
			4.38	0.29		
			3.95	0.2		
			3.39	0.23		
			3.66	0.25		
			3.89	0.29		
			3.93	0.21		

Table A8 Variation of heat flux, departure diameter, and departure frequency with superheat for Copper at 5°C Subcooling (Run 2)

Superheat (°C)	Heat Flux (W/m^2)	Absolute Uncertainty (W/cm^2)	Departure Diameter (mm)	Diameter Uncertainty (mm)	Frequency (Hz)	Frequency Uncertainty (Hz)
6.5	1.79E+04	2.68E+03				
18.4	4.00E+04	2.73E+03	0.68	0.09		
			0.55	0.06		
			0.53	0.06		

			0.57	0.07		
			0.53	0.06		
			0.56	0.05		
			0.5	0.05		
			0.52	0.06		
			0.55	0.05		
			0.52	0.04		
23.5	7.55E+04	2.72E+03	0.77	0.08	50.0	0.2
			0.8	0.09	34.5	0.14
			0.85	0.1	30.3	0.12
			0.83	0.1	31.3	0.13
			0.69	0.09		
			0.67	0.07		
			0.65	0.08		
			0.72	0.07		
			0.59	0.1		
			0.6	0.1		
36.5	1.23E+05	2.73E+03	0.81	0.08	7.0	0.06
			0.79	0.09	29.4	0.24
			0.86	0.09	8.1	0.06
			0.86	0.09		
			0.86	0.09		
			0.88	0.09		
			0.91	0.09		
			1.16	0.13		
			0.93	0.09		
			0.97	0.11		
42.8	1.45E+05	2.71E+03			100.0	0.4
					23.3	0.09
					142.9	0.57
					26.3	0.11
					55.6	0.22
100.6	6.83E+04	2.95E+03				
104.5	7.11E+04	2.86E+03				
108.4	7.31E+04	2.84E+03	2.99	0.2	5.4	0.04
			3.58	0.29	6.5	0.05
			3.65	0.26	11.1	0.09
			3.51	0.23	7.1	0.06
			3.43	0.3		
			3.62	0.24		

			3.05	0.2		
			3.41	0.21		
			3.66	0.25		
			3.52	0.31		
116.6	7.86E+04	2.88E+03	3.56	0.25	6.0	0.05
			3.63	0.26	19.2	0.15
			3.73	0.32	8.9	0.07
			3.5	0.24	11.9	0.1
			3.36	0.24		
			3.63	0.29		
			3.47	0.26		
			4.07	0.32		
			4.04	0.36		
			3.79	0.51		
123.8	8.26E+04	2.81E+03	3.3	0.36	10.2	0.08
			4.18	0.47	21.7	0.17
			3.61	0.38	10.2	0.08
			4.15	0.48	5.6	0.04
			3.3	0.36		
			3.77	0.41		
			3.25	0.35		
			3.34	0.35		
			3.83	0.42		
			3.53	0.38		
130.5	8.69E+04	2.81E+03	3.32	0.27	4.8	0.04
			3.55	0.33	6.0	0.05
			3.75	0.33	5.6	0.04
			3.68	0.38	6.2	0.05
			3.44	0.31		
			3.18	0.28		
			3.11	0.26		
			3.47	0.3		
			3.5	0.31		
			3.22	0.25		

Table A9 Variation of heat flux, departure diameter, and departure frequency with superheat for Copper at 10°C Subcooling (Run 1)

Superheat (°C)	Heat Flux (W/m^2)	Absolute Uncertainty (W/cm^2)	Departure Diameter (mm)	Diameter Uncertainty (mm)	Frequency (Hz)	Frequency Uncertainty (Hz)
3.4	2.07E+04	2.70E+03	0.48	0.07	28.6	0.11
			0.5	0.07	55.6	0.22
			0.47	0.07	71.4	0.29
			0.48	0.07	27.8	0.11
			0.52	0.07	20.0	0.08
			0.5	0.08		
			0.45	0.07		
			0.48	0.07		
			0.52	0.07		
			0.53	0.07		
11.3	4.35E+04	2.73E+03	0.3	0.06	11.6	0.09
			0.51	0.07	50.0	0.4
			0.51	0.08	9.1	0.07
			0.66	0.1		
			0.54	0.07		
			0.46	0.08		
			0.51	0.08		
			0.45	0.08		
			0.69	0.07		
			0.58	0.08		
15.0	7.44E+04	2.69E+03	0.42	0.08	9.8	0.08
			0.52	0.08		
			0.5	0.12		
			0.6	0.12		
			0.46	0.1		
			0.56	0.08		
			0.48	0.08		
			0.66	0.08		
			0.48	0.1		
			0.42	0.08		
46.7	2.02E+05	2.79E+03				
86.9	7.57E+04	2.92E+03	2.65	0.27	12.2	0.1

			2.88	0.27	9.8	0.08
			2.91	0.22	9.4	0.08
			2.88	0.23	8.9	0.07
			2.98	0.25	9.4	0.04
			2.86	0.23		
			2.88	0.21		
			3.21	0.22		
			2.92	0.21		
			3.03	0.21		
107.1	7.12E+04	2.87E+03	3.84	0.25	11.6	0.09
			3.38	0.21	10.6	0.09
			4	0.38	11.6	0.09
			3.54	0.29	14.3	0.11
			3.2	0.2	14.7	0.12
			3.38	0.21		
			3.7	0.21		
			3.47	0.21		
			3.38	0.21		
			3.27	0.23		
121.2	7.94E+04	2.80E+03	3.12	0.19	14.5	0.06
			3.24	0.28	13.5	0.11
			3.18	0.28	13.5	0.11
			3.64	0.2	12.7	0.05
			3.33	0.25		
			3.04	0.26		
			3.04	0.17		
			3.85	0.3		
			3.88	0.2		
			3.32	0.21		
134.8	8.92E+04	2.76E+03	3.84	0.23	11.4	0.09
			3.21	0.28	15.2	0.12
			3.68	0.3	9.4	0.04
			4.28	0.22	9.3	0.07
			3.65	0.19	11.1	0.09
			3.92	0.25		
			3.56	0.17		
			3.44	0.16		

			4.02	0.19		
			3.78	0.21		

Table A10 Variation of heat flux, departure diameter, and departure frequency with superheat for Copper at 10°C Subcooling (Run 2)

Superheat (°C)	Heat Flux (W/m^2)	Absolute Uncertainty (W/cm^2)	Departure Diameter (mm)	Diameter Uncertainty (mm)	Frequency (Hz)	Frequency Uncertainty (Hz)
3.5	1.81E+04	2.75E+03				
20.3	4.20E+04	2.78E+03	0.56	0.05	8.1	0.06
			0.58	0.05	10.0	0.08
			0.74	0.08	29.4	0.24
			0.69	0.06	29.4	0.24
			0.63	0.08		
			0.66	0.06		
			0.71	0.06		
			0.69	0.08		
			0.76	0.08		
			0.69	0.06		
26.3	7.64E+04	2.70E+03	0.63	0.08	22.7	0.18
			0.63	0.07	14.3	0.11
			0.69	0.06	27.8	0.22
			0.72	0.07	14.3	0.11
			0.72	0.07		
			0.74	0.07		
			0.79	0.08		
			0.83	0.07		
			0.72	0.07		
			0.79	0.08		
32.4	1.32E+05	2.84E+03	0.76	0.09		
			0.72	0.09		
			0.72	0.1		
			0.68	0.08		
			0.7	0.08		
			0.72	0.08		

			0.76	0.08		
			0.89	0.1		
			0.68	0.08		
			0.63	0.08		
100.1	7.23E+04	2.82E+03	3.12	0.23	16.1	0.13
			3.33	0.25	11.1	0.09
			2.76	0.21	9.1	0.07
			3.52	0.27	8.6	0.07
			3.07	0.22		
			3.07	0.25		
			2.83	0.16		
			2.66	0.17		
			2.69	0.15		
			3.26	0.21		
114.5	7.76E+04	2.91E+03	4.04	0.36	6.2	0.05
			3.76	0.33	8.6	0.07
			4.14	0.38	10.6	0.09
			4	0.38	8.9	0.07
			3.69	0.34		
			4.03	0.37		
			4.02	0.37		
			3.64	0.33		
			3.52	0.31		
			4.04	0.35		
131.5	8.58E+04	2.88E+03	3.59	0.16	14.7	0.12
			3.51	0.18	12.7	0.05
			3.44	0.19	16.1	0.13
			3.95	0.24	16.1	0.13
			3.68	0.23		
			3.3	0.22		
			3.65	0.24		
			3.43	0.2		
			3.46	0.21		
			3.51	0.21		

Table A11 Variation of heat flux, departure diameter, and departure frequency with superheat for AAO at 5°C Subcooling (Run 1)

Superheat (°C)	Heat Flux (W/m^2)	Absolute Uncertainty (W/cm^2)	Departure Diameter (mm)	Diameter Uncertainty (mm)	Frequency (Hz)	Frequency Uncertainty (Hz)
3.8	2.29E+04	2.77E+03				
6.0	4.56E+04	2.73E+03	0.61	0.03	35.7	0.14
			0.62	0.08	29.4	0.12
			0.71	0.11	32.3	0.13
			0.64	0.03	27.8	0.11
			0.58	0.05		
			0.55	0.11		
			0.71	0.03		
			0.47	0.05		
			0.61	0.03		
			0.5	0.09		
7.5	7.89E+04	2.88E+03	0.55	0.06	27.8	0.22
			0.49	0.09	17.9	0.14
			0.59	0.14	12.8	0.1
			0.46	0.09	17.2	0.14
			0.41	0.03		
			0.46	0.08		
			0.4	0.08		
			0.38	0.05		
			0.53	0.03		
			0.5	0.06		
9.8	1.24E+05	3.00E+03				
10.6	1.43E+05	3.10E+03	0.55	0.05	22.7	0.18
			0.56	0.08	50.0	0.4
			0.43	0.03	14.3	0.11
			0.49	0.09	50.0	0.4
			0.52	0.05		
			0.73	0.06		
			0.36	0.09		
			0.53	0.05		
			0.53	0.03		
			0.41	0.08		

Table A12 Variation of heat flux, departure diameter, and departure frequency with superheat for AAO at 5°C Subcooling (Run 2)

Superheat (°C)	Heat Flux (W/m^2)	Absolute Uncertainty (W/cm^2)	Departure Diameter (mm)	Diameter Uncertainty (mm)	Frequency (Hz)	Frequency Uncertainty (Hz)
4.2	2.04E+04	2.72E+03	0.22	0.03	58.8	0.24
			0.18	0.03	100.0	0.4
			0.24	0.05	62.5	0.25
			0.16	0.03	76.9	0.31
			0.22	0.03		
			0.18	0.03		
			0.26	0.03		
			0.34	0.03		
			0.14	0.03		
			0.21	0.05		
7.1	4.11E+04	2.80E+03	0.84	0.05	26.3	0.11
			0.57	0.04	27.0	0.11
			0.79	0.05	32.3	0.13
			0.4	0.03	33.3	0.13
			0.79	0.1		
			0.63	0.04		
			0.68	0.04		
			0.7	0.04		
			0.66	0.04		
			0.65	0.05		
9.9	8.58E+04	3.18E+03	0.38	0.08	58.8	0.24
			0.38	0.05	47.6	0.19
			0.4	0.03	34.5	0.14
			0.46	0.07	45.5	0.18
			0.42	0.03	83.3	0.33
			0.46	0.05		
			0.46	0.04		
			0.37	0.05		
			0.46	0.04		
			0.45	0.05		
11.3	1.28E+05	3.92E+03				
11.2	1.39E+05	3.50E+03				

Table A13 Variation of heat flux, departure diameter, and departure frequency with superheat for AAO at 10°C Subcooling (Run 1)

Superheat (°C)	Heat Flux (W/m^2)	Absolute Uncertainty (W/cm^2)	Departure Diameter (mm)	Diameter Uncertainty (mm)	Frequency (Hz)	Frequency Uncertainty (Hz)
1.3	2.83E+04	2.68E+03				
2.1	4.93E+04	2.73E+03	0.29	0.04	18.9	0.08
			0.38	0.04	14.7	0.06
			0.31	0.04	16.1	0.06
			0.36	0.07	14.9	0.06
			0.29	0.06		
			0.33	0.04		
			0.33	0.04		
			0.29	0.04		
			0.27	0.04		
			0.31	0.06		
4.1	8.25E+04	2.75E+03	0.33	0.03	9.5	0.04
			0.4	0.03	17.9	0.07
			0.35	0.08	27.8	0.11
			0.35	0.03	41.7	0.17
			0.32	0.06		
			0.36	0.06		
			0.28	0.06		
			0.38	0.03		
			0.33	0.03		
			0.3	0.05		
6.4	1.28E+05	3.00E+03	0.38	0.04	22.7	0.09
			0.36	0.06	21.3	0.09
			0.43	0.04	14.9	0.06
			0.43	0.06		
			0.41	0.04		
			0.38	0.06		
			0.3	0.04		
			0.3	0.04		
			0.24	0.04		
			0.43	0.04		
5.7	1.41E+05	3.74E+03				

Table A14 Variation of heat flux, departure diameter, and departure frequency with superheat for AAO at 10°C Subcooling (Run 2)

Superheat (°C)	Heat Flux (W/m^2)	Absolute Uncertainty (W/cm^2)	Departure Diameter (mm)	Diameter Uncertainty (mm)	Frequency (Hz)	Frequency Uncertainty (Hz)
0.3	1.86E+04	2.81E+03				
3.4	4.22E+04	2.75E+03	0.67	0.13	27.8	0.22
			0.57	0.05	11.9	0.1
			0.37	0.06	23.8	0.19
			0.43	0.04	29.4	0.24
			0.47	0.04		
			0.63	0.1		
			0.53	0.05		
			0.51	0.05		
			0.59	0.05		
			0.61	0.05		
5.2	6.81E+04	2.81E+03	0.58	0.06	19.2	0.15
			0.58	0.06	16.7	0.13
			0.68	0.07	19.2	0.15
			0.54	0.06	14.7	0.12
			0.62	0.05		
			0.58	0.06		
			0.52	0.04		
			0.52	0.04		
			0.52	0.08		
			0.4	0.06		
8.4	1.11E+05	3.24E+03	0.65	0.05	45.5	0.18
			0.7	0.06	34.5	0.14
			0.54	0.05	47.6	0.19
			0.68	0.03	40.0	0.16
			0.68	0.09	34.5	0.14
			0.7	0.06		
			0.81	0.05		
			0.8	0.04		
			0.61	0.06		
			0.83	0.08		